ABSTRACT

Title of dissertation: ASSIMILATION OF TRACE GAS RETRIEVALS WITH THE LOCAL ENSEMBLE TRANSFORM KALMAN FILTER

David Derieg Kuhl, Doctor of Philosophy, 2009

Dissertation directed by: Professor Eugenia Kalnay
and
Professor Istvan Szunyogh
Department of Atmospheric and Oceanic Science

Over the 50 year history of Numerical Weather Prediction (NWP), the focus has been on the modeling and prediction of meteorological parameters such as surface pressure, temperature, wind, and precipitation. However, due to concerns over pollution and to recent advancements in satellite technologies, an increasing number of NWP systems have been upgraded to include capabilities to analyze and predict the concentration of trace gases. This dissertation explores some of the specific issues that have to be addressed for an efficient modeling of the concentration of the trace gases. These issues include modeling the effects of convective mixing on the concentration of the trace gases and the multivariate assimilation of space-based observations of the concentration of the trace gases.

In this dissertation, we assimilate observations of the concentration of trace gases with an implementation of the Local Ensemble Transform Kalman Filter (LETKF) data assimilation system on the National Centers for Environmental Pre-

diction (NCEP) Global Forecast System (GFS) NWP model. We use a modified version of the NCEP GFS model that was operational in 2004 at resolution T62/L28. We modify the model by adding parameterization for the process of convective mixing of the trace gases. We consider two specific trace gases: ozone (O_3) and carbon monoxide (CO). We incorporate these gases into the model by using 3-dimensional time-dependent O_3 and CO production-loss values from the Real-time Air Quality Modeling System (RAQMS) global chemical model. The O_3 observations we assimilate are from the Solar Backscatter UltraViolet generation 2 (SBUV/2) satellite instrument (version 8) flown on the NOAA 16 and 17 satellites. The CO observations we assimilate are from the Measurements Of Pollution In The Troposphere (MOPITT) instrument (version 3) flown on the NASA TERRA satellite. We also develop a new observation operator for the assimilation of retrievals with the LETKF.

We carry out numerical experiment for the period between 000UTC 1 July 2004 to 000UTC 15 August in the summer of 2004. The analysis and forecast impact of the assimilation of trace gas observations on the meteorological fields is assessed by comparing the analyses and forecasts to the high resolution operational NCEP GFS analyses and to radiosonde observations. The analysis and forecast impact on the trace gas fields is assessed by comparing the analyzed and predicted fields to observations collected during the Intercontinental Chemical Transport Experiment (INTEX-A) field mission. The INTEX-A field mission was conducted to characterize composition of pollution over North America, thus providing us with ozonesonde and aircraft based verification data.

We find that adding the process of convective mixing to the parameterization

package of the model and the assimilation of observations of the trace gases improves the analysis and forecast of the concentration of the trace gases. In particular, our system is more accurate in quantifying the concentration of O_3 in the troposphere than the original NCEP GFS. Also, our system is competitive with the state-of-the-art RAQMS atmospheric chemical model in analyzing the concentration of O_3 and CO throughout the full atmospheric model column.

The assimilation of O_3 and CO observations has a mixed impact on the analysis and forecast of the meteorological fields. We find that most of the negative impact on the meteorological fields can be eliminated, without much reduction to the positive impact on the trace gas fields, by inflating the prescribed variance of the trace gas observations.

The appendices of this dissertation reproduces two papers on related research. The first paper covers the northward front movement and rising surface temperatures in the great planes. The second paper covers the assessment of predictability with a Local Ensemble Kalman Filter

ASSIMILATION OF TRACE GAS RETRIEVALS WITH THE LOCAL ENSEMBLE TRANSFORM KALMAN FILTER

by

David Derieg Kuhl

Dissertation submitted to the Faculty of the Graduate School of the
University of Maryland, College Park in partial fulfillment
of the requirements for the degree of
Doctor of Philosophy
2009

Advisory Committee:
Professor Eugenia Kalnay, Chair and Academic Advisor
Professor Istvan Szunyogh, Co-Chair and Research Advisor
Dr. Brad Pierce, Mentor
Professor Kayo Ide
Professor Brian Hunt
Professor Robert Hudson

Dedication

This dissertation is dedicated to my father Arthur Derieg Kuhl.

Acknowledgments

I owe thanks to many people for making this dissertation possible. I would like to first thank my entire dissertation committee. Thanks to Istvan Szunyogh and Brad Pierce who helped me and directed me throughout my research. I cannot say enough about the wonderful guidance they both gave me throughout my entire graduate school journey. I would like to thank the other authors on the two appendices: for Appendix A that includes Debra Baker and Bob Hudson, for Appendix B that includes Istvan Szunyogh, Eric Kostelich, Gyrogyi Gyarmati, D. J. Patil, Mike Oczkowski, Brian Hunt, Eugenia Kalnay, Ed Ott and Jim Yorke.

Thanks to the entire Chaos Weather group. Thanks to Eugenia Kalnay for her support, advice and direction. Thanks to Kayo Ide for her taking the time to listen and reflect on my research since Istvan moved to Texas. Thanks to Ed Ott for his early insights and recommendations. Thanks especially to Eric Kostelich for all his support, coding expertise and giving me the opportunity to work with him at the MSRI summer workshop. And thanks to Liz Satterfield and Elana Fertig for listening and helping me all along the way. A special thanks to Gyorgyi Gyarmait, Alfredo Nava-Tudela, Aleksey Zimin and Guillaume Marcais who set-up the computer clusters and kept them running and then, in the last few months, helped me to continue their work.

Thanks to the entire Chemistry and Dynamics Branch at NASA Langley for hosting me for my second and third years in graduate school. Thanks especially to Doreen O'Neil for financially supporting me through nearly all of my graduate

studies. Thanks to Jassim al-Saadi for his insights and direction. Thanks to Murali Natarajan for his support and insight. Thanks to Bruce Doddridge for his support and encouragement. And a very special thanks to the late Cheiko Kittaka for her friendship and support.

Thanks to the National Institute for Aerospace in Hampton Virginia for initially helping set-up the collaboration between the UMD Chaos Weather group and NASA Langley. Thanks to Bernie Grossman and all the administrative staff at the NIA who helped throughout the years. Thanks to the NASA GSRP which directed my funding for two years.

Thanks to the Atmospheric and Oceanic Science department at Maryland. Thanks to the all my class professors. I would like to thank the entire administrative staff in the AOSC department especially June Sherer and Sonya Junek for helping sort out my complicated funding and health insurance nearly every year of graduate school. Thanks to all my fellow graduate students who were always there for support. I would like to especially like to acknowledge Debra Baker, Scott Rabenhorst, Dagmar Merkova, Matus Martini and Anthony Santorelli.

Last, and certainly not least, I would like to thank all my family and friends. All of my friends which supported me all this time and who are too many to name. All of my family especially my brother Joe for his support and insight. My mother, Jean Kuhl, for her tireless support throughout all of my life. And to my father, Arthur Kuhl, for whom this work is dedicated, who passed away several months ago and was always there for me. And finally, I thank my wife Aysha Keisler without whom I would probably never have started this wonderful journey and who lovingly

supported me along every step of the process.

Thank you all!

Table of Contents

List of Tables

List of Figures

List of Abbreviations

4D-Var	4-Dimensional Variational
AMSU	Advanced Microwave Sounding Unit
CAM3	Communality Atmosphere Model
CLD	Chemiluminescesnse Detector
COBRA	CO2 Budget and Rectification Airborne
DACOM	Differential Absorptions CO Measurement
ECC	Electrochemical Concentration Cell
EnKF	Ensemble Kalman Filtering
GFS	Global Forecast System
HALOE	HALogen Occultation Experiment
INTEX	Intercontinental Chemical Transport Experiment
IONS	INTEX Ozonesonde Network Study
LEKF	Local Ensemble Kalman Filter
LETKF	Local Ensemble Transform Kalman Filter
LIDAR	Light Detection and Ranging
MODIS	MODerate Resolution Imaging Spectroradiometer
MOPITT	Measurements Of Pollution In The Troposphere
MOZAIC	Measurement of OZone, water vapor, carbon monoxide and nitrogen oxides by Airbus In-service airCraft
NCEP	National Centers for Environmental Prediction
NMHC	Non-Methane HydroCarbon
NWP	Numerical Weather Prediction
OI	Optimal Interpolation
RAQMS	Real-time Air Quality Modeling System
SBUV/2	Solar Backscatter UltraViolet generation 2
SAGE	Stratospheric Aerosol and Gas Experiment
SDF	Statistical Digital Filter
TDL	Tunable Diode Laser

Chapter 1

Introduction

Anthropogenic activities have been significantly perturbing the chemical composition of the atmosphere through emissions of trace gases. Thus, improving our air quality modeling capabilities is important for the safety and the well-being of the public. In particular, the improved modeling capabilities are expected to lead to a better understanding of the chemical composition of the atmosphere and to improved forecasts of the concentration of the trace gases. Chemical transport models integrate the effects of chemical sources, chemical formation-destruction processes and atmospheric dynamics. The quality of the representation of the meteorological processes in the model has a significant effect on the quality of the modeling of the atmospheric constituents (e.g., Miyazaki 2009). Thus, it is desirable to use an advanced, highly tuned Numerical Weather Prediction (NWP) model as the dynamical component of the transport model. In addition, incorporating chemical processes into a NWP system has the potential to improve the analysis and the forecast of the meteorological parameters. One way to achieve this, without increasing the computational expense to an unaffordable level, is to externally calculate the chemical sources and chemical formation-destruction processes with a chemical model, and then incorporate this information into a NWP system through a 3-dimensional spatio-temporally varying production-loss parameter fields.

Data assimilation is the process of obtaining the initial conditions (analysis) of a model forecast based on observations and the model dynamics (Kalnay 2003 and Evensen 2007). Advanced data assimilation schemes are multivariate statistical-dynamical techniques that can take advantage of information about the covariance between uncertainties in the forecast-based estimates of the different model variables. Such covariance is expected to exist between the concentration of chemical constituents with long lifetimes and the meteorological variables.

The two advanced approaches for data assimilation are 4-Dimensional Variational assimilation (4D-Var) and Ensemble based Kalman Filtering (EnKF). In this dissertation, we focus on one specific ensemble-based Kalman Filter, the Local Ensemble Transform Kalman Filter (LETKF) (Hunt et al., 2007). While other studies have demonstrated that univariate EnKF can provide high quality analysis of the concentration fields (e.g., Arellano et al. 2007; Constantinescu et al. 2007) to the best of our knowledge, ours is the first successful attempt for the multivariate assimilation of meteorological and chemical observation with an ensemble-based Kalman filter. We assess the effect of the chemical data assimilation on the analysis and the ensuing forecast of the meteorological fields with both a univariate and a multivariate version of LETKF for the assimilation of the chemical observations.

There are several long-lived chemical constituents in the atmosphere, that are currently being observed by satellites. The use of satellite observations in data assimilation presents a choice of either directly using the radiance observations or using processed retrieval observations. In NWP the direct assimilation of radiances has replaced the assimilation of retrievals for such variables as temperature and humid-

ity (Thepaut, 2003). The advantages and disadvantages of radiance and retrieval assimilation are listed in Table 1.1. The primary advantages of radiance assimilation are that A1) the results are not affected by external processes for which the error characteristics may be poorly known and A2) the radiance observations are less affected by spatially correlated errors than the retrievals. The main disadvantages of radiance assimilation are that D1) the increased computational cost associated with the use of a radiative transfer model in the observational operator (the observation operator maps the model state to the observables in the data assimilation) and D2) the cost of doing quality control for each observation. Though the assimilation of satellite radiance observations have been embraced by the NWP community, trace gas observations have been typically assimilated as retrievals. The main advantages of retrieval assimilations are that A1) the observations are expressed in the form of geophysical fields, hence, the observation operators are less computationally expensive and that A2) the quality control and monitoring is handled by the experienced organizations producing the retrievals. The main disadvantages to retrieval assimilation are that D1) they are affected by external processing characteristics (such as a priori information and smoothing) that introduce spatially correlated observation errors with often not very well known error characteristics. In the present study, we assimilate retrievals of the trace gases. However, we use advanced observation operators (originally proposed by Rodgers 2000 and discussed in Chapter 2) to account for the effects of the process that produces the retrievals.

Our NWP system is based on the NCEP (National Centers for Environmental Prediction) GFS (Global Forecast System), into which we incorporate the chem-

Table 1.1: Advantages and disadvantages of radiance and retrieval assimilation.

	Radiance Assimilation	**Retrieval Assimilation**
Advantages	1) the results are not affected by external processes for which the error characteristics may be poorly known 2) the radiance observations are less affected by spatially correlated errors than the retrievals	1) the observations are expressed in the form of geophysical fields, hence, the observation operators are less computationally expensive 2) the quality control and monitoring is handled by the experienced organizations producing the retrievals
Disadvantages	1) the increased computational cost associated with the use of a radiative transfer model in the observational operator 2) the cost of doing quality control for each observation	1) they are affected by external processing characteristics (such as a priori information and smoothing) that introduce spatially correlated observation errors with often not very well known error characteristics

ical production-loss parameters provided by the RAQMS (Real-time Air Quality Modeling System) (Pierce et al., 2007) chemical model. The meteorological observations we assimilate include all surface pressure, temperature, and wind meteorological observations operationally assimilated by NCEP, but they do not include the operationally assimilated radiance observations. The two chemical constituents we assimilate are ozone (O_3) and carbon monoxide (CO). The constituents have long lifetimes in the free troposphere and lower stratosphere and are of interest to air quality. The chemical constituent satellite observations include SBUV/2 (Solar Backscatter UltraViolet generation 2) version 8 ozone retrievals and MOPITT (Measurements Of Pollution In The Troposphere) version 3 carbon monoxide retrievals. In what follows we refer to these species as trace gases.

To evaluate the resulting impact of multivariate data assimilation of trace gases on the meteorological fields we compare our analyses and forecasts to the operational NCEP GFS analyses and to radiosonde observations. To evaluate the impact of data assimilation on the trace gas fields, we compare our analyses and forecasts to in situ aircraft measurements and to other independent observations collected in the INTEX-A (Intercontinental Chemical Transport Experiment) field mission over the North Eastern United States.

Chapter 2 describes the design of our experiments. Chapters 3 and 4 present and discuss the results of the assimilation experiments with the SBUV/2 O_3 retrieval and the MOPITT CO retrievals. Chapter 5 draws the conclusions of our research. Appendix A reproduces a paper on northward front movement and rising surface temperatures. Appendix B reproduces a paper on assessing predictability with a

Local Ensemble Kalman Filter.

Chapter 2

Background

In this chapter we discuss the experiment design to assimilate trace gas satellite retrievals in the 2004 operational NCEP GFS using the LETKF (Local Ensemble Transform Kalman Filter) algorithm. The design includes our modifications to the NCEP GFS and LETKF schemes, expanding both the number of variables modeled and observations assimilated. We also develop a modified version of the assimilation observation operator for retrieval assimilation, a localization scheme and a "covariance inflation" strategy for the trace gas observations.

2.1 The Model

All experiments are carried out with a version of the NCEP GFS model that was operational at the beginning of 2004. The model is a spectral model, meaning that the model state variables are height-dependent coefficients of a spherical harmonic expansion of the atmospheric fields on the globe. The model includes the following spectral coefficient variables: two-dimensional vorticity and divergence, virtual temperature, logarithm of the surface pressure, specific humidity, and O_3 mixing ratio. To save computational time, we use a reduced resolution of T62 in the horizontal direction (about 150 km in the mid-latitudes) and 28 sigma levels in the vertical direction. The full operational resolution model (whose operational anal-

ysis is used as a verification of our meteorological field impacts in Chapters 3 and 4) in 2004 was T254 in the horizontal direction (about 35 km in the mid-latitudes) and 64 sigma levels in the vertical direction. We made further modifications to the NCEP GFS, adding a convective mixing scheme for the trace gases and replaced the input based on climatology for the production and loss of the traces gases with a formulation from the RAQMS model.

2.1.1 NCEP GFS O_3 Modeling

The O_3 mixing ratio is one of the prognostic variables in the operational setup of the GFS. The primary use of O_3 field in the 2004 operational NCEP GFS model is for the computation of the stratospheric radiative processes. Thus, the model is tuned to account for the distribution of O_3 in the stratosphere, but not in troposphere.

The spatio-temporal evolution of O_3 is described by a tracer equation, which feeds back on the dynamics through stratospheric radiative processes. The O_3 continuity equation is solved by first applying the transport algorithm to the O_3 field, followed by the chemistry production-loss operator. In the operational GFS, the transport and chemistry time steps are 7.5 minutes. The continuity equation for O_3 can be written as:

$$\frac{\partial \chi}{\partial t} = -\mathbf{v} \cdot \nabla (\chi) + P - D\chi + \chi_d. \tag{2.1}$$

Here χ is the O_3 mixing ratio in kg/kg, $\mathbf{v}$ is the horizontal and vertical velocities, P is the photochemical production rate, D is the photochemical destruction rate per

unit O_3 mixing ratio (destruction coefficient) and χ_d is weak horizontal and vertical diffusion of ozone. The advection term $\mathbf{v} \cdot \nabla(\chi)$ is composed of the velocity vector $\mathbf{v}$ and the gradient of the O_3 mixing ratio field $\nabla(\chi)$ which gives the contribution due to air motion to the local O_3 mixing ratio.

The advection terms $\mathbf{v} \cdot \nabla(\chi)$ are evaluated to produce an intermediate constituent field χ^*; the photochemical terms are accounted for by writing Equation 2.1 as a difference equation:

$$\frac{\chi(t) - \chi(0)}{\Delta t} = \frac{\chi^* - \chi(0)}{\Delta t} + P - L\chi(t), \tag{2.2}$$

and solving

$$\chi(t) = \frac{\chi^* + P\Delta t}{1 + L\Delta t}, \tag{2.3}$$

(Rood et al., 1991).

The production P and destruction coefficient D for the 2004 operational NCEP GFS O_3 mixing ratio variable are derived from the zonal and 10-day averages (Derber et al., 1998) obtained from the NASA Goddard Space Flight Center offline two-dimensional middle atmosphere model (Fleming et al., 2002). In Figure 2.1 we show the production and destruction coefficient for 000UTC 18 July 2004 to 000UTC 28 July 2004. The model contains basic tropospheric chemical modeling with neither daily nor longitudinal variation in the O_3 production-loss parameters. Note the lack of latitudinal variation to the O_3 production parameter at the surface. Due to large spatially (and temporally) varying surface emissions of O_3 and O_3 precursors in the real atmosphere, this approach poorly represents the tropospheric O_3 production.

In Figure 2.2 (a), we show the high resolution operational NCEP GFS analysis

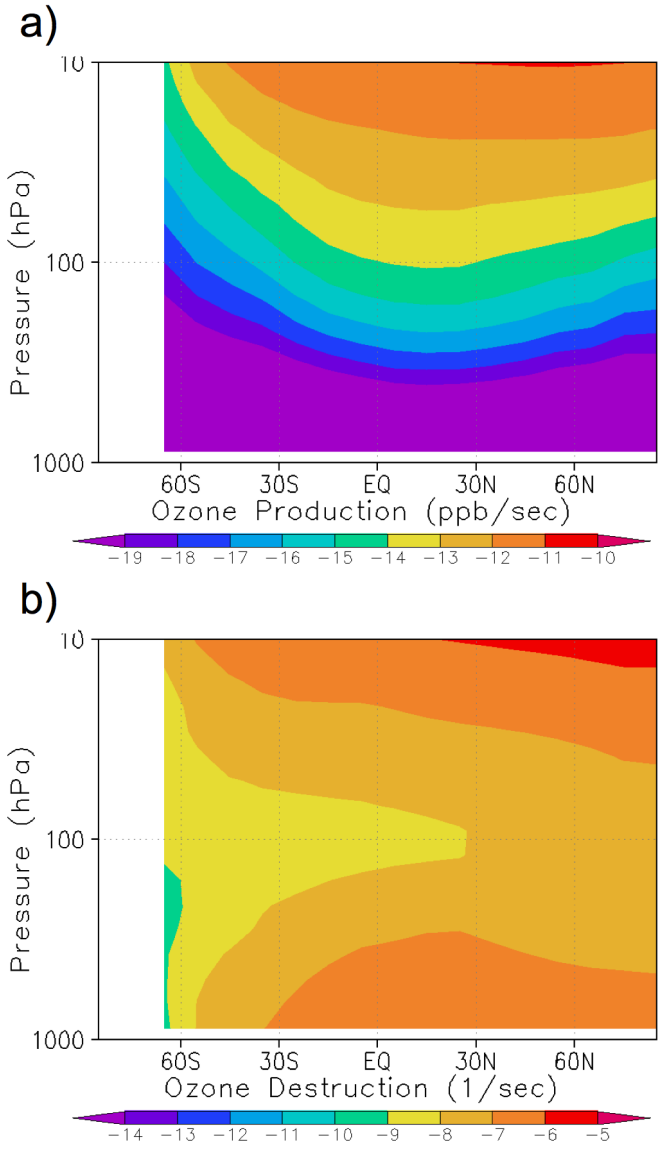

Figure 2.1: 2004 operational NCEP GFS O_3 production-loss parameters for 000UTC 18 July 2004 to 000UTC 28 July 2004. Panel (a) shows production parameter (P) in mixing ratio per second and panel (b) shows destruction coefficient parameter (D) in per second, both from the Equation 2.1.

for the zonally averaged total column O_3 from 000UTC 1 July 2004 to 000UTC 15 August 2004. The NCEP GFS total column O_3 is compared with a 45 day model integration without assimilation of observations, initialized with the 000UTC 1 July 2004 high resolution operational NCEP GFS analysis (see Figure 2.2 (b)). From Figure 2.2 it can be seen that the main structure of the progression of O_3 over the 45-days is maintained in the model integration.

For the ozone, along with production-loss parameterization, the 2004 operational NCEP GFS model also includes Rayleigh damping and a parameterization of some of the sub-grid scale processes, such as vertical diffusion. Rayleigh damping is used to damp gravity waves caused by a rigid lid top boundary on the model. Vertical diffusion is the vertical turbulent eddy diffusion of momentum, water vapor and sensible heat. The 2004 operational O_3 model does not include the sub-grid scale process of convective mixing because, as mentioned earlier, the O_3 is primarily used for the computation of stratospheric radiative processes. However, for the assimilation of O_3 observations in the upper troposphere, the lack of convective mixing of the O_3 becomes an important issue.

2.1.2 Modified Trace Gas Convection

In the 2004 operational version of the NCEP GFS the cumulus convection is modeled by a simplified Arakawa-Schubert scheme (Arakawa and Schubert 1974; Grell 1993). This cumulus convection parameterization is formulated by dividing the atmosphere into a few layers and calculating a simplified cloud model in the grid

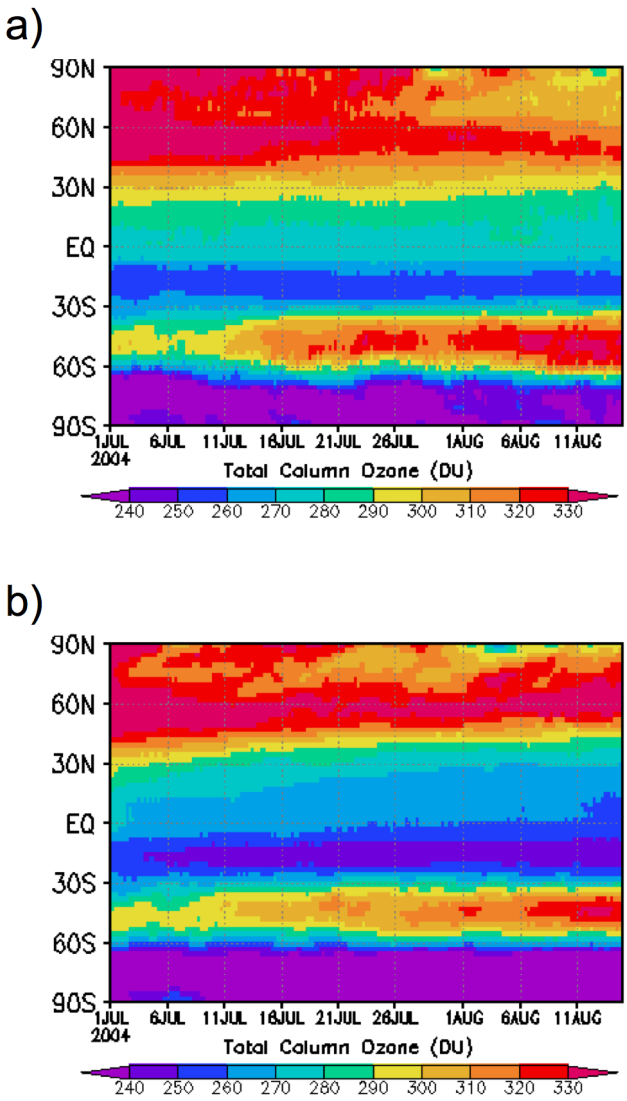

Figure 2.2: Zonally averaged total column O_3 in Dobson units (DU) from 000UTC 1 July 2004 to 000UTC 15 August 2004. Panel (a) shows the high resolution operational NCEP GFS analysis and panel (b) shows the 45-day model integration without assimilation of observations initialized with the 000UTC 1 July 2004 operational NCEP GFS analysis meteorological and O_3 fields and using NCEP GFS production-loss O_3 parameters.

space to provide the statistical effects of moist convection on the model variables. Hereafter, we refer to this parameterization as convective mixing. One of the effects of convection on the large scale atmospheric processes is the redistribution of momentum in the vertical. However, in the operational NCEP GFS, the only tracer affected by the cumulus convection parameterization is water vapor.

Our first modification to the 2004 operational NCEP GFS model is the addition of ozone and CO in the convective parameterization. The goal of a more sophisticated parameterization is to produce a more realistic vertical transport of the trace gases in the model. We implement the transport by using scalar momentum mixing as a template for the trace gas convective mixing. We discuss the verification of the effect of the changes we make to the model in Chapters 3 and 4.

The impact of the assimilation of trace gas observations on the meteorological fields is determined by the accuracy of the transport model, since the ensemble of transport models build the covariances between the uncertainties in the estimation of the meteorological variables (atmospheric flow) and the trace gases. Parameterized sub-grid scale processes, including that of atmospheric convection, do not provide a representation of the dynamics of the sub-grid scale process. Instead, they provide a representation of the expected effects of the sub-grid processes on the resolved larger scales (e.g. Emanuel 1994). Thus, we can expect to extract only limited information about the meteorological variables from the trace gas observations.

2.1.3 Modified O_3 Modeling

In addition to including convective mixing in the model of O_3, we also updated the production P and destruction coefficient D parameters (Equation 2.1) using the RAQMS model (Pierce et al., 2007). The RAQMS model is a state-of-the-art unified stratosphere-troposphere global chemical model. We use the RAQMS model reanalysis to improve upon the simple tropospheric chemical modeling of the production-loss parameters in the 2004 operational NCEP GFS model.

The RAQMS O_3 production-loss parameters are taken from the post INTEX-A mission $1.4^\circ \times 1.4^\circ$ reanalysis from 000UTC 1 July to 000UTC 15 August 2004. RAQMS uses the UW-Hybrid dynamics at its core with the meteorological fields initialized to the operational NCEP GFS analysis every 6 hours in the reanalysis. Time averaged RAQMS O_3 production-loss parameters were archived at 6-hour intervals and used to update the NCEP GFS production-loss every 6-hours, as opposed to every 10 days in the 2004 operational NCEP GFS, resulting in a better modeling of the diurnal changes of O_3 (There is a large diurnal variation in O_3 due to the primary component of formation and destruction from photochemical processes).

RAMQS utilizes a unified stratosphere/troposphere chemistry module developed to represent photochemical processes governing O_3 formation and destruction from the surface of the earth up to 60 km altitude in the Earth's atmosphere. The chemical formulation is based upon a family approach where closely coupled chemical species are handled as a unit. The partitioning of the families is based on photochemical equilibrium approximations. The continuity equations are solved for

each of 55 families and individual constituents. Equilibrium concentrations of 86 separate species are also determined. RAQMS includes a full treatment of tropospheric Non-Methane HydroCarbon (NMHC) chemistry (Pierce et al., 2007).

For the RAQMS reanalysis the following observations were assimilated: the Stratospheric (tropopause and above) HALogen Occultation Experiment (HALOE) observations, Stratospheric Aerosol and Gas Experiment (SAGE) II observations, and SAGE III (Rault and Taha, 2007) solar occultation observations. These observations were assimilated at 6 hour (0000 UT, 0600 UT, 1200 UT, 1800 UT) intervals to provide constraints on the stratospheric O_3 mixing ratios. Assimilation of global TOMS V8 cloud cleared total column O_3 observations were used to provide constraints on the RAQMS total column analysis. All of the observations were assimilated using a Statistical Digital Filter (SDF) assimilation system, an algorithm is based on Optimal Interpolation (OI) data assimilation (Stobie, 2000).

In Figure 2.3 we show the zonal average of the RAQMS O_3 production and destruction coefficient parameters for the 6 hour period from 000UTC to 600UTC 19 July 2004. In contrast to Figure 2.1, this figure shows spatially varying surface O_3 production-loss distribution due to variations in precursor emissions.

The production-loss parameterization modifications are tested by performing a 45-day integration of the model without assimilating any data. The model is initialized from the high resolution operational NCEP GFS analysis meteorological fields and from the RAQMS analysis O_3 fields on 000UTC 1 July 2004. The results (Figure 2.4) show improved behavior of the model. The differences between our NCEP GFS integration and the RAQMS analysis is partly due to the coarser

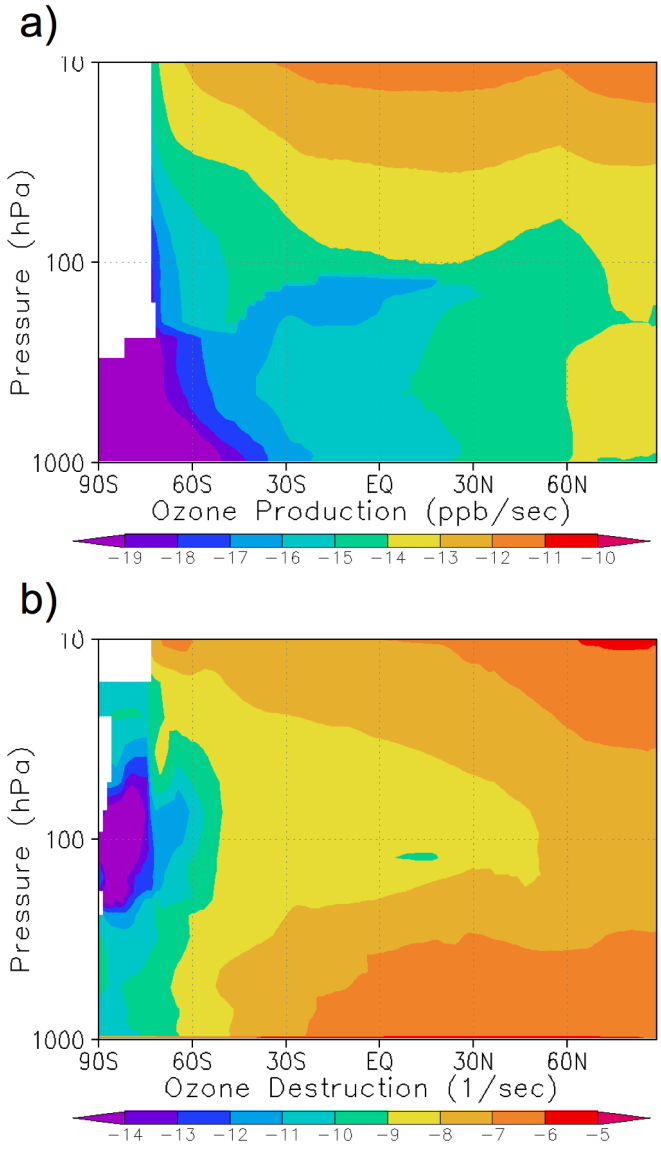

Figure 2.3: RAQMS O_3 production-loss parameters used in the modified 2004 operational NCEP GFS for the period of 000UTC to 600UTC 19 July 2004. Panel (a) shows production parameter (P) in mixing ratio per second and panel (b) shows destruction coefficient parameter (D) in per second, both from Equation 2.1.

stratospheric vertical resolution in our version of the NCEP GFS and partly due to the assimilation of the HALO and SAGE measurements constraining the stratospheric column in the RAQMS analysis. The stratospheric O_3 mechanisms used in RAQMS are from the Interactive Modeling Project for Atmospheric Chemistry and Transport (IMPACT) model, a model that has been known to have a climatological low bias in the stratosphere (Al-Saadi et al., 2004).

2.1.4 Modified CO Modeling

Unlike ozone, the operational form of the NCEP GFS model has never included carbon monoxide (CO) as a prognostic variable. We incorporated CO prediction capability into the model using the same tracer formulation as for the ozone. This includes applying the same sub-grid scale process parameterizations (Rayleigh damping, vertical diffusion and convective mixing) to the CO as to the ozone. One notable difference between CO and O_3 in the model is that the CO field is not used in the radiative process calculations and thus does not feedback on the meteorological fields within the model. As for ozone, the CO production-loss parameters are derived from the RAQMS model reanalysis and updated every 6-hours.

In the RAQMS model, climatological emissions of CO include anthropogenic and natural sources and are largely based on $1^\circ \times 1^\circ$ gridded data available from Global Emissions Inventory Activity (GEIA, cited 2009) and Emission Database for Global Atmospheric Research (EDGAR, cited 2009) with updates for Asian emissions from Streets et al. (2003). To augment the biomass burning inventories,

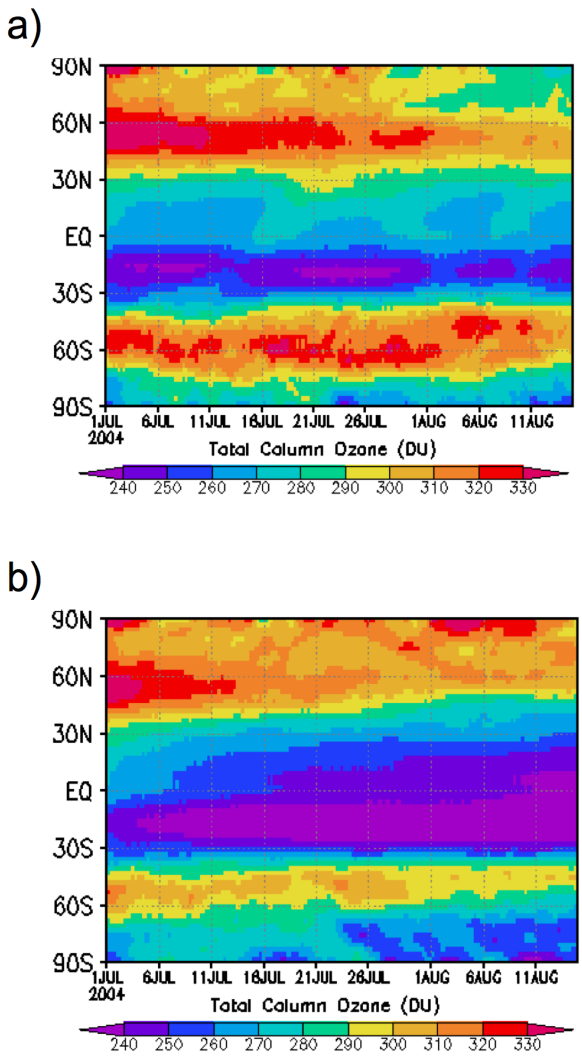

Figure 2.4: Zonally averaged total column O_3 in Dobson units (DU) from 000UTC 1 July 2004 to 000UTC 15 August 2004. Panel (a) shows the RAQMS analysis and panel (b) shows the 45-day model integration without assimilation of observations, initialized with the 000UTC 1 July 2004 operational NCEP GFS analysis meteorological fields and RAQMS analysis O_3 fields and using RAQMS production-loss O_3 parameters.

RAQMS uses a time-dependent ecosystem-based approach developed by Soja et al. (2004) to predict wildfire CO emissions. RAQMS extends this algorithm to predict global biomass burning emissions using MODerate Resolution Imaging Spectroradiometer (MODIS) thermal anomaly data to provide area burned estimates. More details on the CO chemistry and emissions in RAQMS is found in Pierce et al. (2007).

The sub-grid scale processes and production-loss parameterization modifications are tested by performing a 45-day integration of the model without assimilating any data. The model is initialized from the high resolution operational NCEP GFS analysis meteorological fields and from the RAQMS analysis CO fields on 000UTC 1 July 2004. The results of the integration are shown in Figure 2.5 along side the results from the RAQMS reanalysis. The figure shows the time series of zonally averaged total column CO. It is clear from these figures that there is good agreement between the two panels.

2.2 LETKF Assimilation

For all assimilation experiments in this study we use the Local Ensemble Transform Kalman Filter (LETKF) data assimilation system (Hunt et al., 2007) described in Szunyogh et al. (2008). Several previous experiments have been conducted with different implementations of this data assimilation system. An implementation of the Local Ensemble Kalman Filter (LEKF) (Ott et al., 2004), the precursor to the LETKF, on a reduced resolution 2001 operational version of the NCEP GFS atmo-

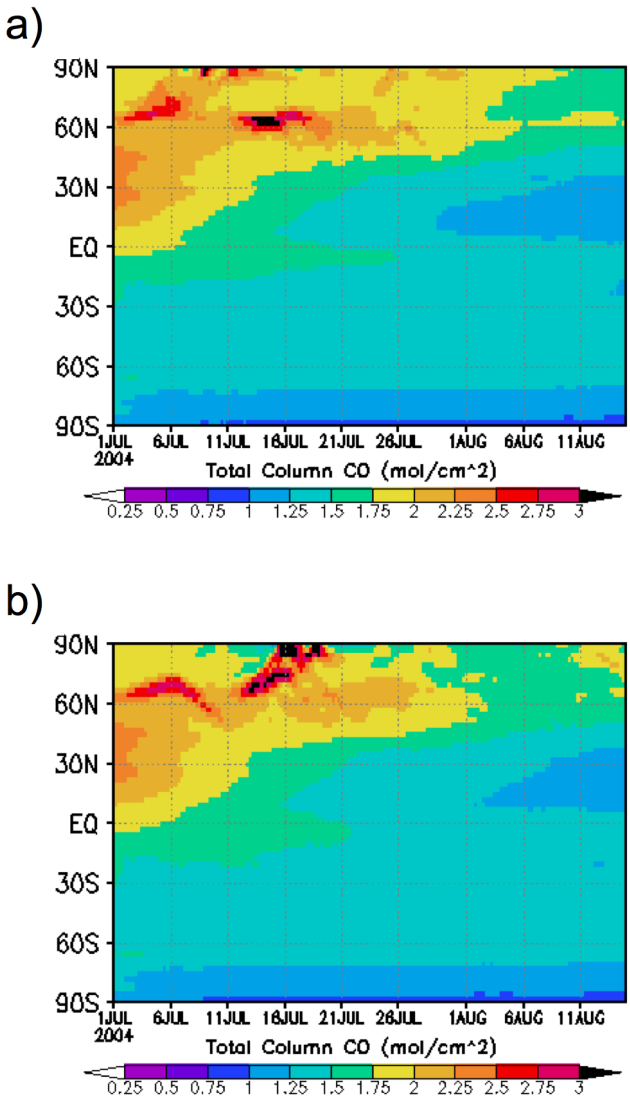

Figure 2.5: Zonally averaged total column CO in molecules cm^{-2} from 000UTC 1 July 2004 to 000UTC 15 August 2004. Panel (a) shows the RAQMS analysis and panel (b) shows the 45-day model integration without assimilation of observations, initialized with the 000UTC 1 July 2004 operational NCEP GFS analysis meteorological fields and RAQMS analysis CO field and using RAQMS production-loss CO parameters.

spheric model has been successfully tested using simulated observations (Szunyogh et al., 2005). The LEKF was also used to generate initial conditions for the assessment of predictability in the reduced resolution 2001 operational NCEP GFS model (Kuhl et al. 2007/Appendix B). An implementation of the LETKF assimilation scheme on a reduced resolution version of the 2004 operational NCEP GFS model has been successfully tested for the assimilation of observation of the real atmosphere Szunyogh et al. (2008). The same implementation of the LETKF on the NCEP GFS was also used to study atmospheric predictability by Satterfield and Szunyogh (2009). In addition, the implementation of the LETKF on the 2004 NCEP GFS was also used for the assimilation of microwave, AMSU-A (Advanced Microwave Sounding Unit), radiance observations by Aravequia et al. (Submitted).

The experiments in this dissertation are an extension of the aforementioned efforts in several aspects. First, our experiments are for the summer of 2004 while all earlier studies were for the winter of 2004. Secondly, our study is the first attempt to extend the LETKF-NCEP GFS analysis/forecast system to the assimilation and prediction of trace gas concentrations.

In what follows, we first introduce the major components of the data assimilation algorithm. Then, we discuss the conventional forms of retrieval observation operators as well as the modified form we use in our experiments. We also discuss our method for vertical localization, a key aspect of the LETKF, for retrievals, and the covariance inflation for O_3 and CO observations.

2.2.1 LETKF Algorithm

At analysis time t_n we assimilate observations from the observation time window

$$\tau_n = (t_n - \frac{\Delta t}{2}, t_n + \frac{\Delta t}{2}), \tag{2.4}$$

centered at analysis time t_n and with a time window width of Δt. We introduce the notation $\boldsymbol{\gamma}_n$ for the state space trajectory of the model in τ_n, that is,

$$\boldsymbol{\gamma}_n = \mathbf{x}\,(t)\,, t \in \tau_n, \tag{2.5}$$

where the vector $\mathbf{x}\,(t)$ is the finite-dimensional representation of the atmospheric state on the model grid. The inputs of the assimilation process are the vector of observations $\mathbf{y}_n^o$, from τ_n, and a K-member ensemble of analyses $\mathbf{x}_{n-1}^{a(k)}$, $k = 1,\ldots,$ K, from the previous analysis time $t_{n-1} = t_n - \Delta t$.

As all other current data assimilation systems, the LETKF consists of a forecast and a state update step. In the forecast step of the LETKF, each ensemble member is integrated for a time interval of $\frac{3}{2}\Delta t$, using the K members of the analysis ensemble $\mathbf{x}_{n-1}^{a(k)}$, $k = 1,\ldots,$ K, as initial conditions, to obtain an ensemble of background forecast trajectories $\boldsymbol{\gamma}_n^{b(k)}$, $k = 1,\ldots,$ K. In our current implementation of the LETKF, the members of the background ensemble are six-hour forecast trajectories starting at 3-hour forecast lead time and ending at 9-hour forecast lead time relative to t_{n-1}.

The formulation of the state update step of the LETKF, similar to that of all other modern data assimilation schemes, is based on the assumption that we have

the knowledge of an observation operator $\mathbf{h}(\boldsymbol{\gamma}_n)$ that satisfies the equation

$$\mathbf{y}_n^o = \mathbf{h}\left(\boldsymbol{\gamma}_n^t\right) + \boldsymbol{\epsilon}_n; t \in \tau_n. \tag{2.6}$$

Here, $\boldsymbol{\gamma}_n^t$ is the model representation of the (unknown) true system trajectory, and $\boldsymbol{\epsilon}_n$ is a vector of Gaussian random observation noise with zero mean and a known observation error covariance matrix $\mathbf{R}_n$. In practice, the observation operator typically consists of an interpolation of $\boldsymbol{\gamma}_n$ to the time and location of the observations and a conversion of the model variables to the observed quantities. In our implementation of the LETKF on the NCEP GFS, the time interpolation component of $\mathbf{h}(\boldsymbol{\gamma}_n)$ for all types of observations is performed by storing the background trajectories $\boldsymbol{\gamma}_n^{b(k)}$, $k = 1,\ldots, K$, with a 3-hour resolution and applying a linear interpolation to the stored model fields to obtain the ensemble of model states at the observation time with a one minute resolution.

In what follows, we discuss how to obtain an analysis $\mathbf{x}_n^a$ at time t_n, thus we drop the subscript n. The LETKF obtains the vector components of the analysis $\mathbf{x}^a$ independently for each grid point. We define a local state vector $\mathbf{x}_\ell$, which is composed of the model variables at model grid point ℓ. The LETKF generates a K-member ensemble of local analyses, $\mathbf{x}_\ell^{a(k)}$, $k = 1,\ldots, K$ by computing an ensemble of "weight" vectors $\mathbf{w}_\ell^{a(k)}$, $k = 1,\ldots, K$ such that

$$\mathbf{x}_\ell^{a(k)} = \mathbf{x}_\ell^b + \mathbf{X}_\ell^b \mathbf{w}_\ell^{a(k)} (1+\rho)^{\frac{1}{2}}. \tag{2.7}$$

Here, $\mathbf{x}_\ell^b$ is the ensemble mean of the local background state vectors $\mathbf{x}_\ell^{b(k)}$, $k = 1,\ldots, K$, while $\mathbf{X}_\ell^b$ is the matrix of the background ensemble perturbations, whose k-th column is the k-th background ensemble perturbation $\mathbf{x}^{b(k)} - \mathbf{x}^b$. Hereafter, we

denote the ensemble mean of a quantity, by simply dropping the superscript (k) that refers to a particular ensemble member. The weights $\mathbf{w}_\ell^{a(k)}$ are defined in section 2.2.2 and $\rho \geq 0$ is a multiplicative covariance inflation factor. In our implementation, ρ is a smoothly varying three-dimensional scalar field. We should note that in this implementation we are inflating the increment as well as the ensemble covariance.

Our best estimate of the state at location ℓ is the ensemble mean analysis

$$\mathbf{x}_\ell^a = \mathbf{x}_\ell^b + \mathbf{X}_\ell^b \mathbf{w}_\ell^a (1+\rho)^{\frac{1}{2}}. \tag{2.8}$$

The members of the global analysis ensemble, $\mathbf{x}^{a(k)}$, and the global analysis, $\mathbf{x}^a$, are obtained by collecting the local analyses, $\mathbf{x}_\ell^{a(k)}$ and $\mathbf{x}_\ell^a$, for all locations ℓ.

2.2.2 Conventional Observations

For the conventional (non-retrieval) observations, we compute the weight vectors $\mathbf{w}_\ell^{a(k)}$, $k = 1,\ldots, K$, and their ensemble mean, $\mathbf{w}_\ell^a$, by the following procedure: First, the observation operator $\mathbf{h}(\boldsymbol{\gamma})$ is defined. In the two horizontal spatial dimensions, $\mathbf{h}(\boldsymbol{\gamma})$ is a bilinear interpolation. Since the vertical coordinate in the NCEP GFS model is σ (defined by the ratio of the pressure to surface pressure), and the vertical position of the observations is given in pressure, the vertical interpolation for a given observation is carried out in three steps:

1. We calculate the pressure at each σ-level at the horizontal location of the observation by multiplying σ by the background surface pressure interpolated to the observational location.

2. We define 28 σ-layers, each bounded by a pair of σ- levels (the lowest layer is defined by the model surface and the lowest σ-level).

3. We find the σ-layer that contains the observation, and linearly interpolate the logarithm of the pressure using the pressure values at the two σ-levels that bound that layer.

Second, the observation operator $\mathbf{h}(\boldsymbol{\gamma})$ is applied to each member $\boldsymbol{\gamma}^{b(k)}$, $k = 1,\ldots,$ K, of the ensemble of background trajectories to obtain an ensemble $\mathbf{y}^{b(k)}$, $k = 1,\ldots,$ K, of the observable at the observation locations. The ensemble average $\mathbf{y}^b$ of the ensemble $\mathbf{y}^{b(k)}$, $k = 1,\ldots, K$, is computed and the matrix $\mathbf{Y}^b$ is constructed by taking its columns to be the vectors obtained by subtracting $\mathbf{y}^b$ from each ensemble member $\mathbf{y}^{b(k)}$, $k = 1,\ldots, K$.

Third, the localization is performed: for each location (grid point) ℓ, observations are selected for assimilation within a local neighborhood. The local neighborhood is defined to include all observations that are thought to have useful information about the atmospheric state at grid point ℓ. The selected observations form the local observation vector $\mathbf{y}^o_\ell$. The vector $\mathbf{y}^b_\ell$ and the matrixes $\mathbf{Y}^b_\ell$ and $\mathbf{R}_\ell$ are formed by selecting those vector components and matrix elements that are associated with the selected set of observations at ℓ. In the present study, we choose the localization neighborhood as follows:

1. In the horizontal direction, observations are considered within an 800-km radius of the location (grid point) ℓ. The influence of observations located further than 500 km from ℓ is reduced by multiplying the entries of R_ℓ^{-1} by a factor

$\mu(r) \leq 1$, which linearly tapers from one at r=500-km radius to zero at r=800 km radius.

2. In the vertical direction, observations are considered from a layer around ℓ. The depth of the layer is 0.35 scale height between model levels 1 and 15 (below $\sigma = 0.372$), and starting with level 15 the depth gradually increases with heights to reach 2 scale heights at the top of the model atmosphere (defined by $\sigma = 0.003$). (The scale height is defined by the vertical distance in which the surface pressure drops by a factor of $e = 2.718$.) Surface pressure observations are considered from the local horizontal region when the state is analyzed at a model grid point, that is at or below model level 15.

3. The surface pressure components of the state vector are treated differently from the other components: to obtain the surface pressure analysis at a location ℓ, we use all surface pressure observations from an 800 km radius of ℓ and all temperature and wind observations from a 800 km radius of ℓ between model levels 2 ($\sigma = 0.982$) and 5 ($\sigma = 0.916$). For all other observation types, the influence of the surface observation is tapered beyond a 500 km radius.

Fourth, the mean "weight" vector $\mathbf{w}_\ell^a$ is computed by

$$\mathbf{w}_\ell^a = \mathbf{P}_\ell^a \left(\mathbf{Y}_\ell^b\right)^T \mathbf{R}_\ell^{-1} (\mathbf{y}_\ell^o - \mathbf{y}_\ell^b). \tag{2.9}$$

Here, the analysis error covariance matrix $\mathbf{P}_\ell^a$ is defined by

$$\mathbf{P}_\ell^a = \left((K-1)\,\mathbf{I} + \left(\mathbf{Y}_\ell^b\right)^T \mathbf{R}_\ell^{-1} \mathbf{Y}_\ell^b\right)^{-1}. \tag{2.10}$$

Fifth, the matrix $\mathbf{W}_\ell^a = \left((K-1)\,\mathbf{P}_\ell^a\right)^{\frac{1}{2}}$ is computed.

Sixth, the "weight" vector $\mathbf{w}_\ell^a$ is added to each column of $\mathbf{W}_\ell^a$. The columns of the resulting matrix are the members of the ensemble of weight vectors $\mathbf{w}_\ell^{a(k)}$, $k = 1,\ldots, K$.

The above procedures are repeated for all ℓ.

2.2.3 Trace Gas Observation Operator

The trace gas observation operator is similar to the conventional observation operator. The observation operator algorithm for the O_3 observations consists of a horizontal bilinear interpolation followed by transformation of model units to observation units followed by interpolation of the model layers to the observation layers. The model variable units for ozone, and all trace gases in the 2004 operational NCEP GFS atmospheric model, are in mixing ratio. The observation operator algorithm for the carbon monoxide observations is similar, consisting of a horizontal bilinear interpolation. However, for CO both the model units and observation units are point measurement of the mixing ratio, therefore the observation operator is a vertical interpolation from the model grid points to the observation locations. Each step of the transformation operations is discussed in detail below, first for the O_3 observation operator and then for the CO observation operator. Then, we explain how we incorporate the a priori and smoothing information from the retrieval algorithm into the observation operators.

2.2.3.1 O_3 Observation Operator

The first step in formulating the O_3 observation operator is the bilinear horizontal interpolation from the model latitude-longitude to the observation latitude-longitude. In this step, the prognostic model variable for ozone, the volume mixing ratio, is horizontally interpolated. Volume mixing ratio is defined as the ratio of the number density of the gas to the total number density of the atmosphere. In other words, O_3 volume mixing ratio is the density of O_3 divided by the density of all constituents in a unit volume. We assume that the horizontal model grid is fine enough so that the O_3 varies linearly.

The second step is the conversion of each of the vertical profiles of mixing ratio into model layers in Dobson Units. The observations of retrieved SBUV/2 O_3 are reported in Dobson Units. Dobson Units (1 DU=1 mili-atm-cm or $2.68 \times 10^{16} O_3$ molecules cm^{-2} at standard temperature and pressure), is the equivalent depth per unit area of the vertically-integrated O_3 number density normalized to standard temperature and pressure. To convert between volume mixing ratio χ and Dobson Units χ_{DU} the mixing ratio of a layer is multiplied by the thickness of that layer and a constant conversion factor:

$$\chi_{DU} = \chi \cdot \Delta P \cdot g \cdot C_1. \tag{2.11}$$

Here, the model vertical pressure layer thickness ΔP is in Pascals, g is the gravitational constant ($\frac{m^2}{s}$) and the conversion factor C_1 is 2.1415×10^{-5} ($kg \cdot m^{-2} \cdot DU^{-1}$).

The final step is to convert the model layers to the SBUV/2 O_3 retrieval layers. A sample set of model layers compared to the observation layers is shown in

Figure 2.6. The model grid vertical profile consists of 28 layers specified by a fixed sigma coordinate and shown in Figure 2.6 (a) for a sample profile. The SBUV/2 O_3 retrieval vertical profiles consist of 21 log-pressure distributed layers shown in Figure 2.6 (b). The SBUV/2 O_3 retrieval layers are similar to the ground based Umkehr technique (Bhartia et al., 1996). Because Dobson Units are integrated quantities, all model layers contained within an observation layer are summed. When only part of a model layer is contained in the SBUV/2 layer, the percentage of the layer contained, as calculated in log pressure, is used to weight the amount of O_3 in the layer. The top model layer (layer 28) is disregarded because it extends to the top of the atmosphere and therefore, has an indeterminate thickness. Any SBUV/2 O_3 observation retrieval layer above layer 27 is not assimilated. For the model layers shown in Figure 2.6, the top 9 observations would be rejected leaving 12 SBUV/2 O_3 retrieval layers for assimilation.

2.2.3.2 CO Observation Operator

The first step in forming the carbon monoxide observation operator is the same as that of the O_3 with a bilinear horizontal interpolation from the model latitude-longitude to the observation latitude-longitude. In this step, the prognostic model variable for carbon monoxide, the volume mixing ratio, is horizontally interpolated. What follows is a vertical interpolation from the model point locations to the observation point locations. Since both the model variable and the observations are in volume mixing ratio, there is no need for unit conversion. The assimilated model

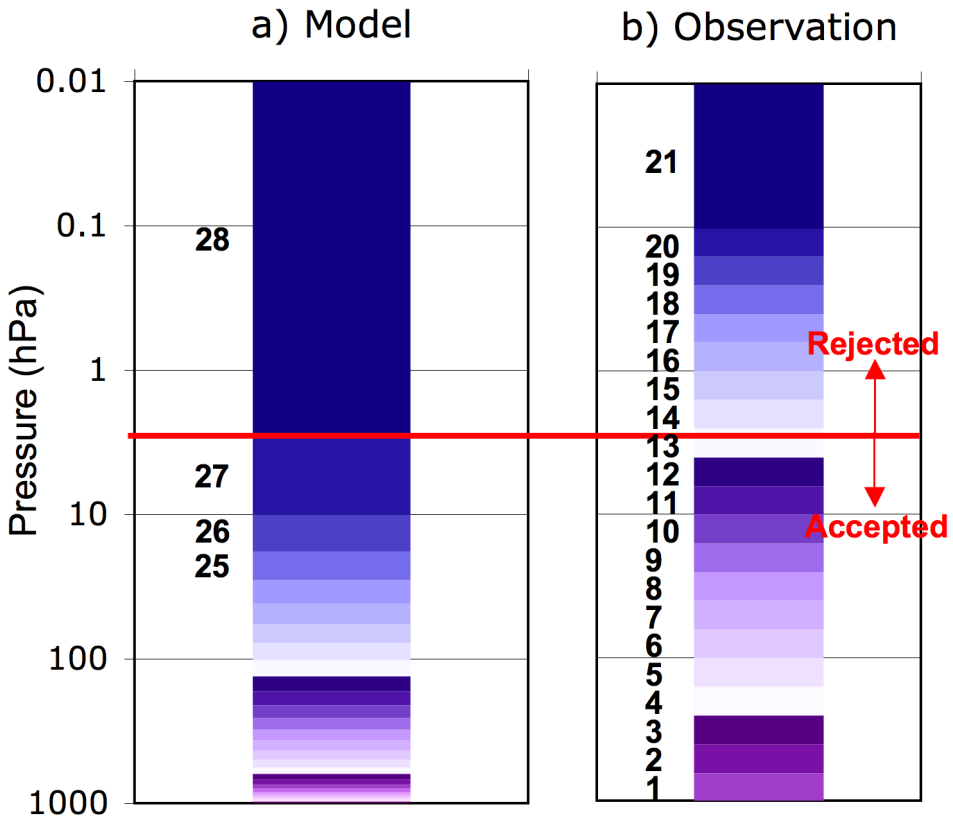

Figure 2.6: Model layers for a sample vertical profile and observation layers for all SBUV/2 O_3 retrievals. The top four model levels are labeled and all of the observation levels are labeled. The red line demarcates which observation layers are accepted for assimilation and which are rejected.

units for CO are in mixing ratio parts per part (ppp) by volume. The MOPITT CO data set includes retrieval profiles with 7-levels in the vertical.

2.2.4 Modified Retrieval Observation Operator

We design an observation operator $\mathbf{h}(\boldsymbol{\gamma})$ (defined in section 2.2.1 by Equation 2.6) for retrievals based on the approach described in Rodgers (2000). This approach takes into account that both the version 8 SBUV/2 O_3 retrieval observations (Bhartia et al., 2004) and the MOPITT CO retrieval observations (Emmons et al., 2004) are produced by a vertical smoothing approach. Our redesigned observation operators compares a properly smoothed model state to the retrieval.

Rodgers (1990) characterizes the vertical profiles retrieved from remote sounding measurements using an a priori vertical profile and averaging kernel (first defined by Backus and Gilbert 1970). We use the notation of Rodgers (2000) with the exception that we replace $\mathbf{x}$ with $\mathbf{z}$, to avoid creating a confusion between model states that we have been denoting with $\mathbf{x}$ and atmospheric profiles that we denote with $\mathbf{z}$

The derivation of the modified observation operator begins with observing that the relationship between the observed atmospheric radiance vector $\boldsymbol{\xi}$ and the state of the atmosphere vertical profile vector $\mathbf{z}$ is

$$\boldsymbol{\xi} = \mathbf{F}\left(\mathbf{z}^t\right) + \boldsymbol{\epsilon}_{\boldsymbol{\xi}}. \tag{2.12}$$

In Equation 2.12 the forward model $\mathbf{F}$ transforms the atmospheric vertical profile $\mathbf{z}^t$ into a radiance $\boldsymbol{\xi}$. The components of $\mathbf{z}^t$ represent the true state of the atmosphere at the vertical levels which are used in the radiative transfer model that $\mathbf{F}$ represents.

The vector $\boldsymbol{\epsilon_\xi}$ represents the noise in the retrieval, which is due to the noise in the observations and to the random part of the error in the forward model.

The retrieved vertical profile $\hat{\mathbf{z}}$ is obtained from the radiance $\boldsymbol{\xi}$ using the Kalman Filter state update equation:

$$\hat{\mathbf{z}} = \mathbf{z_a} + \mathbf{G_\xi}(\boldsymbol{\xi} - \mathbf{K}\mathbf{z_a}). \tag{2.13}$$

Here $\mathbf{K}$ is the linearization of $\mathbf{F}$ about $\mathbf{z} = \mathbf{z_a}$, where $\mathbf{z_a}$ is the a priori vertical profile, and $\mathbf{G_\xi}$ is the retrieval gain matrix (or Kalman gain matrix). The a priori $\mathbf{z_a}$ for the computation of the retrieval should not be confused with the a priori (background) $\mathbf{x}^b$ used in the data assimilation.

It can be shown (Rodgers 2000 section 2.3.2.2) that Equation 2.13 can be written as

$$\hat{\mathbf{z}} = \mathbf{z_a} + \mathbf{A}(\mathbf{z}^t - \mathbf{z_a}) + \hat{\boldsymbol{\epsilon}}. \tag{2.14}$$

This form assumes that $\mathbf{F}(\mathbf{z})$ is linear, i.e., $\mathbf{F}(\mathbf{z}) = \mathbf{K}\mathbf{z}$. We can see that the true state of the atmosphere $\mathbf{z}^t$ is not directly comparable to the retrieval $\hat{\mathbf{z}}$. Smoothing by the matrix $\mathbf{A}$ (which is called the averaging kernel matrix), as well as information from the a priori vertical profile must also be considered.

A correct formulation of the observation operator for satellite retrievals should incorporate Equation 2.14. This modified observation operator for satellite retrievals $\hat{\mathbf{h}}(\boldsymbol{\gamma})$ is:

$$\hat{\mathbf{h}}(\boldsymbol{\gamma}) = \mathbf{z_a} + \mathbf{A}(\mathbf{h}(\boldsymbol{\gamma}) - \mathbf{z_a}) + \hat{\boldsymbol{\epsilon}}. \tag{2.15}$$

To illustrate the differences between the modified and the conventional observation operators, we compute $\mathbf{e}$, which is defined by the difference between the retrieval $\hat{\mathbf{z}}$

and the observation operator $\mathbf{h}\left(\boldsymbol{\gamma}^t\right)$ of the model representation of the (unknown) true system $\boldsymbol{\gamma}^t$ system trajectory. For the unmodified observation operator (defined in section 2.2.3.1) $\mathbf{e}$ would be:

$$\mathbf{e} = \hat{\mathbf{z}} - \mathbf{h}\left(\boldsymbol{\gamma}^t\right). \tag{2.16}$$

A properly designed observation operator, on the other hand, should map the true atmospheric trajectory to the true atmospheric profile $\mathbf{h}\left(\boldsymbol{\gamma}^t\right) = \mathbf{z}^t$ then Equation 2.16 is equivalent to:

$$\mathbf{e} = \hat{\mathbf{z}} - \mathbf{z}. \tag{2.17}$$

Substituting Equation 2.14 into Equation 2.17:

$$\mathbf{e} = \mathbf{z_a} + \mathbf{A}(\mathbf{z} - \mathbf{z_a}) - \mathbf{z} + \hat{\boldsymbol{\epsilon}}, \tag{2.18}$$

that is,

$$\mathbf{e} = (I - \mathbf{A})(\mathbf{z_a} - \mathbf{z}) + \hat{\boldsymbol{\epsilon}}. \tag{2.19}$$

When the averaging kernel is the identity, Equation 2.19 becomes $\mathbf{e} = \hat{\boldsymbol{\epsilon}}$. This equation states, as it should always be the case, that when the observation operator is applied to the true atmospheric trajectory, $\mathbf{e}$ is equal to the random observation noise, in accordance with Equation 2.6. For any other averaging kernel, there is a contribution of the difference between the a priori and the true state to $\mathbf{e}$, which is an undesirable behavior. Such an $\mathbf{e}$ would move the state estimate from the true state towards the a priori, which typically reflects climatology. This would also have the added negative effect of introducing strongly correlated observation errors. In the extreme case when the averaging kernel is close to zero, which occurs when there is

little contribution from the actual observation to the retrieval, the retrieval becomes approximately equal to the a priori; and the difference between the a priori and the true state dominates the retrieval. In contrast, when we apply the modified form of the observation operator (Equation 2.15) to the true trajectory $\boldsymbol{\gamma}^t$, Equation 2.16 becomes

$$\mathbf{e} = \mathbf{z_a} + \mathbf{A}(\mathbf{z} - \mathbf{z_a}) + \hat{\boldsymbol{\epsilon}} - (\mathbf{z_a} + \mathbf{A}(\mathbf{z} - \mathbf{z_a})), \tag{2.20}$$

that is:

$$\mathbf{e} = \hat{\boldsymbol{\epsilon}}, \tag{2.21}$$

as it should be when the observation operator operates on the true state.

2.2.5 Localization

An important issue we have to address is the nonlocal nature of the observation operator for retrievals: in contrast to the case of the conventional observations, where the observation operator for a given observation depends on the model state only at the nearby grid points, the retrievals depend on the smoothing and the a priori for the entire vertical profile. This suggests that the vertical component of the localization strategy, implemented in step three of the LETKF, should be modified for the retrieval observations. Our modified data selection strategy is based on the averaging kernel for each retrieval observation (the averaging kernels are the rows of the **A** matrix from Equation 2.14). The averaging kernel is the sensitivity of the retrieval to the true state and are peaked functions which peak at the level where the retrieval is most sensitive to the true state.

We apply a cut-off-based observation strategy similar to the one suggested by Fertig et al. (2007) for radiances: we assimilate the retrieval at all model levels where the averaging kernel is larger than 1/2 the peak value of the averaging kernel. In Figure 2.7 we show the averaging kernel for a random observation of SBUV/2 O_3 retrieval number 10. Since for the retrieval in Figure 2.7, the peak value is about 0.4, we assimilate the retrieval at all levels where the averaging kernel is larger than 0.2. This retrieval in Figure 2.7 is assimilated at model levels 26 and 27. The vertical localization we described here replaces the third step of the LETKF algorithm for retrieval. The horizontal localization for the retrievals is the same as that used by the conventional observations.

2.2.6 Covariance Inflation

The multiplicative covariance inflation ρ in Equation 2.8 for the conventional observations was determined by numerical experimentation. In Figure 2.8 we show a map of the temporally constant ρ given in percent. This is only applied when observations are assimilated. For the trace gas retrievals the multiplicative covariance inflation is set to be spatially and temporally constant value of 5% for both the O_3 and CO observations. This value was determined by numerical experimentation by varying the inflation factor between 2% and 10%.

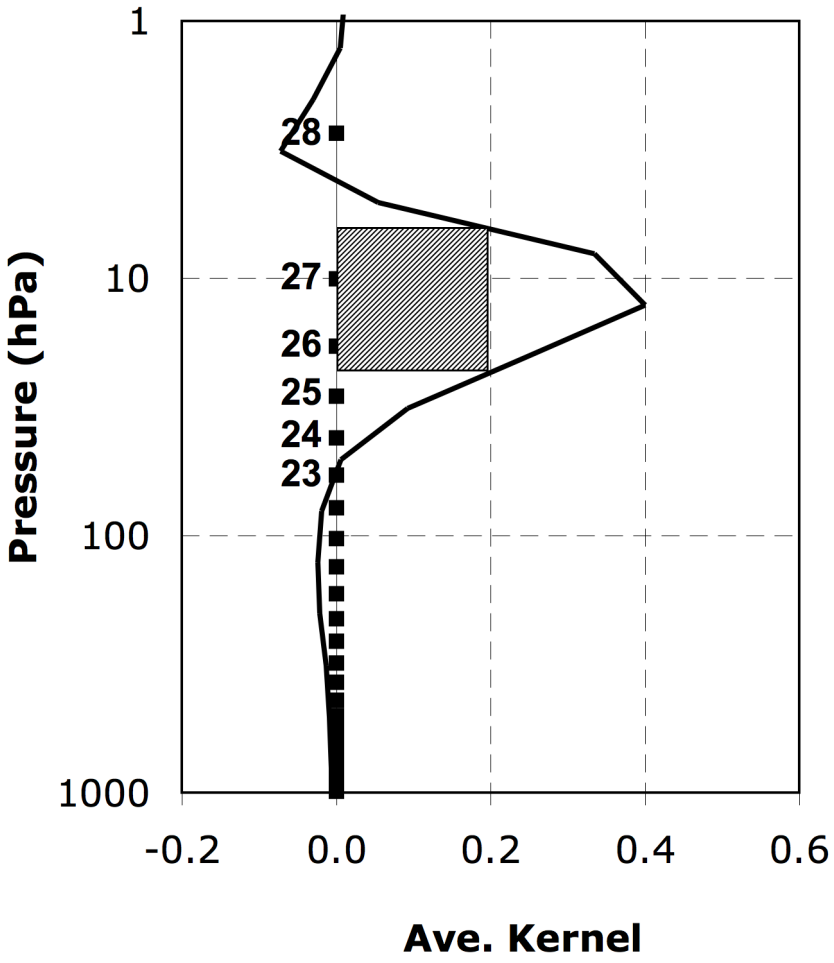

Figure 2.7: Averaging kernel for SBUV/2 O_3 retrieval number 10. The model levels are shown as black squares and the top six model levels are labeled. Shading indicates the model layers in which the retrieval is assimilated.

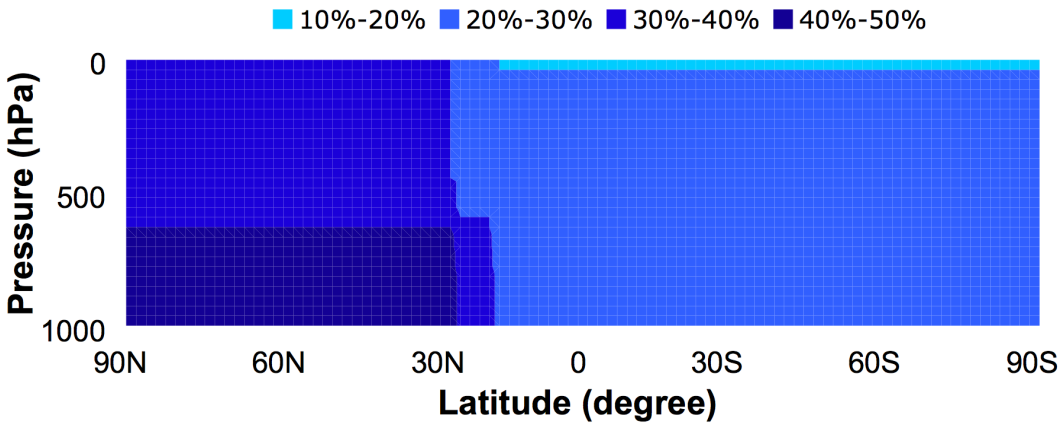

Figure 2.8: Percent multiplicative covariance inflation for conventional meteorological fields.

Chapter 3

O_3 Assimilation Experiments

In this chapter, we first describe the observations we assimilate and the observations we use for verification. Then, we discuss the impact of the modifications we made to the model. Finally, we report the results from the multivariate assimilation of SBUV/2 O_3 retrievals and meteorological observations.

3.1 O_3 Observations

We assimilate two sets of observations: the conventional meteorological observations which are assimilated as point measurements, and the satellite O_3 observations which are assimilated as retrievals. There are four sets of data we use to verify our analyses and forecasts. The first set of verification data is the high resolution operational NCEP GFS analyses. The second set is the radiosonde observations which we use only for the verification of forecasts. These two sets of data are used to verify the meteorological fields. The third set of verification data is aircraft observations of O_3 from the DC-8 flights of the INTEX-A experiment (Singh et al., 2006). This set of data we use to verify the tropospheric O_3 fields over the United States and southern Canada. The fourth set of verification data is ozonesonde observations from the IONS (INTEX Ozonesonde Network Study) sonde network from the INTEX-A experiment (Thompson et al., 2007a). This set of data we use to verify

the upper tropospheric and lower stratospheric O_3 fields over the United States and southern Canada. All of these data sets are described in this section, except for the high resolution operational NCEP GFS analyses results which were discussed in section 2.1.1.

3.1.1 Assimilated Meteorological Observations

The conventional meteorological observations are obtained from a database that includes all non-radiance observations operationally assimilated at NCEP between 000UTC 1 July 2004 and 000UTC 15 August 2004. We also exclude all surface observations except for the surface pressure and the scatterometer wind measurements over oceans (Szunyogh et al., 2008). These measurements were part of the set of observations assimilated in the high resolution operational NCEP GFS analysis. A map of the horizontal distribution of surface pressure, temperature and wind observations for +/- 3-hours on 000UTC 19 July 2004 is found in Figure 3.1, Figure 3.2 and Figure 3.3.

A subset of the temperature and wind observations (see Figure 3.2 and Figure 3.3) are the radiosonde observations (Figure 3.4). The radiosonde observations are used for the verification of the forecasts of the meteorological fields.

3.1.2 Assimilated O_3 Observations

The O_3 observations are from the Solar Backscatter UltraViolet generation 2 (SBUV/2) instrument O_3 retrievals deployed on the NOAA-16 and NOAA-17 satel-

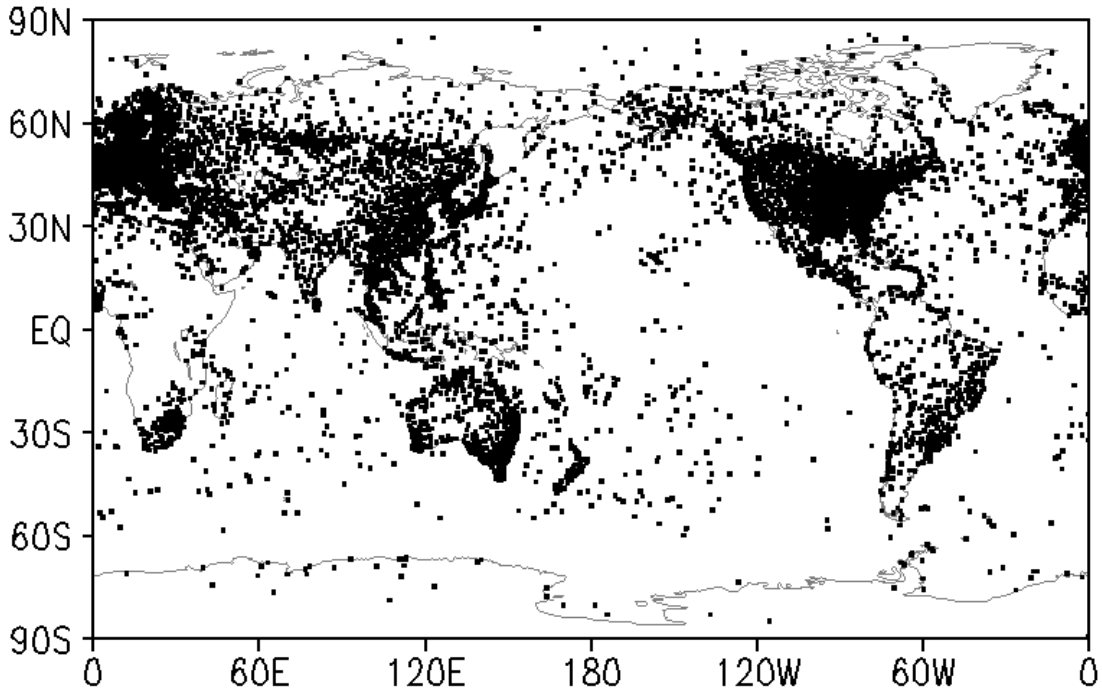

Figure 3.1: Surface pressure observations +/- 3-hours 000UTC 19 July 2004.

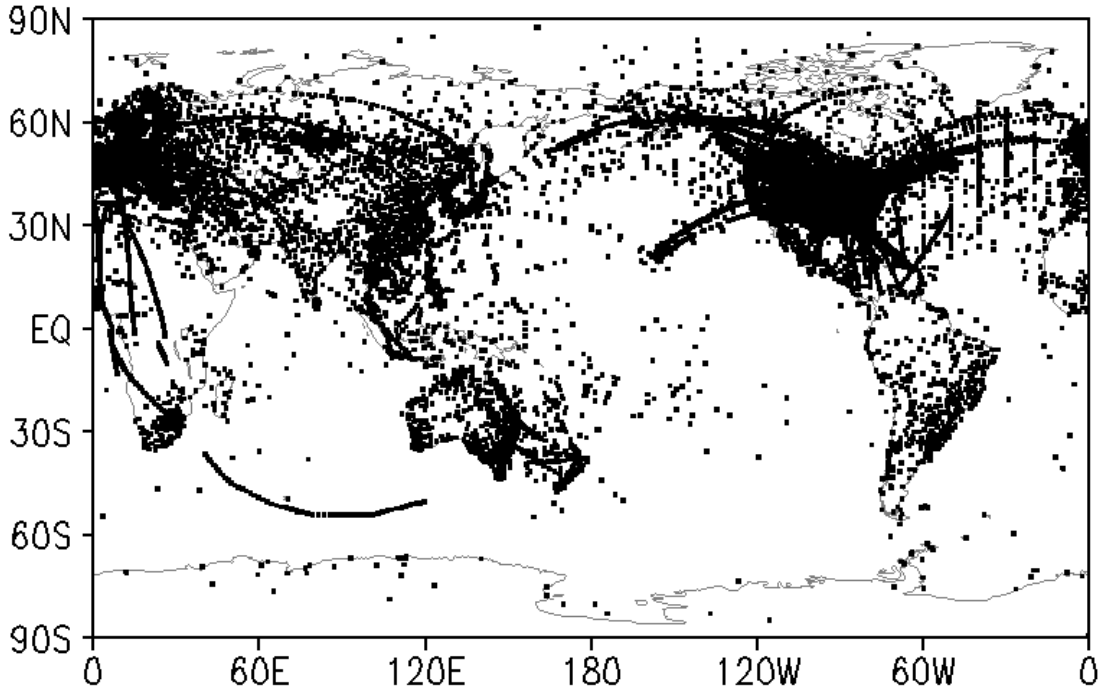

Figure 3.2: Horizontal temperature observation locations +/- 3-hours 000UTC 19 July 2004 including surface temperatures, radiosonde and aircraft measurements.

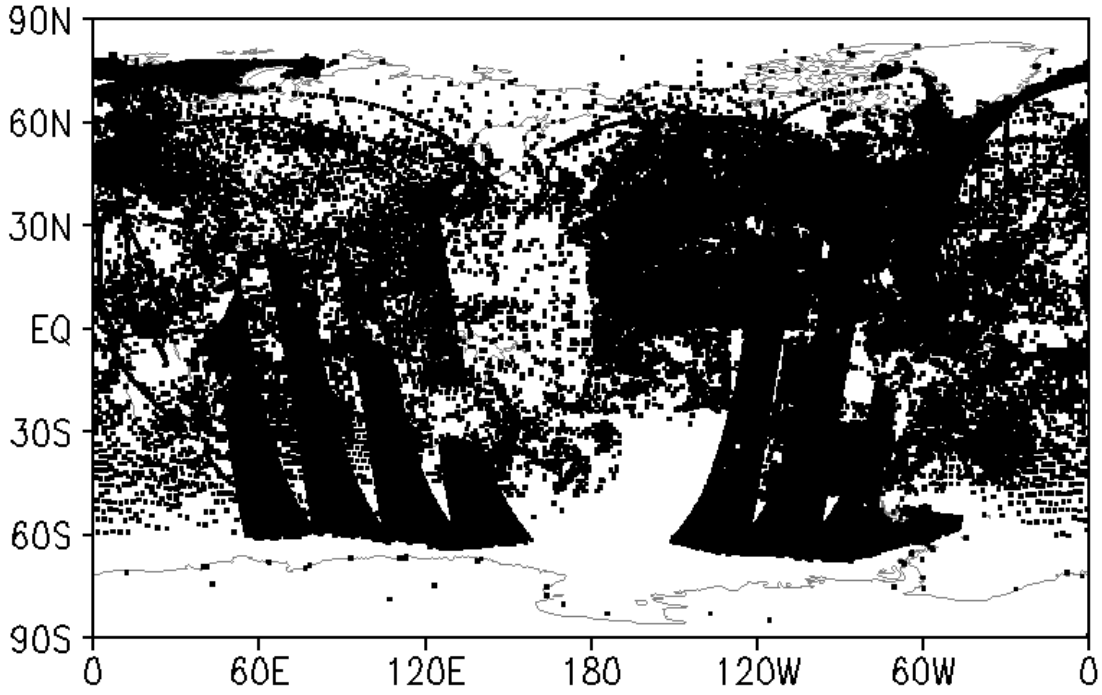

Figure 3.3: Horizontal wind observation locations +/- 3-hours 000UTC 19 July 2004 including radiosonde, aircraft and satellite-derived wind measurements over the oceans.

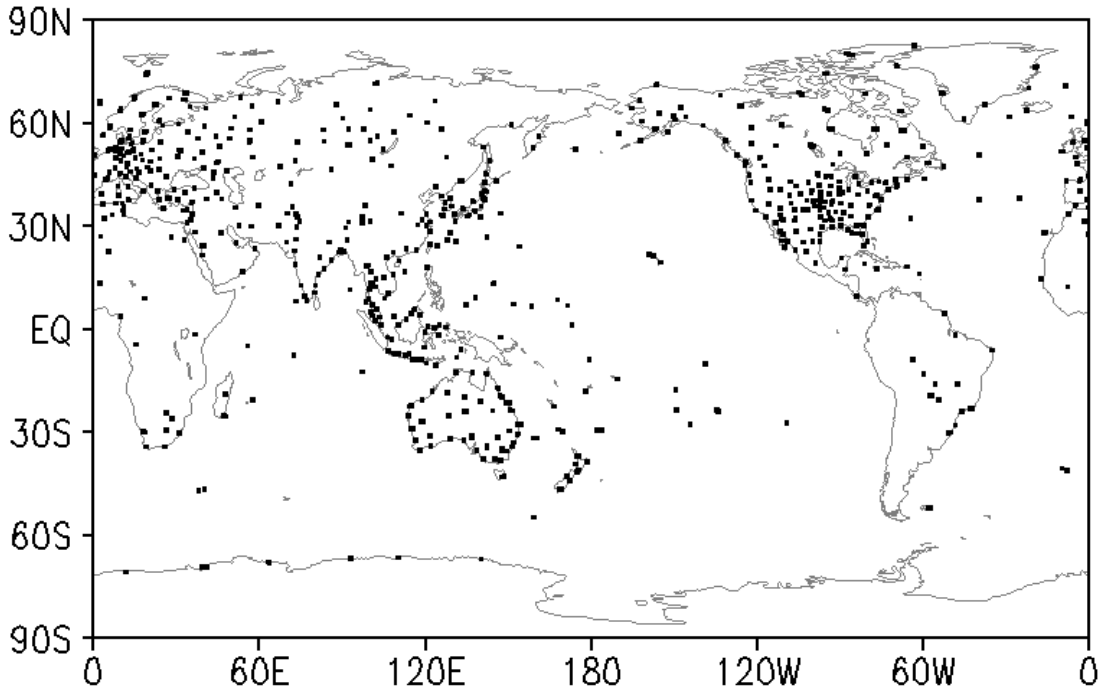

Figure 3.4: Horizontal wind and temperature observation locations +/- 3-hours 000UTC 19 July 2004 including only radiosonde measurements.

lites between 000UTC 1 July 2004 and 000UTC 15 August 2004 (Heath et al. 1975, Hilsenrath et al. 1995). This instrument measures the ratio of the backscattered Earth radiances to the incident solar irradiance, or the geometrical albedo, to derive total O_3 and vertical O_3 profiles. We assimilate the vertical O_3 profiles produced by the version 8 algorithm discussed in Bhartia et al. (2004). The version 6 retrieval observations were also part of the data set assimilated in the high resolution operational NCEP GFS analysis. A map of 6 hours worth of observations is shown in Figure 3.5. Every six hours, approximately 300 vertical profiles of O_3 are retrieved from the SBUV/2 instruments. The retrieval profiles normally consist of 12-layers in the vertical (see section 2.2.3.1).

The observation error range on these retrievals is 5-10% of the retrieved value. Errors were calculated through experiments comparing SBUV/2 retrievals to ozonesondes, LIDAR and microwave measurements, and with SAGE II and HALOE satellite data records (McPeters et al., 2004).

Reported with the SBUV/2 O_3 retrieval observations are three other important pieces of information: the variances of the retrieval layers $\hat{\boldsymbol{\epsilon}}$, the a priori vertical profile $\mathbf{z_a}$ and the averaging kernel matrix $\mathbf{A}$. We are provided with the error variances of the SBUV/2 O_3 retrieval layers but not with the covariance information. Within the vertical profile, the covariance between the retrieval layers is significant, thus neglecting the covariance information most likely degrades the quality of our analyses.

The a priori vertical profile for the SBUV/2 O_3 retrievals varies only by month and latitude, with 18 latitudinal zones. The climatological SBUV/2 O_3 retrieval a

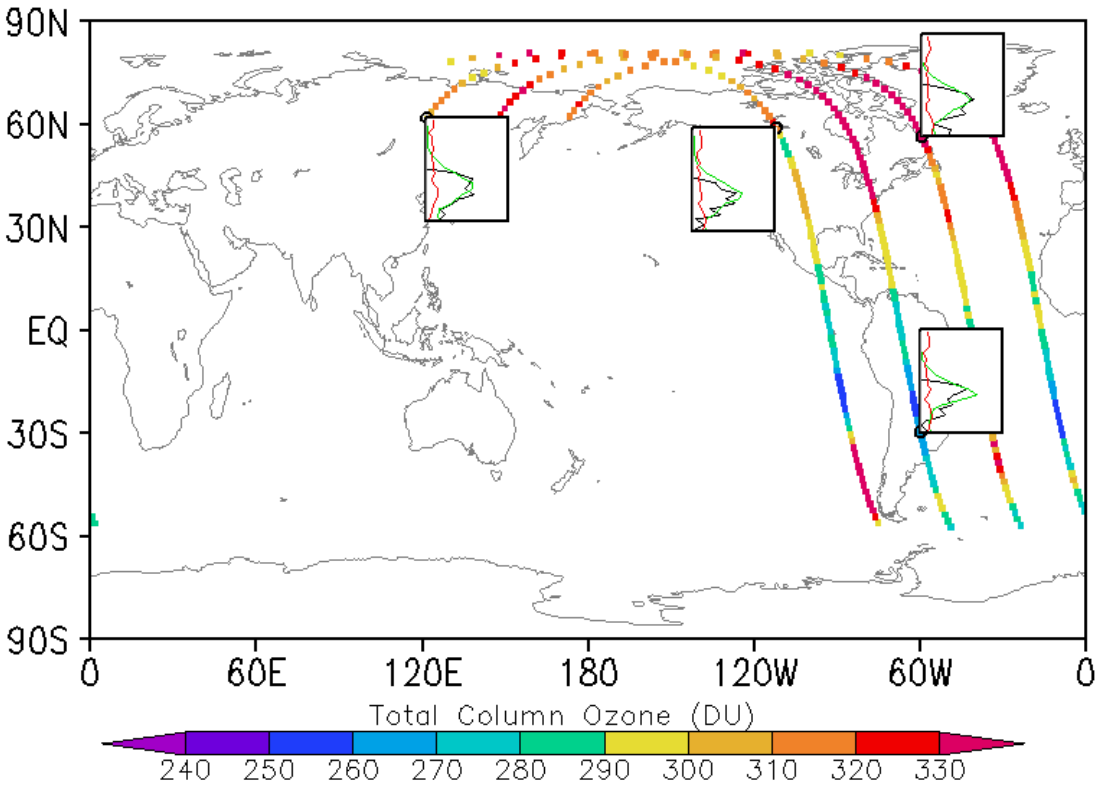

Figure 3.5: SBUV/2 O_3 retrieval observations +/- 3-hours 000UTC 19 July 2004. Colored symbols show total column O_3 amounts in Dobson Units. Inset figures show Dobson Unit vertical profiles with ordinate log pressure from 1000 to 0.1hPa and abscissa from 0 to 80DU. The inset figures show retrievals (black), retrieval error (red), and a priori vertical profile (green).

priori vertical profile was constructed with a single a priori error covariance matrix which produces averaging kernels that are minimally distorted from a Gaussian shape and peak at the correct altitudes (Bhartia et al., 2004).

A unique averaging kernel matrix is provided for each SBUV/2 O_3 retrieval. The averaging kernel matrix **A** is explicitly provided for each vertical profile. The SBUV/2 O_3 retrieval averaging kernels vary very little in either the short-term or long-term (Bhartia et al., 2004).

3.1.3 O_3 Verification Aircraft Observations

In situ O_3 data were obtained by instruments on board the NASA DC8 aircraft during INTEX-A. The flight tracks are shown in Figure 3.6. The observations were collected by M. Avery using a NO-O3 Chemiluminescesnse Detector (CLD). Certain chemical reactions release part of their energy in the form of light, chemiluminescence. When nitric oxide, NO, reacts with O_3 it emits red light. The measurements are performed by combining pure reagent nitric oxide (NO) with incoming sample air in a small volume reaction chamber, and by measuring light from the resulting nitrogen dioxide (NO2) chemiluminescence. The system is a fast response, high precision instrument with accuracy of 1ppb/s (Singh et al., 2006). The system is described in Avery et al. (2001) and Avery cited 2009. The accuracy and density of this data set makes it extremely useful for tropospheric verification of our experimental results.

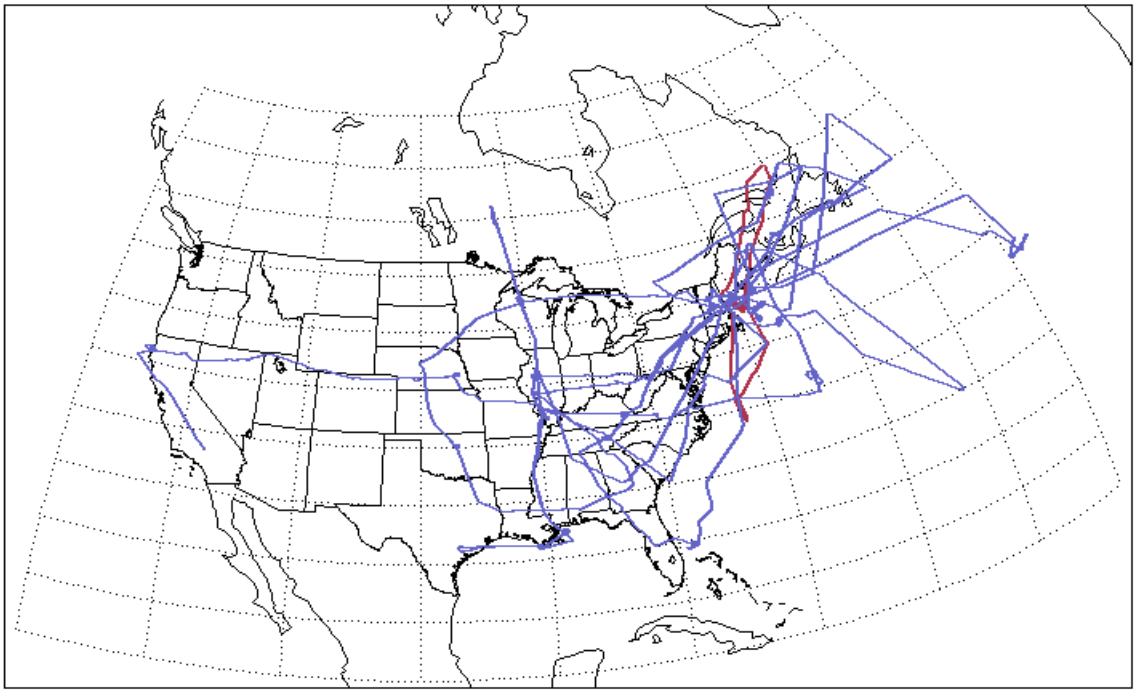

Figure 3.6: INTEX-A DC-8 flight tracks between 11 July 2004 and 15 August 2004. Flight track of 22 July 2004 is shown in red.

3.1.4 Ozonesonde Verification Observations

The ozonesonde data during the INTEX-A mission was collected durring the IONS project. The stations are shown in Figure 3.7. At five IONS sites (Trinidad Head, Houston, Pellston, Narragansett, the R/V Ronald H. Brown), soundings were made daily between noon and 1400 local time. The remaining stations launched midday 1–3 times per week, except for Sable Island, where the ozonesonde accompanied the standard 2300 UTC radio sounding. This provided multiple daily ozonesonde launches throughout the continental United States and southern Canada. The frequency and density of the data set makes it extremely useful for upper tropospheric and lower stratospheric verification of our experimental results.

Soundings were made with ECC (Electrochemical Concentration Cell) sondes, first developed by Komhyr (1969). The ECC sondes have an accuracy in the troposphere and lower stratosphere of about 5-10% of the measured value. The precision of the sondes, defined as the reproducibility of a single sounding, is 5-7%. Given the time response and ascent rate, the ECC sondes effective vertical resolution is 100m (Thompson et al., 2007b).

3.2 Impact on O_3 from Modeling Modifications

The purpose of the experiments presented in this section is to evaluate the impact of modifications to the NCEP GFS to improve the modeling of O_3 . In these experiments, we assimilate the meteorological observations with the LETKF, but we do not assimilate ozone. The O_3 field between the analysis cycles is carried by

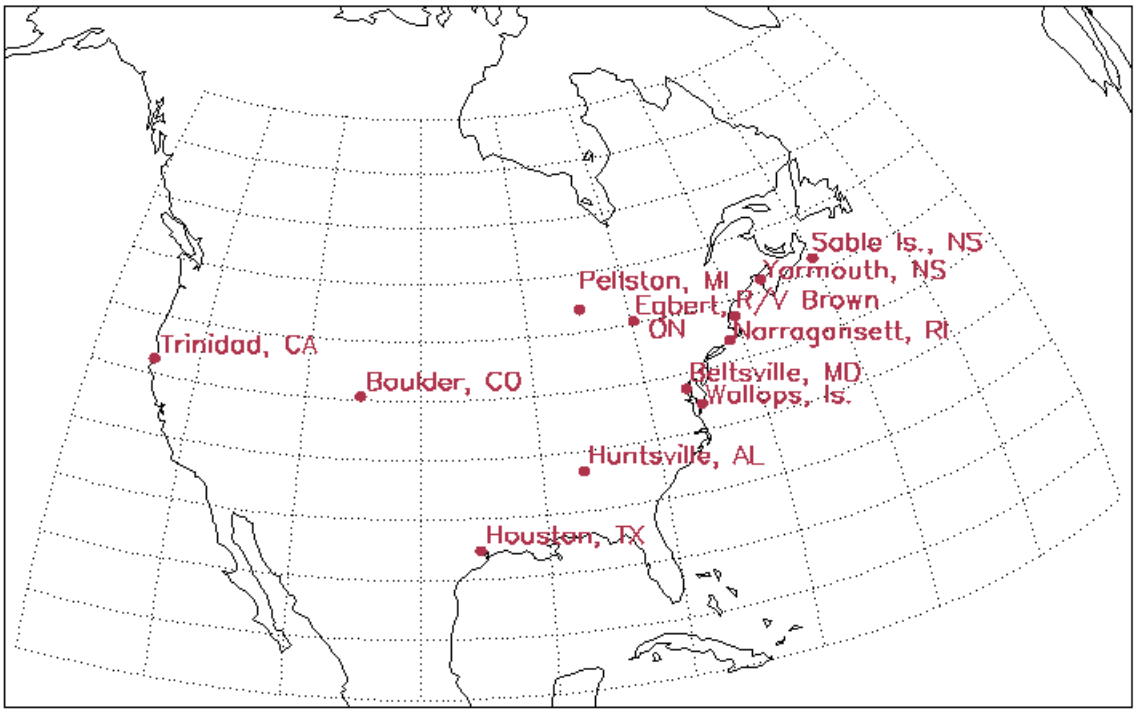

Figure 3.7: Map of IONS sites in July and August 2004, with the R/V Brown operating in the Gulf of Maine.

the background. The initial O_3 field for the experiment with the NCEP-GFS O_3 production-loss terms is the NCEP analysis. The initial O_3 field for the experiment with the RAQMS O_3 production-loss terms is the RAQMS analysis interpolated to the NCEP GFS grid.

To evaluate the impact of the modifications to the model on the tropospheric O_3 field, we compare the model simulated O_3 field with the aircraft data (Figure 3.8). In this figure we compare the modeled O_3 field from the NCEP GFS with the in situ O_3 data collected between 10 July 2004 and 15 August 2004. The modeled fields are compared to the measurements by interpolating the assimilated chemical fields to the flight tracks and sampling the model at the frequency of the in situ measurements. Both the modeled and the in situ aircraft measurements are collected in 50 hPa pressure bins and then the median statistic is calculated for each bin (Pierce et al., 2007).

In Figure 3.8 the blue line shows the analysis profile for the case in which the operational NCEP GFS parameterization of O_3 production-loss (see Figure 2.1) is used. As expected, due to the lack of realistic tropospheric O_3 production-loss, this configuration does a very poor job, particularly near the surface. The green line shows the profile using the RAQMS production-loss parameterization (see Figure 2.3). Comparing the blue and the green lines, we can see clear improvements from the production-loss parameterization modification. The red line shows the analysis profile result for the case in which, in addition to the use of the RAQMS provided O_3 production-loss values, convective mixing of the O_3 is included in the model. It can be seen that including convective mixing of the O_3 greatly improves the vertical

distribution of the O_3 in the troposphere; when no convective mixing is included, there is an excessive amount of O_3 found in the upper troposphere. Convective mixing transports lower concentrations of O_3 at the surface to the upper troposphere.

To evaluate the model modification impact on the upper tropospheric and lower stratospheric O_3 field, we compare the model simulated O_3 fields with the in situ ozonesonde data collected by instruments launched on sondes during INTEX-A between 1 July 2004 and 15 August 2004 (Figure 3.9). The model O_3 profiles in this figure are obtained by interpolating the O_3 filed from the model to the full resolution ozonesonde and sampling the modeled fields at the frequency of the ozonesonde measurements. Time averaged mean, mean bias, RMS errors and correlations are all shown in Figure 3.9.

In Figure 3.9 we show clear improvement by using RAQMS production-loss values instead of the original NCEP GFS in the troposphere, similar to what we saw in Figure 3.8. We also see clear improvement by including convective mixing of O_3 in the troposphere (panels (b) and (c)). In contrast, no such clear improvement is seen in the stratosphere from using RAQMS production-loss values instead of the original NCEP GFS. This is due to the careful tuning of the production-loss parameterization in the 2004 operational NCEP GFS model as well as the known bias in the RAQMS stratospheric O_3 modeling (discussed in section 2.1.3).

In the experiments reported above, O_3 observations were not assimilated, thus there was no direct impact on the analysis of the meteorological fields from ozone. However, through stratospheric radiative processes, which are included in the GFS, there may be a potential impact of the improved O_3 modeling on the analysis of

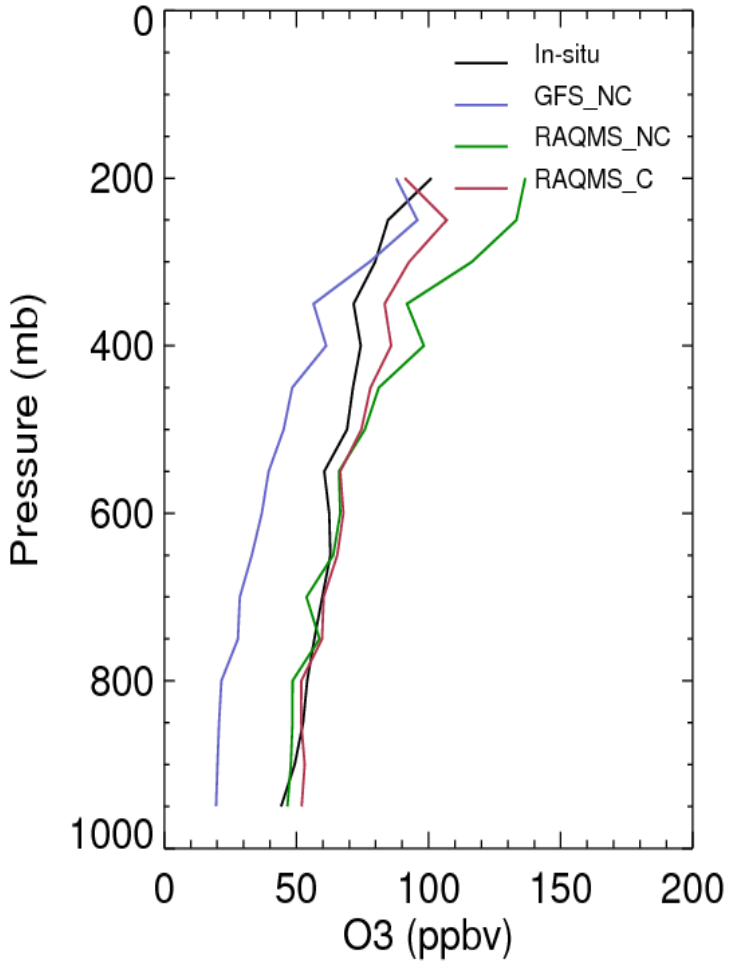

Figure 3.8: Comparison between different model modification O_3 fields and aircraft measurements. The aircraft measurements were acquired on 14 DC-8 flights between 10 July 2004 and 15 August 2004. Plotted are the median profiles of: the in situ aircraft data in black ("In-situ"), the analysis results using operational NCEP GFS O_3 production-loss parameterization and no O_3 convective mixing in blue ("GFS_NC"), the analysis results using RAQMS O_3 production-loss parameterization and no O_3 convective mixing in the model in green ("RAQMS_NC"), and the analysis results using RAQMS O_3 production-loss parameterization and O_3 convective mixing in the model in red ("RAQMS_C"). All analysis results assimilated only conventional meteorological observations.

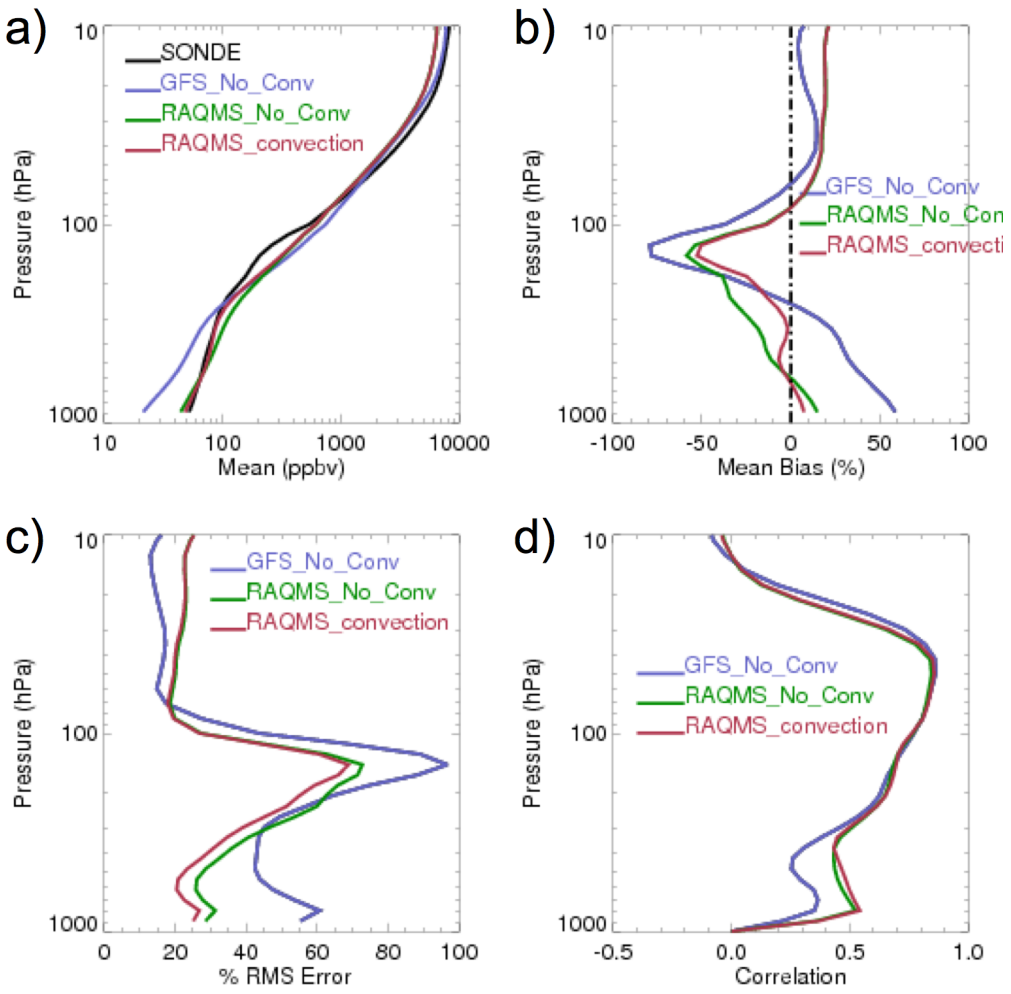

Figure 3.9: Comparison between different model modification O_3 fields and ozonesonde measurements. Ozonesonde measurements, "SONDE" (black in panel (a)), were acquired from 217 launched sondes between 10 July 2004 and 15 August 2004. In all panels, "GFS_No_Conv" (blue) is analysis results using 2004 operational NCEP GFS O_3 production-loss parameterization and no convective mixing of ozone, "RAQMS_No_Conv" (green) is analysis results using RAQMS O_3 production-loss parameterization and no convective mixing of O_3 in the model and "RAQMS_Convection" (red) is analysis results using RAQMS O_3 production-loss parameterization and convective mixing of O_3 in the model. All analysis results are with only conventional meteorological observations assimilated. Panel (a) shows the time averaged mean vertical profiles (in ppb volume mixing ratio), panel (b) the mean bias (in percent), panel (c) the RMS error (in percent), and panel (d) the correlation between the model results and the ozonesondes.

the meteorological fields. To further investigate this possibility, in Figure 3.10, we look at both the impact from using RAQMS O_3 production-loss values (panels (a) and (b)) and from incorporating convective mixing of O_3 (panels (c) and (d)) on the analysis of the geopotential height meteorological field. As shown in the figure, the convective mixing of O_3 has nearly no impact on the geopotential height field (panels (c) and (d)). This is not unexpected, because O_3 has a large impact on the radiative processes only in the stratosphere. In addition, the RAQMS O_3 production-loss values did have a negative impact on the meteorological fields (see panels (a) and (b)). This can be explained by the bias seen in the stratospheric O_3 from the RAQMS production-loss values in Figure 3.9. This bias (discussed in section 2.1.3) affects the geopotential height fields through the temperature fields, which are affected by the modified radiative heating due to change in the O_3 concentration. The response of the temperature field to the modified O_3 modeling is similar to that of the geopotential height (results not shown here). The 2004 operational NCEP GFS O_3 production-loss parameterization has been tuned to maintain the O_3 field in the stratosphere, which may explain why it performs better for this region than in the troposphere, as seen in Figure 3.9.

The experiments described above show that, in the troposphere, using RAQMS-based production-loss values and a simplified Arakawa and Schubert cumulus parameterization to account for the convective mixing of O_3 improves modeling of the O_3 in the NCEP GFS compared to its original configuration. In the stratosphere, however, the RAQMS O_3 production-loss parameterization is inferior to the original parameterization of the operational NCEP GFS, which leads to a negative impact

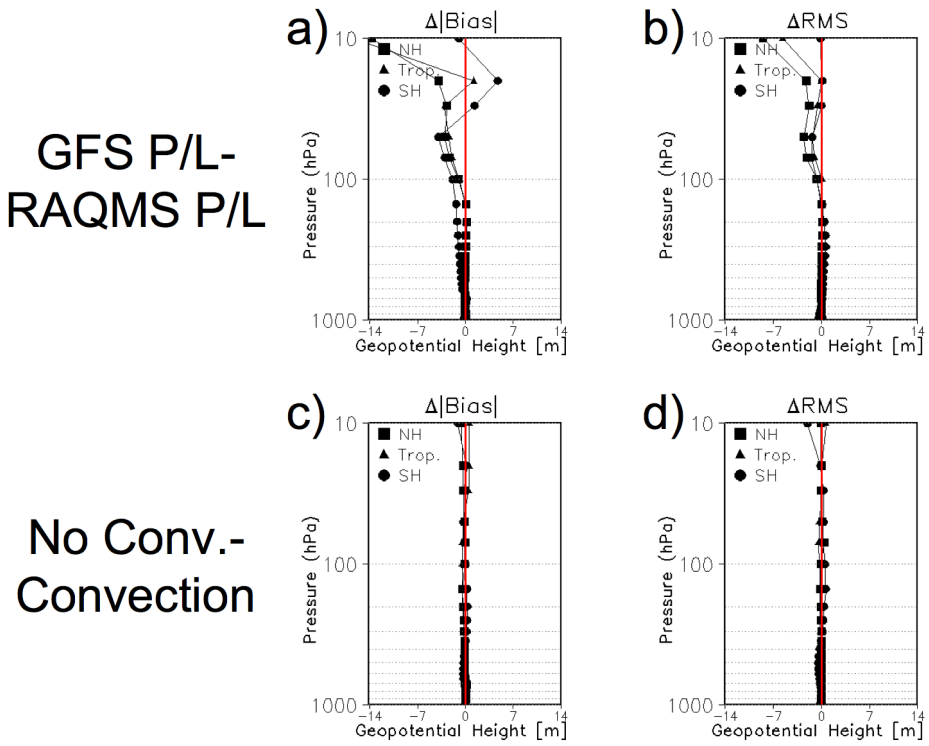

Figure 3.10: Comparison between different model modification geopotential height fields relative to the high resolution operational NCEP GFS analysis. Panels (a) and (b) show the difference between 2004 operational NCEP GFS O_3 production-loss parameterization and RAQMS O_3 production-loss parameterization. Panels (c) and (d) show the difference between no convective mixing of O_3 in the model and convective mixing of O_3 in the model. Panels (a) and (c) show the difference in the absolute value of the bias calculated relative to the high resolution operational NCEP GFS analysis. Panels (b) and (d) show the difference in the RMS error calculated relative to the high resolution operational NCEP GFS analysis. The statistics are averaged over 45 days from 000UTC 10 July 2004 to 000UTC 15 August 2004 in three different regions: northern hemisphere "NH" (square) from 30N to 90N, tropics "Trop" (triangle) from 30S to 30N and southern hemisphere "SH" (circle).

on the meteorological fields through the stratospheric radiative processes.

3.3 Assimilation of O_3 Observations

To evaluate the impact of the multivariate SBUV/2 O_3 retrieval assimilation we carry out two experiments: in the first experiment we assimilate only the meteorological observations (benchmark no-ozone experiment), and in the second experiment we assimilate both the meteorological observations and SBUV/2 O_3 retrieval observations (ozone experiment). Both experiments use the version of the NCEP GFS that includes our modifications to the O_3 modeling and the LETKF assimilation system.

We use three different approaches to compare the analysis and forecast errors for the meteorological fields of the experiments. First, error statistics are computed by comparing the no-ozone and O_3 experiments to the high resolution operational NCEP analyses. Our no-ozone experiment differs from the NCEP analyses in two respects: (1) the modeling of ozone is different, and (2) we do not assimilate satellite radiances and SBUV/2 O_3 retrieval observations in our system. On the other hand, our O_3 experiment differs from the NCEP analysis by the modeling of O_3 and, even though we assimilate SBUV/2 O_3 retrievals, we assimilate the O_3 observations multivariately, whereas NCEP assimilated these observations univariately.

The second approach to verify of the meteorological fields is to compare 48-h forecasts started from the analyses we produce to the verifying NCEP analyses. It should be noted that the O_3 production-loss parameters used in the forecast are from

the RAQMS analysis results. In this sense, the final product is not a true forecast that could be produced in real time. Instead, the forecast results are a demonstration of potential forecast skill assuming that we have a good representation of the production-loss parameters for the trace gases.

Our third approach for the meteorological field verification is based on comparing 48-hour forecasts to radiosonde observations. More precisely, the root-mean-square error is estimated by comparing radiosonde observations with the forecast field interpolated to the observational locations. The average is calculated over observational locations instead of model grid points. While this approach has the advantage that the verified and the verification data sets are truly independent, thus providing a neutral verification approach for the comparison of the two systems, it has the significant disadvantage that the radiosonde network is strongly inhomogeneous, and the verification results reflect forecast accuracy over highly populated areas of the globe (see Figure 3.4).

We use two approaches for the verification of the O_3 fields. The first approach compares the analysis and short-term forecasts to the O_3 measurements obtained in the 14 INTEX-A DC-8 aircraft flights between 11 July 2004 and 15 August 2004. The second approach compares the analysis and short-term forecasts to the O_3 measurements obtained in the IONS ozonesonde project launched from 12 different locations. For both of these approaches we compare the analysis and/or forecast states to the verification sets at the observational locations. Similar to the verification against radiosonde observations, this approach provides a verification with a truly independent verification data. On the other hand, they provide verification

data only over the continental united states and Canada (see Figure 3.6 and Figure 3.7)

3.3.1 O_3 Assimilation Impact on Meteorological Fields

First, the no-ozone and O_3 experiments are compared to the high resolution operational NCEP analyses (see Figure 3.11). In Figure 3.11 we show the impact on the meteorological fields from the multivariate assimilation of SBUV/2 O_3 retrieval observations. Shown in the figure is the difference between a 45 day assimilation without O_3 observations and an assimilation including O_3 observations. Two statistics are shown: the absolute value of the bias and the RMS error, both calculated relative to the high resolution operational NCEP GFS analysis. Each of these statistics are averaged in one of three regions of the globe: northern hemisphere (30N to 90N), tropics (30S to 30N) and southern hemisphere (90S to 30S). In the figure a negative value implies that the assimilation of SBUV/2 O_3 retrieval observations has a negative impact on the field and a positive value implies that the assimilation of O_3 observations has a positive impact on the field.

It is clear from Figure 3.11 that the assimilation of O_3 observations has significant negative impact on the meteorological fields. There are some areas of positive impact in the troposphere but these are dwarfed by the negative impacts seen in the stratosphere.

Next, we compare the 48-hour forecasts from the experimental analyses to the high-resolution NCEP GFS analyses (Figure 3.12). It is clear from Figure 3.12 that

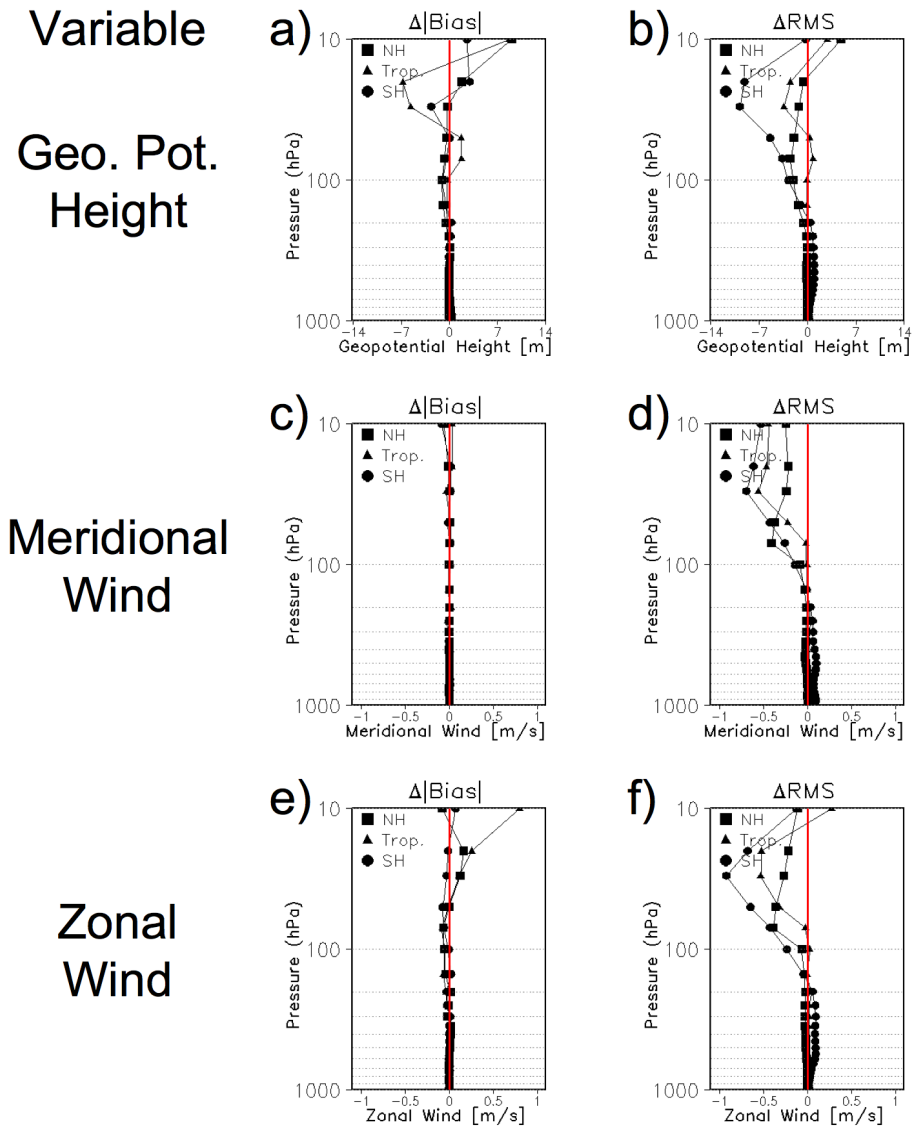

Figure 3.11: SBUV/2 O_3 retrieval observation assimilation impact on the meteorological fields verified with NCEP GFS analysis. All panels show the difference between assimilation with only conventional meteorological observations and assimilation with conventional meteorological observations as well as O_3 observations. Panels (a) and (b) show the geopotential height field, panels (c) and (d) show the meridional wind field and panels (e) and (f) show the zonal wind field. Panels (a), (c), and (e) show the difference in the absolute value of the bias calculated relative to the high resolution operational NCEP GFS analysis. Panels (b), (d), and (f) show the difference in the RMS error calculated relative to the high resolution operational NCEP GFS analysis. The statistics are averaged over 45 days from 000UTC 10 July 2004 to 000UTC 15 August 2004 in three different regions: Northern Hemisphere "NH" (square) from 30N to 90N, Tropics "Trop" (triangle) from 30S to 30N and Southern Hemisphere "SH" (circle) from 90S to 30N.

there is some negative impact from the assimilation of O_3 observations on the 48-hour forecast of the meteorological fields, but these degradations have significantly reduced amplitude compared to the magnitude of the degradations in the analysis. Also, the negative bias seen in the tropics of the geopotential height field in Figure 3.11 vanishes by the 48-hour forecast time.

Our final verification results are from the comparison of the 48-hour forecasts to the radiosonde observations (see Figure 3.13). It is not clear, according to this verification approach, that the O_3 assimilation has a negative impact on the meteorological fields.

3.3.2 O_3 Meteorological Field Impact Investigation

As described in the previous section, the multivariate assimilation of the O_3 observations has a negative effect on the analysis of the meteorological fields. There are three potential causes of this negative impact: O_3 observation bias, deficiencies in the O_3 model and/or deficiency in the O_3 observational error. In what follows we address each of these areas.

3.3.2.1 O_3 Observation Bias

Nazaryan et al. (2007) reported a bias of less than 9% in the layers from 40 to 1.5 hPa for the NOAA-11 and NOAA-16 SBUV/2 version 8 data sets. Nazaryan et al. (2007) compared coincident measurements to the HALOE version 19 vertical profiles between the years of 1991 to 2005. The results agreed with previous studies

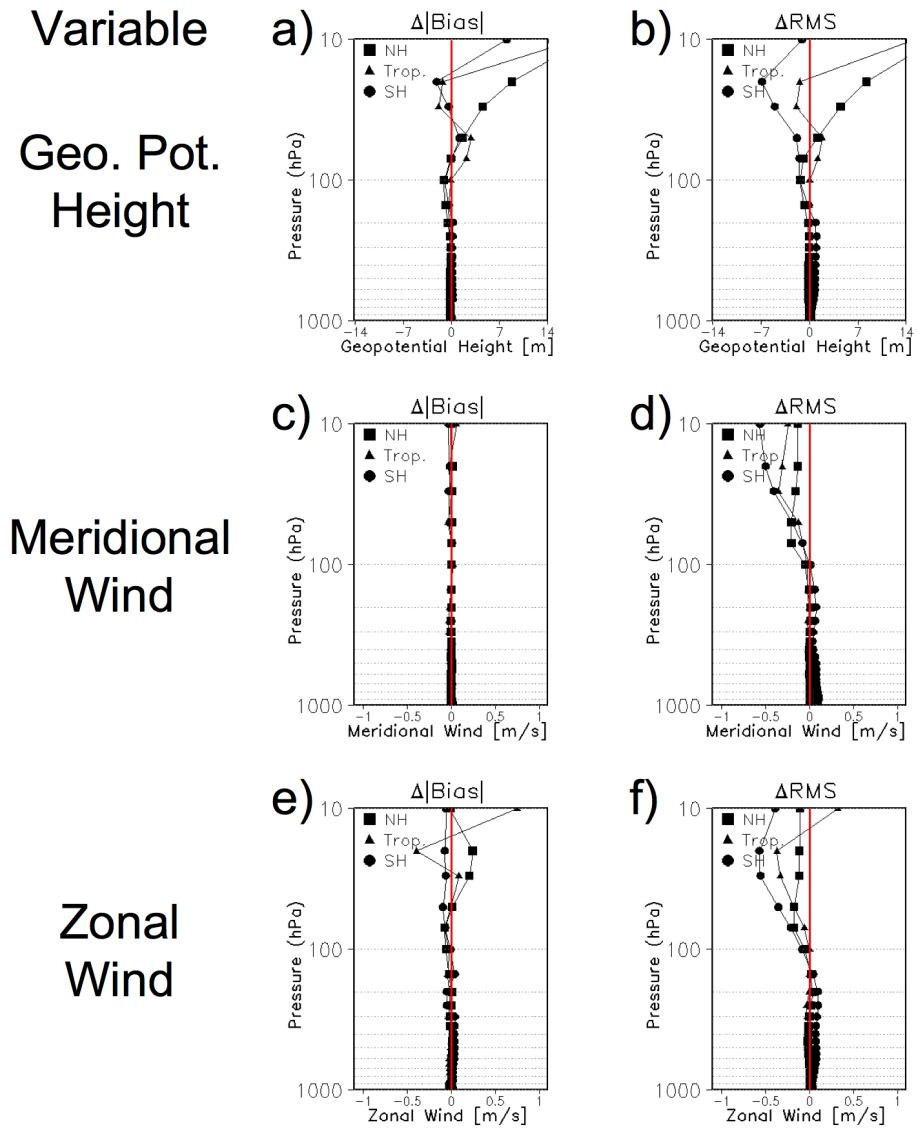

Figure 3.12: 48-hour forecast SBUV/2 O_3 retrieval observation assimilation impact on the meteorological fields verified with NCEP GFS analysis. All panels show the difference between assimilation with only conventional meteorological observations and assimilation with conventional meteorological observations as well as O_3 observations. Panels (a) and (b) show the geopotential height field, panels (c) and (d) show the meridional wind field and panels (e) and (f) show the zonal wind field. Panels (a), (c), and (e) show the difference in the absolute value of the bias calculated relative to the high resolution operational NCEP GFS analysis. Panels (b), (d), and (f) show the difference in the RMS error calculated relative to the high resolution operational NCEP GFS analysis. The statistics are averaged over 45 days from 000UTC 10 July 2004 to 000UTC 15 August 2004 in three different regions: northern hemisphere "NH" (square) from 30N to 90N, tropics "Trop" (triangle) from 30S to 30N and southern hemisphere "SH" (circle) from 90S to 30N.

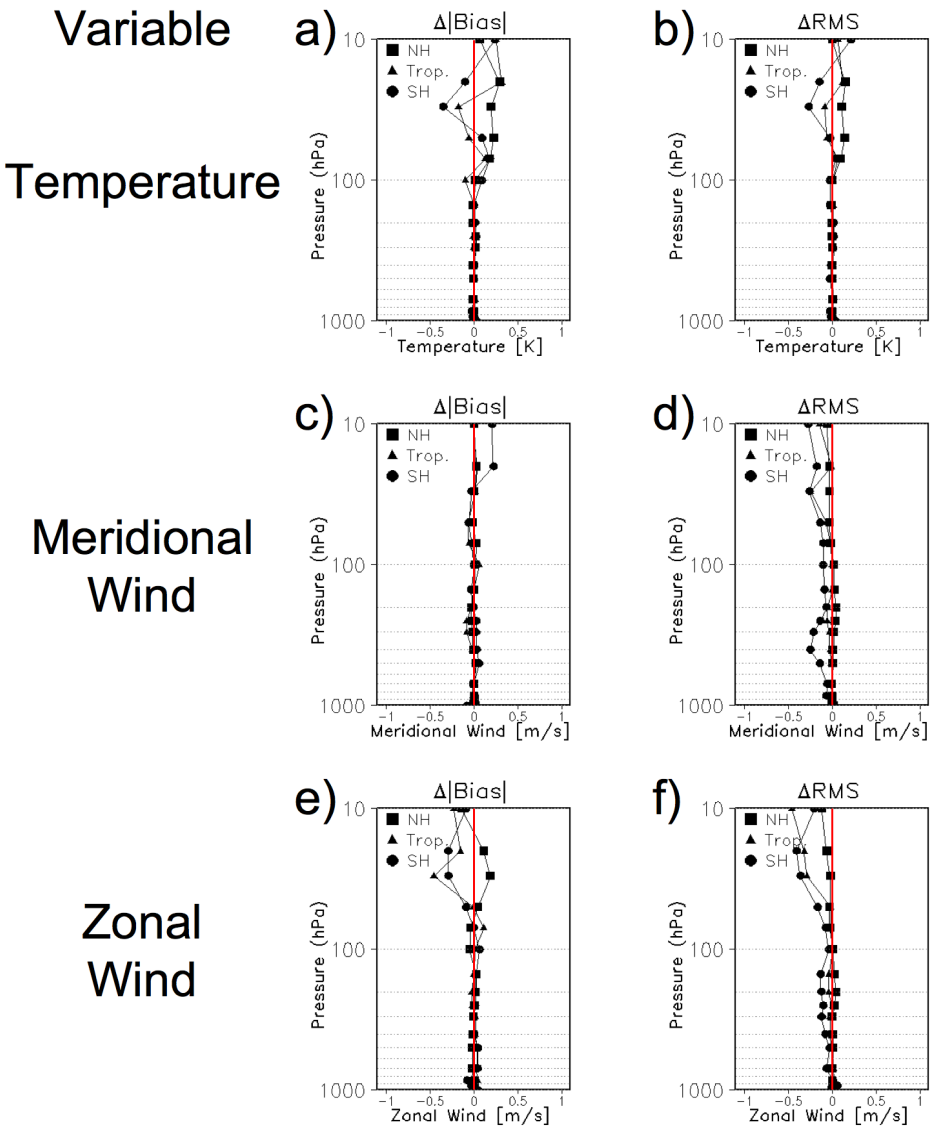

Figure 3.13: 48-hour forecast SBUV/2 O_3 retrieval observation assimilation impact on the meteorological fields verified with radiosonde observations. All panels show the difference between assimilation with only conventional meteorological observations and assimilation with conventional meteorological observations as well as O_3 observations. Panels (a) and (b) show the temperature field, panels (c) and (d) show the meridional wind field and panels (e) and (f) show the zonal wind field. Panels (a), (c), and (e) show the difference in the absolute value of the bias calculated relative to the radiosonde observations. Panels (b), (d), and (f) show the difference in the RMS error calculated relative to the radiosonde observations. The statistics are averaged over 45 days from 000UTC 10 July 2004 to 000UTC 15 August 2004 in three different regions: northern hemisphere "NH" (square) from 30N to 90N, tropics "Trop" (triangle) from 30S to 30N and southern hemisphere "SH" (circle) from 90S to 30N.

comparing SBUV/2 version 8 retrieval observations to ECC ozonesondes, LIDAR and microwave retrievals, SAGE II and HALOE O_3 data sets (McPeters et al., 2004) as well as Umkehr measurements from ground-based systems (Petropavlovskikh et al., 2005). This reported bias should be compared with the 5-10% standard deviation observation error range reported for the SBUV/2 retrievals and used in the assimilation. The bias is on the same order of magnitude as the standard deviation and thus not negligible.

3.3.2.2 O_3 Model Error

As discussed in section 3.2, the modeling of O_3 in the RAQMS model of O_3 is known to be deficient in the stratosphere. This stratospheric low bias in the model can potentially cause the negative response in the meteorological fields to the assimilation of SBUV/2 O_3 retrievals. However, the operational NCEP GFS O_3 production-loss model does not have this issue in the stratosphere, and the results from the assimilation of SBUV/2 O_3 observations using the original production-loss values from the NCEP GFS produces similar negative results. In Figure 3.14 we show the verification results for this experiment, which have a worse fit than those shown in Figure 3.11 for the experiment with RAQMS production-loss values.

Also, it is known that the sub-grid scale process parameterizations, such as convective mixing, are deficient in modeling sub-grid scale transport processes. As discussed in section 3.1.2, this could lead to a negative impact of O_3 assimilation on the meteorological fields.

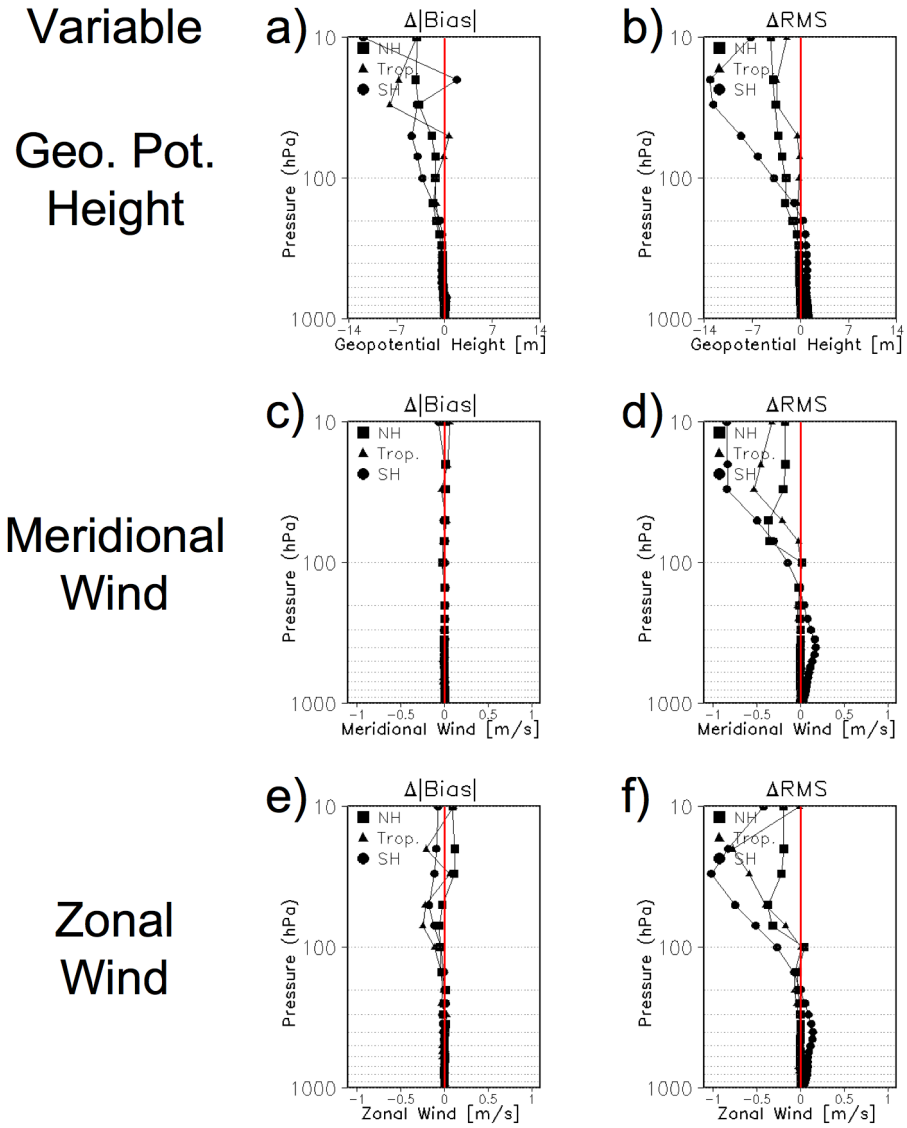

Figure 3.14: SBUV/2 O_3 retrieval observation assimilation impact on the meteorological fields verified with NCEP GFS analysis. Same as Figure 3.11, except here the operational NCEP GFS O_3 production-loss model is used.

3.3.2.3 O_3 Observation Error

We know that the observational error specification in the analysis is deficient in that the covariance between the O_3 observations is not considered, though the errors of the retrieval observations are known to be strongly correlated. To account for these strong correlations we increase the value of the prescribed O_3 observational error variance, a process which we will call O_3 observation error inflation. While not a perfect solution, accounting for the effect of neglected covariance by increasing the variance of the observation errors is a standard practice in NWP. In essence, by inflating the observation error variance, we give less weight to the observations in the analysis than if they were independent measurements of the state of the atmosphere.

To investigate the origin of the negative impact of O_3 assimilation on the meteorological fields, we carry out a series of experiments inflating the prescribed variance of the observation error of the O_3 by different amounts. In these experiments, the O_3 standard deviation error is multiplied by a gradually increasing factor (2, 4 and 10). This increases the observation error variance (square of the standard deviation) by a factor of 4, 16 and 100.

Shown in Figure 3.15 is the zonal wind field verification at the analysis time against the operational NCEP GFS analysis; in Figure 3.16 is the zonal wind field verification at the 48-hour forecast time against the NCEP GFS analysis; and in Figure 3.17 is the zonal wind field verification at the 48-hour forecast time against the radiosonde observations. All figures show results for an increasing observation error inflation factors going from the top to the bottom.

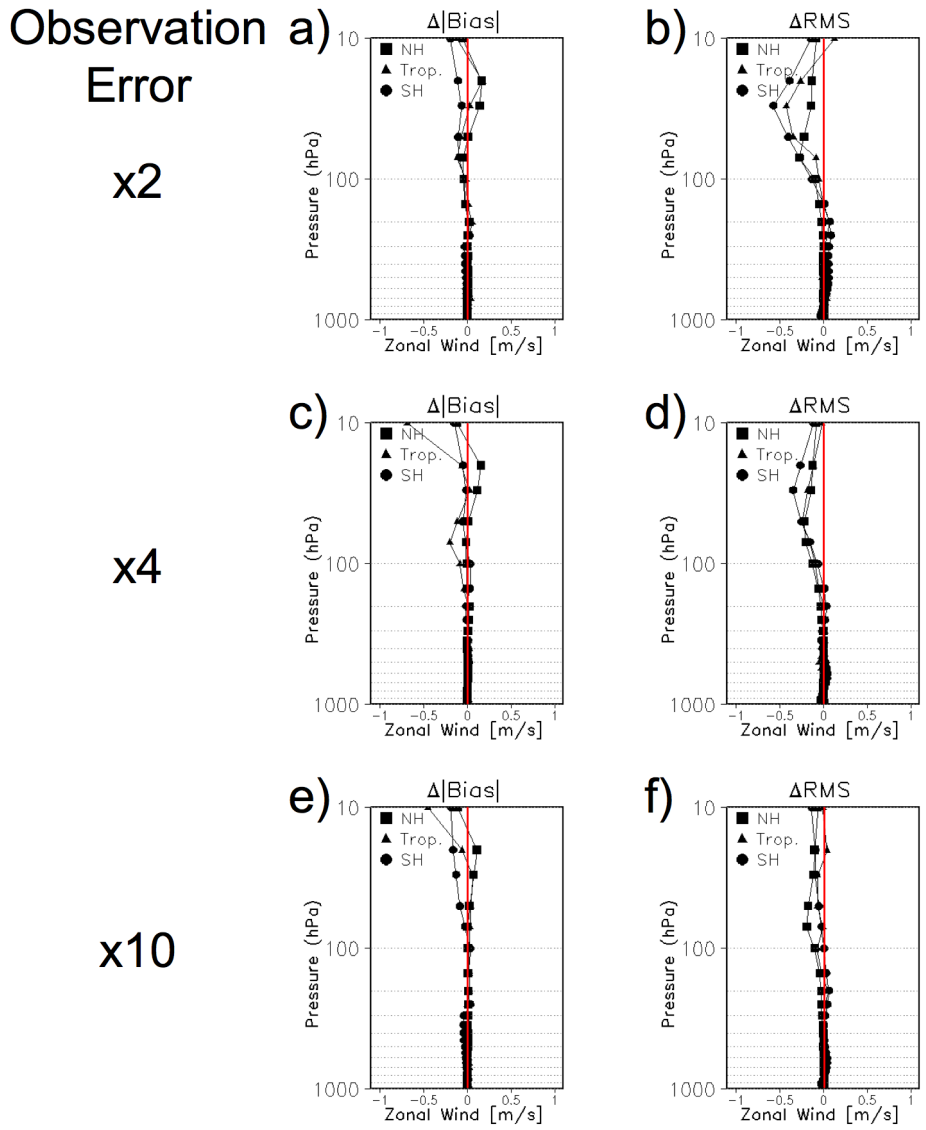

Figure 3.15: Ozone observation error inflation impact on the zonal wind field verified with NCEP GFS analysis. Same as Figure 3.11, except all panels show geopotential height field and panels (a) and (b) show the impact of 2 O_3 observation error inflation factor, panels (c) and (d) show the impact of 4 O_3 observation error inflation factor and panels (e) and (f) show the impact of 10 O_3 observation error inflation factor.

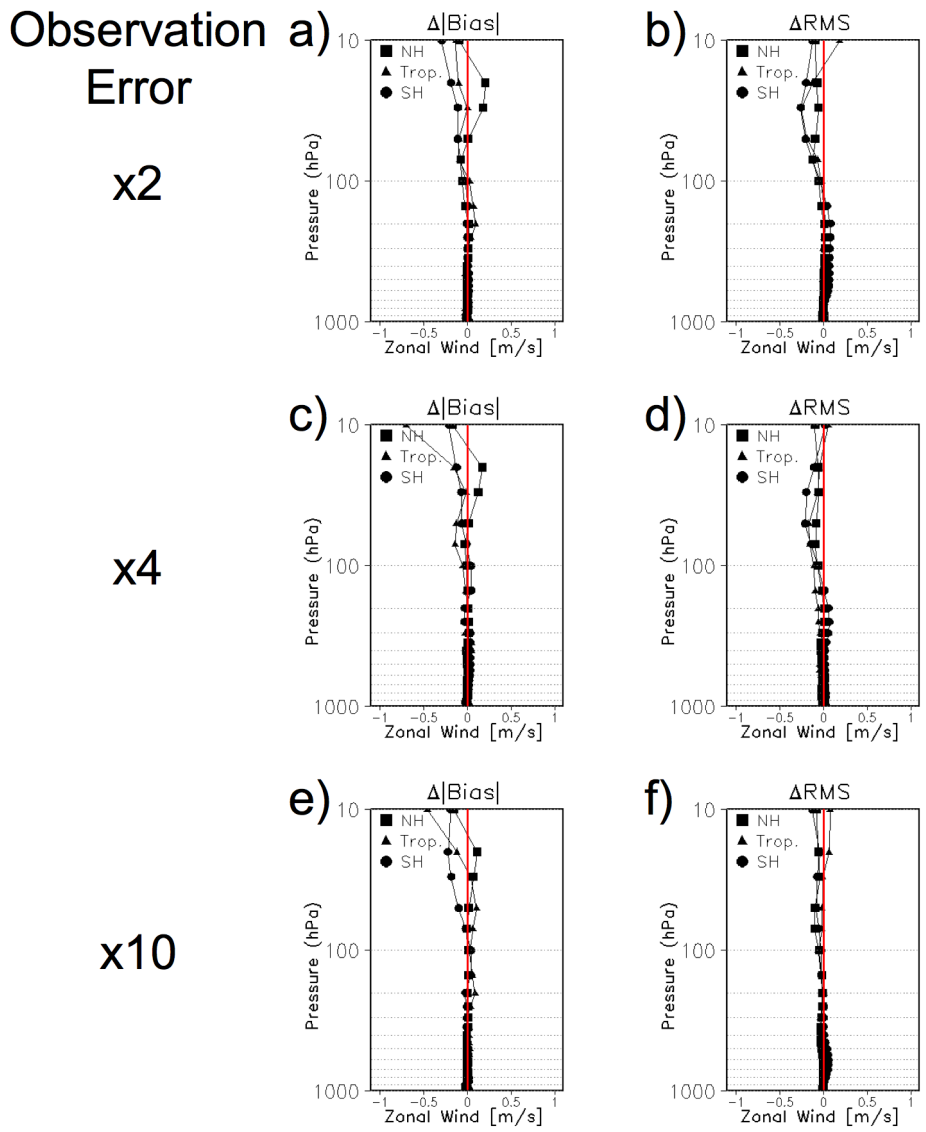

Figure 3.16: Ozone observation error inflation impact on the zonal wind field 48-hour forecast from the analysis and verified with the NCEP GFS analysis. Same as Figure 3.12, except all panels show geopotential height field and panels (a) and (b) show the impact of 2 O_3 observation error inflation factor, panels (c) and (d) show the impact of 4 O_3 observation error inflation factor and panels (e) and (f) show the impact of 10 O_3 observation error inflation factor.

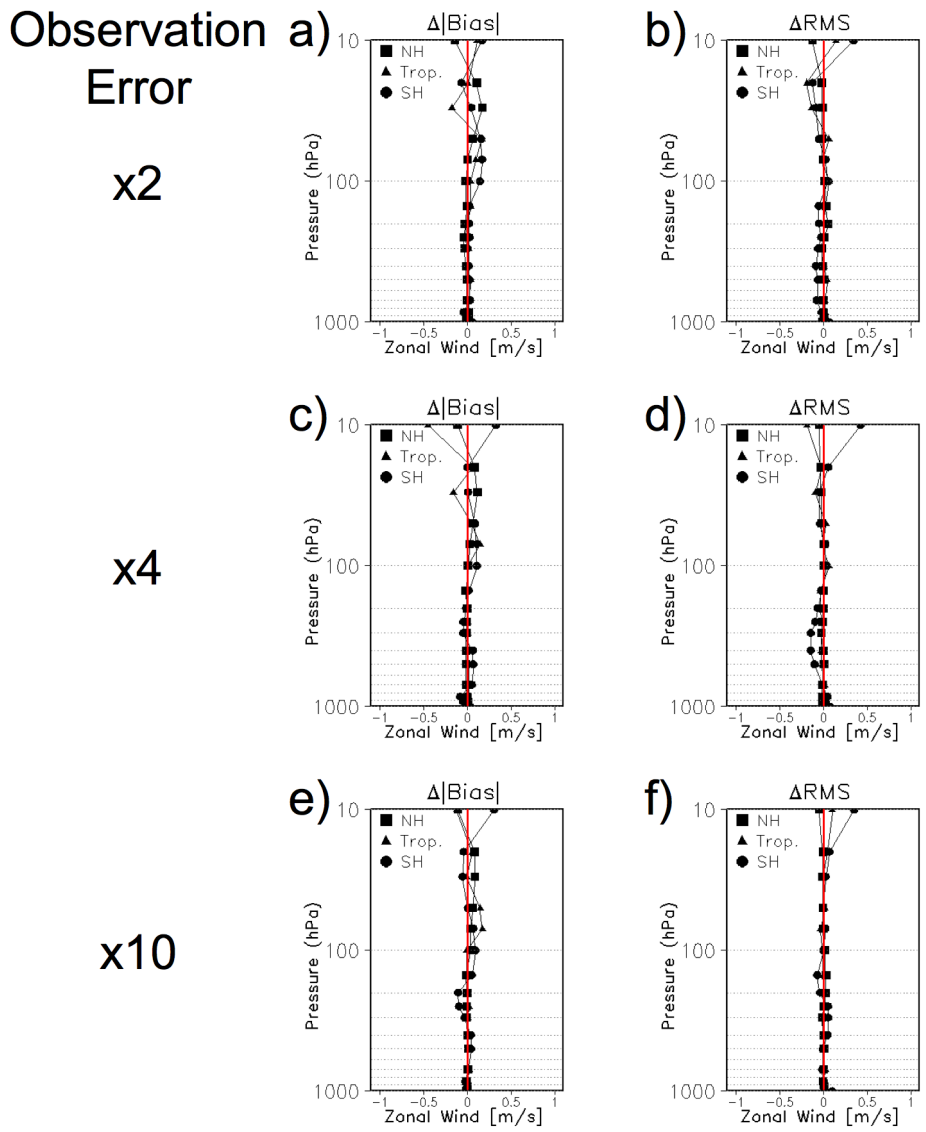

Figure 3.17: Ozone observation error inflation impact on the zonal wind field 48-hour forecast from the analysis and verified with the radiosonde observations. Same as Figure 3.13, except all panels show geopotential height field and panels (a) and (b) show the impact of 2 O_3 observation error inflation factor, panels (c) and (d) show the impact of 4 O_3 observation error inflation factor and panels (e) and (f) show the impact of 0 O_3 observation error inflation factor.

Based on Figure 3.15, the conclusion would be to use an observation error inflation factor between 4 and 10; however, taken together with the other two verification figures, one would favor a factor between 2 and 4.

The single meteorological variable for which we see a clear positive impact from the assimilation of O_3 observations is the geopotential height field: shown in Figure 3.18 is the 48-hour forecast verification against the NCEP GFS analysis for the 2 and 4 observation error inflation factors. For both the bias error and the rms error we see a clear positive impact in the stratospheric geopotential height field.

We do not see such a dramatic positive impact on the temperature field in the 48-hour forecast verification against the radiosondes as we saw for the geopotential height field. Nevertheless, the over all impact on the temperature forecasts is positive (Figure 3.19). The bias reduction for the experiment in which the O_3 observation error standard deviation is inflated by a factor of 2 is nearly 0.5 K in the Northern and the Southern Hemispheres.

3.3.3 O_3 Assimilation Impact on Ozone Fields

In Figure 3.20, we compare the O_3 analysis for the different error inflation factors with the ozonesonde data. It is clear that the assimilation of SBUV/2 O_3 retrieval observations reduces the bias and rms error in the stratosphere. This is exactly what occurred with the RAQMS analysis when SAGE III and TOMS observations were assimilated (Pierce et al., 2007). In Figure 3.20, it can also be seen that there is a weak impact of observation error inflation factors on the O_3

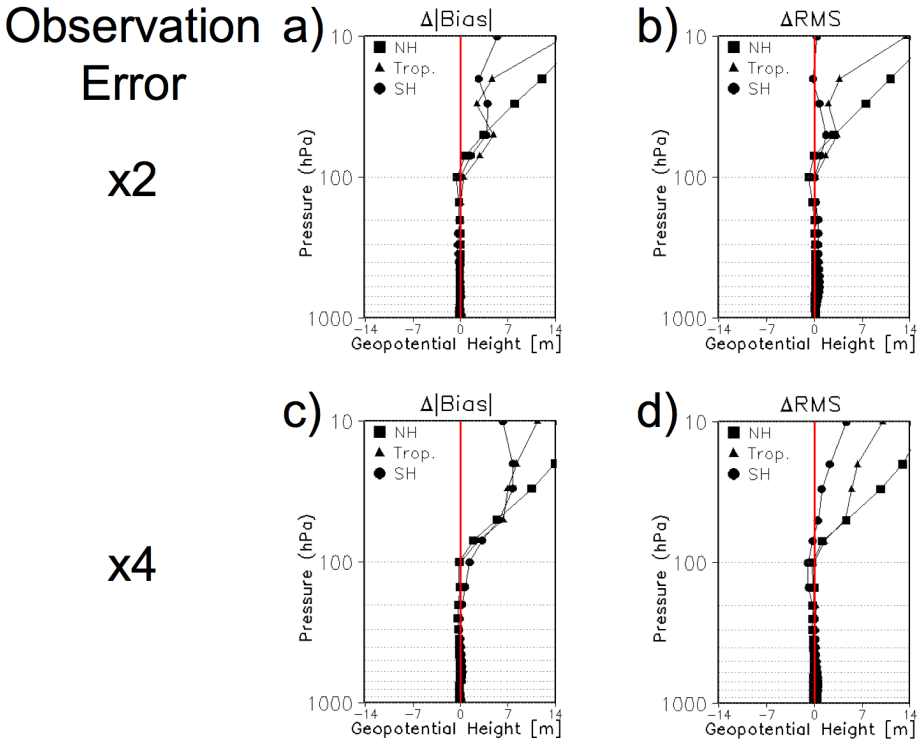

Figure 3.18: Ozone observation error inflation impact on the geopotential height field 48-hour forecast from the analysis and verified with the NCEP GFS analysis. Same as Figure 3.16, except all panels show geopotential height field and panels (a) and (b) show the impact of 2 O_3 observation error inflation factor and panels (c) and (d) show the impact of 4 O_3 observation error inflation factor.

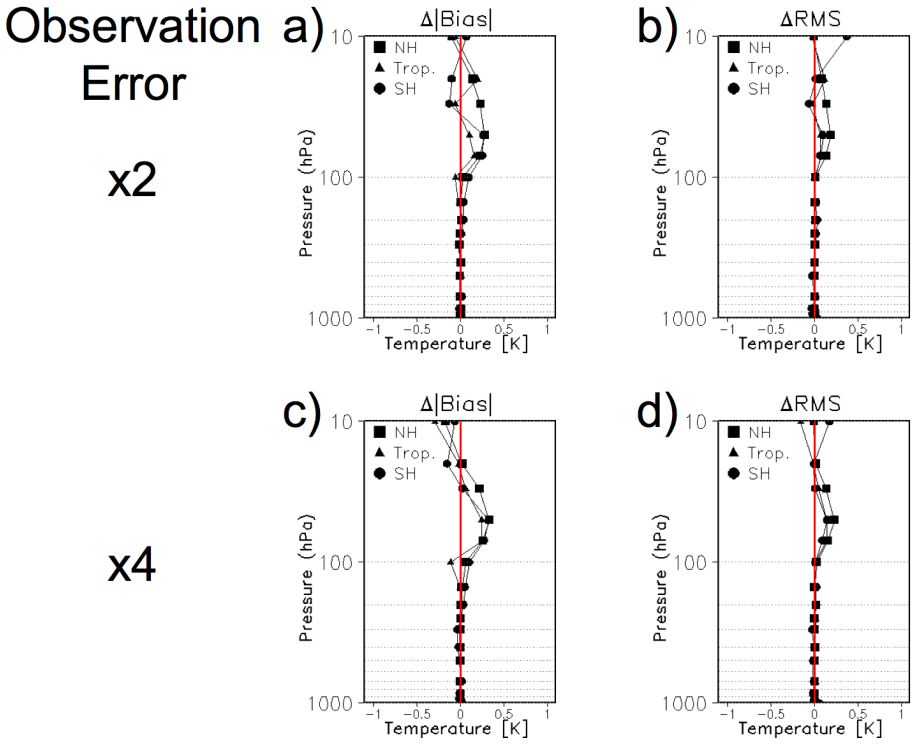

Figure 3.19: Ozone observation error inflation impact on the temperature field 48-hour forecast from the analysis and verified with the NCEP GFS analysis. Same as Figure 3.17, except all panels show temperature field and panels (a) and (b) show the impact of 2 O_3 observation error inflation factor and panels (c) and (d) show the impact of 4 O_3 observation error inflation factor.

field. The analogous figure for the 48-hour forecasts is very similar to Figure 3.20, therefore, it is not shown.

In Figure 3.21 we see the effect of increasing the observation error on the verification results with in-situ aircraft data. As the inflation factor is increased, the median value tends slightly towards the aircraft value, although, for the most part, increasing the inflation factor has no impact on the verification results. Comparing these results to Figure 3.8, which shows the case of no O_3 assimilation, and with Figure 3.22, which shows the verification results against the high resolution operational NCEP GFS analysis and the RAQMS analysis, we conclude that the multivariate assimilation of O_3 observations clearly improves the analysis of the tropospheric O_3 vertical profile. The figure for the verification of the 48-hour forecasts is very similar to Figure 3.21, thus it is not shown.

At the top of Figure 3.23 and Figure 3.24 we plot the time series ("curtain") of the O_3 analysis profile for the DC-8 flight on 22 July 2004 (the flight track is highlighted in red in Figure 3.6). The curtains are made by interpolating the O_3 analysis results onto the DC-8 flight track and sampling the vertical profile of the model at the frequency of the in situ measurements. At the bottom of Figure 3.23 and Figure 3.24 we compare the O_3 analysis results (dashed red line) and the in situ O_3 observations (solid black line) for the same DC-8 flight. In Figure 3.23 we show the results from the experiment with an observation error inflation factor of 2, and in Figure 3.24 we show the RAQMS analysis. Comparing the two plots it is clear that even though the median in our system is closer to the in situ measurements than the RAQMS analysis, it does not fully capture the structure of the measurement

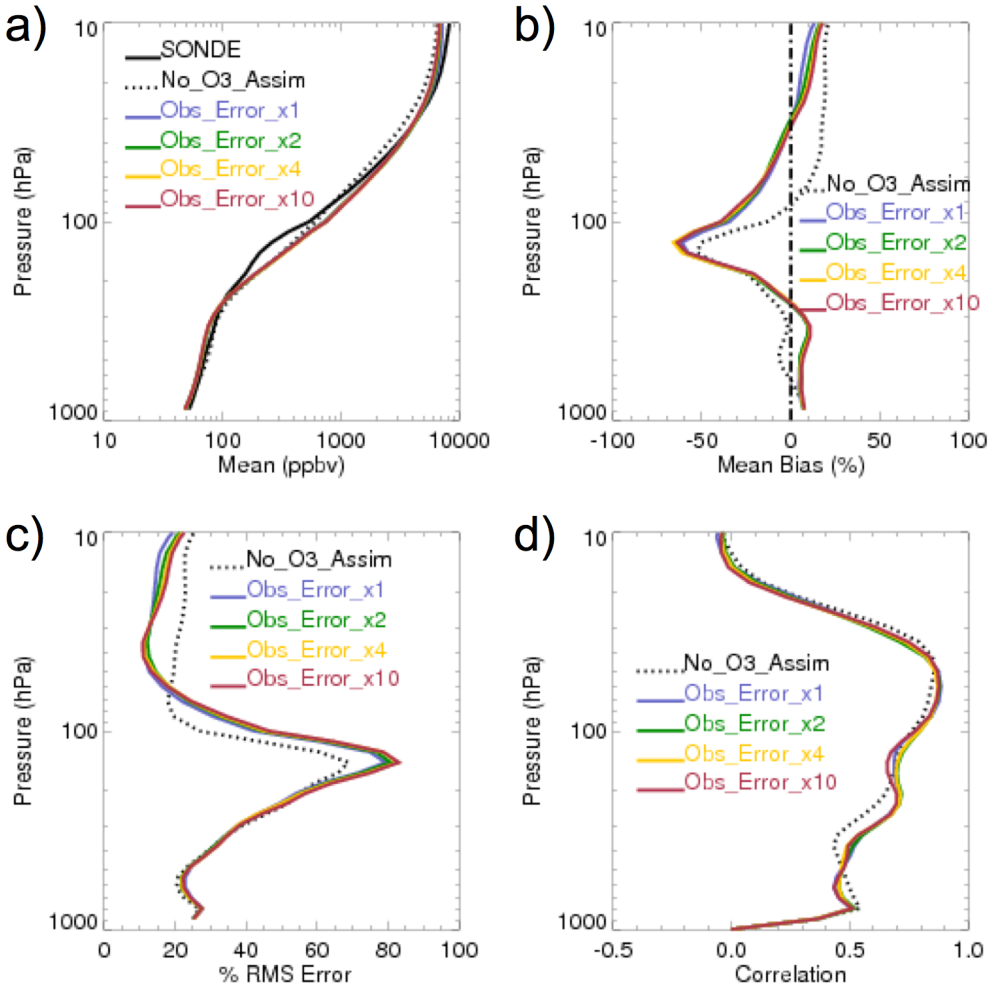

Figure 3.20: Comparison between different O_3 observation error inflation and ozonesonde measurements. Same as Figure 3.9, except all analysis results used RAQMS O_3 production-loss parameterization and convective mixing of O_3 in the model. In all panels "No_O3_Assim" is analysis results assimilating no O_3 observations, "Obs_Error_x1" (blue) is analysis results assimilating O_3 observations with no observation error inflation factor, "Obs_Error_x2" (Green) is analysis results assimilating O_3 observations with 2 observation error inflation factor, "Obs_Error_x4" (Yellow) is analysis results assimilating O_3 observations with 4 observation error inflation factor and "Obs_Error_x10" (Red) is analysis results assimilating O_3 observations with 10 observation error inflation factor.

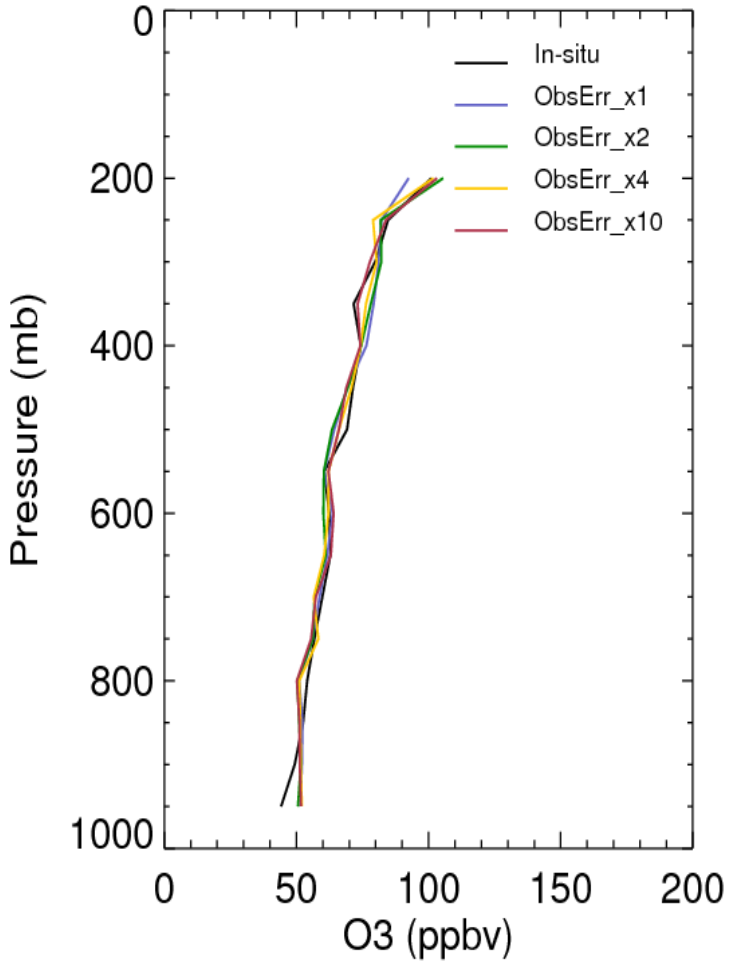

Figure 3.21: Comparison between different O_3 observation error inflation and aircraft measurements. Plotted are the median profiles of: the in situ aircraft data in black ("In-situ"), the analysis results assimilating O_3 observations with no observation error inflation factor in blue ("ObsErr_x1"), the analysis results assimilating O_3 observations with 2 observation error inflation factor in green ("ObsErr_x2"), the analysis results assimilating O_3 observations with 4 observation error inflation factor in yellow ("ObsErr_x4"), and the analysis results assimilating O_3 observations with 10 observation error inflation factor in red ("ObsErr_x10").

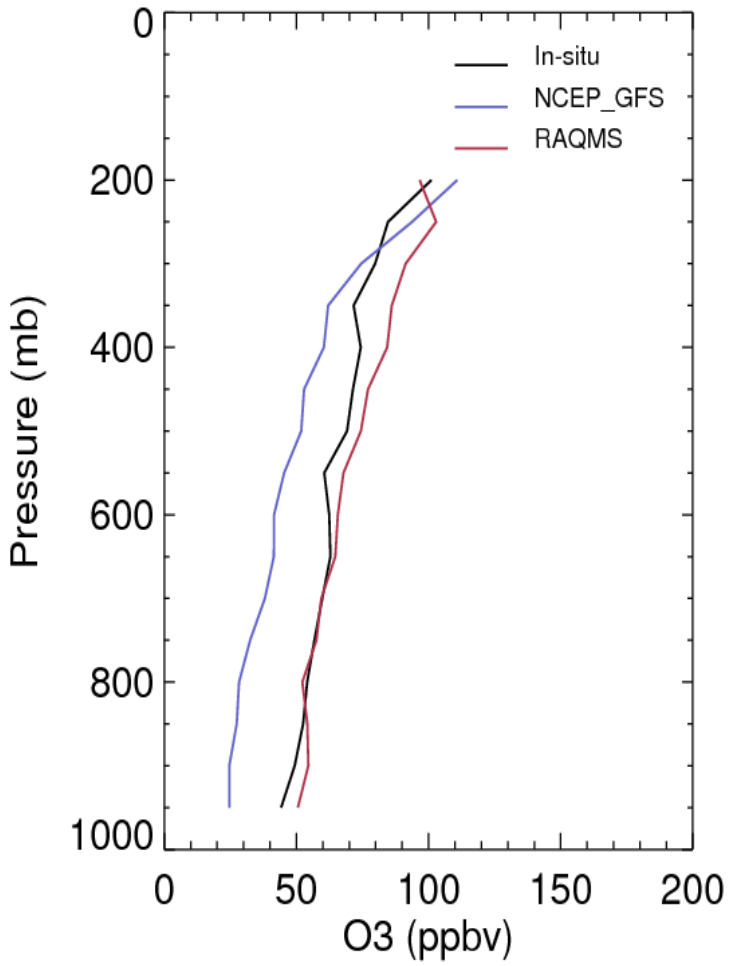

Figure 3.22: Comparison between different model analysis O_3 results and aircraft measurements. Plotted are the median profiles of: the in situ aircraft data in black ("In-situ"), the analysis results from the high resolution operational NCEP GFS analysis in blue ("NCEP_GFS"), and the analysis results from the RAMQS analysis in red ("RAQMS").

data (solid black line in the lower panel of both figures).

3.3.4 Impact of Modified Observation Operator on O_3

In Figure 3.25 and Figure 3.26 we compare the performance of the analysis system for two different choices of the observation operator: one of these observation operators, which is defined by Equation 2.15, is the one we have used in the experiments we have reported on so far; the other observation operator ignores the effects of the vertical smoothing introduced by the use of an a priori to obtain the retrieval. The latter approach is implemented by replacing the averaging kernel matrix provided with the data by the identity matrix. In Figure 3.25 we verify the analyses against the aircraft measurements and find little difference between the performance of the analysis system for the two different observation operators in the troposphere. However, Figure 3.26, which compares the analyses to the ozonesonde measurements, shows that using the information provided by the averaging kernel results in more accurate analysis near the tropopause in the rms sense.

3.3.5 Multivariate vs. Univariate Assimilation of O_3 retrievals

To assess the benefits of assimilating the O_3 retrievals multivariately, we compare the performance of the multivariate system to one in which the O_3 retrievals are assimilated univariately. The results of this comparison are shown in Figure 3.27 and Figure 3.28. In the state update step of the univariate assimilation system the assimilation of the meteorological observations affects only the meteorological fields

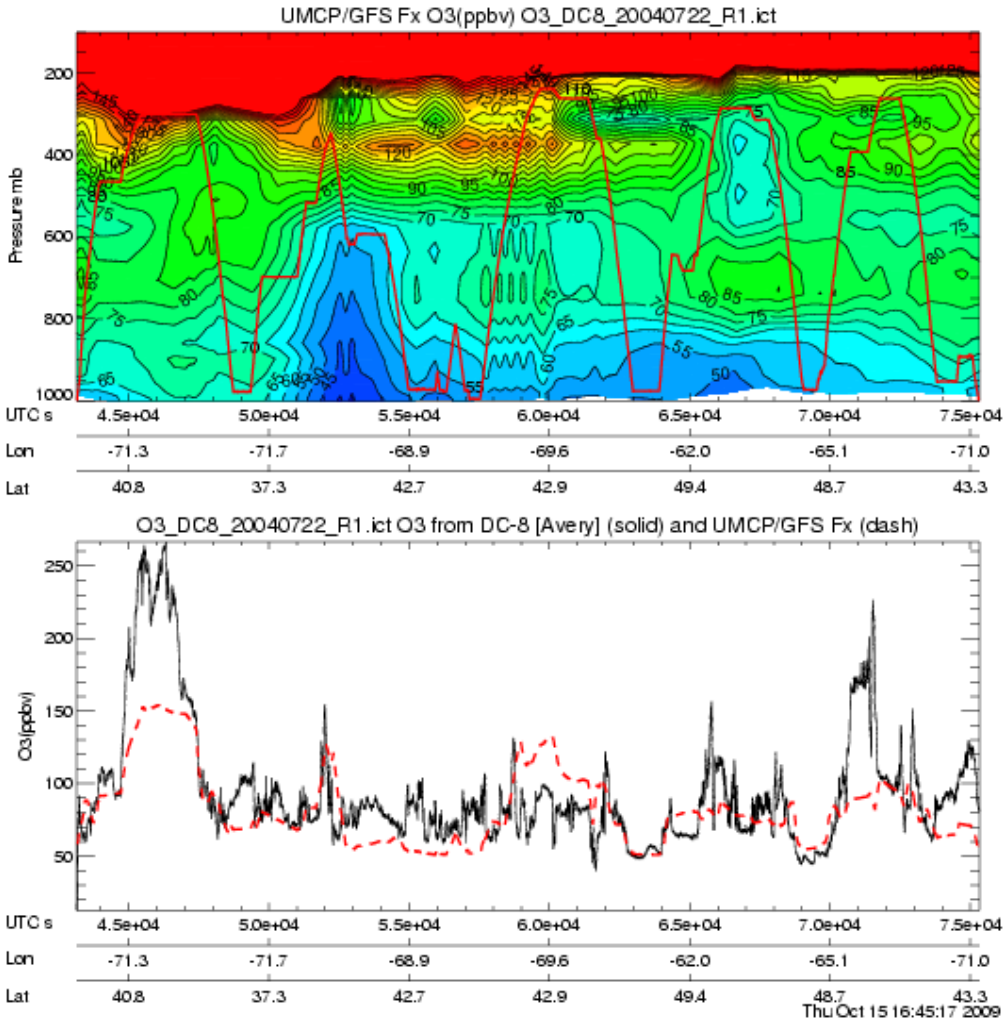

Figure 3.23: Time series of the O_3 analyses with an observation error inflation factor of 2 and the aircraft measurements. Plotted in the top panel is the time series ("curtain") of model analysis profiles for the DC-8 flight on 22 July 2004. The flight track is shown as the red line and the contours are the model analysis O_3 in volume mixing ratio (ppb). Plotted in the bottom portion of the figure is the time series comparison between the 2 observation error inflation factor model O_3 analysis results (dashed red line) and the in situ O_3 observations (solid black line) for the same DC-8 flight. The time, longitude and latitude are included on the plots.

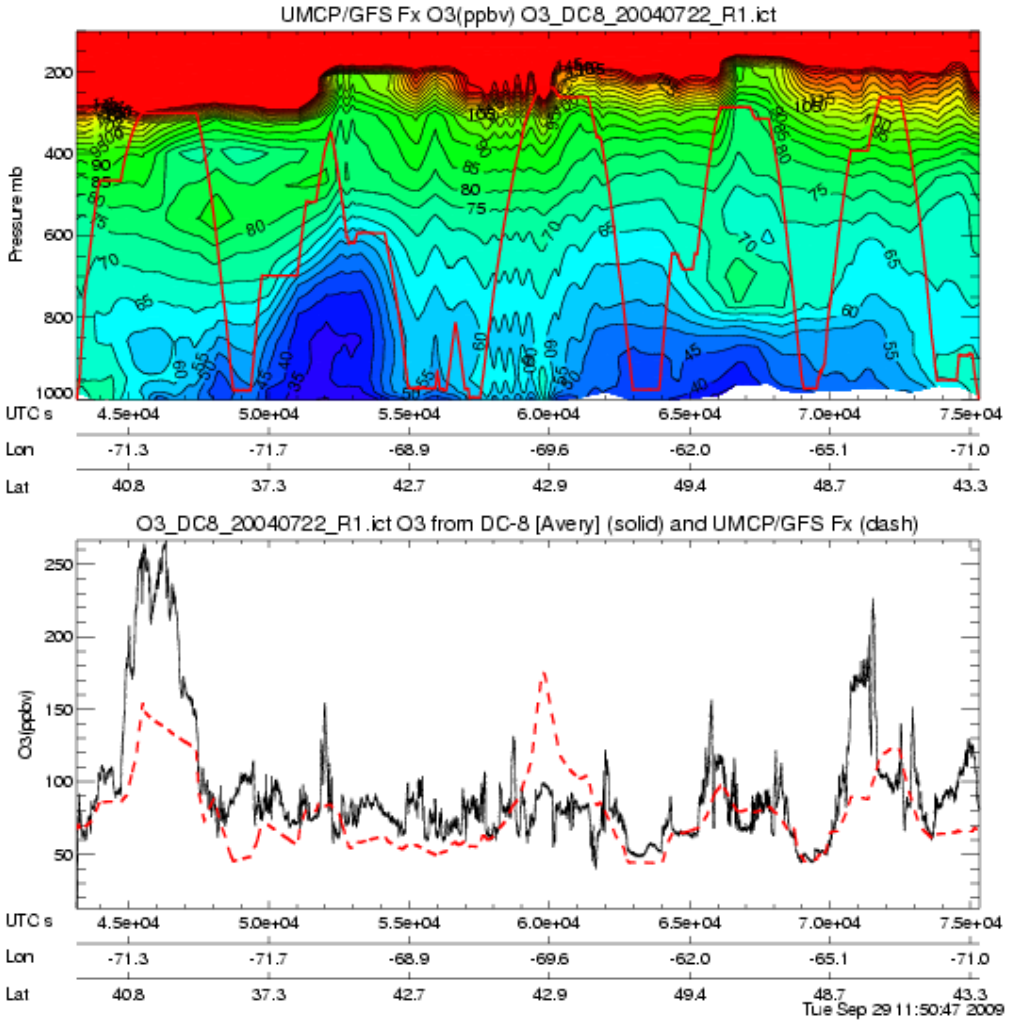

Figure 3.24: Time series of the RAQMS O_3 analyses and the aircraft measurements. Plotted in the top panel is the time series ("curtain") of the RAQMS analysis profiles for the DC-8 flight on 22 July 2004. The flight track is shown as the red line and the contours are the model analysis O_3 in volume mixing ratio (ppb). Plotted in the bottom portion of the figure is the time series comparison between the RAQMS O_3 analysis results (dashed red line) and the in situ O_3 observations (solid black line) for the same DC-8 flight. The time, longitude and latitude are included on the plots.

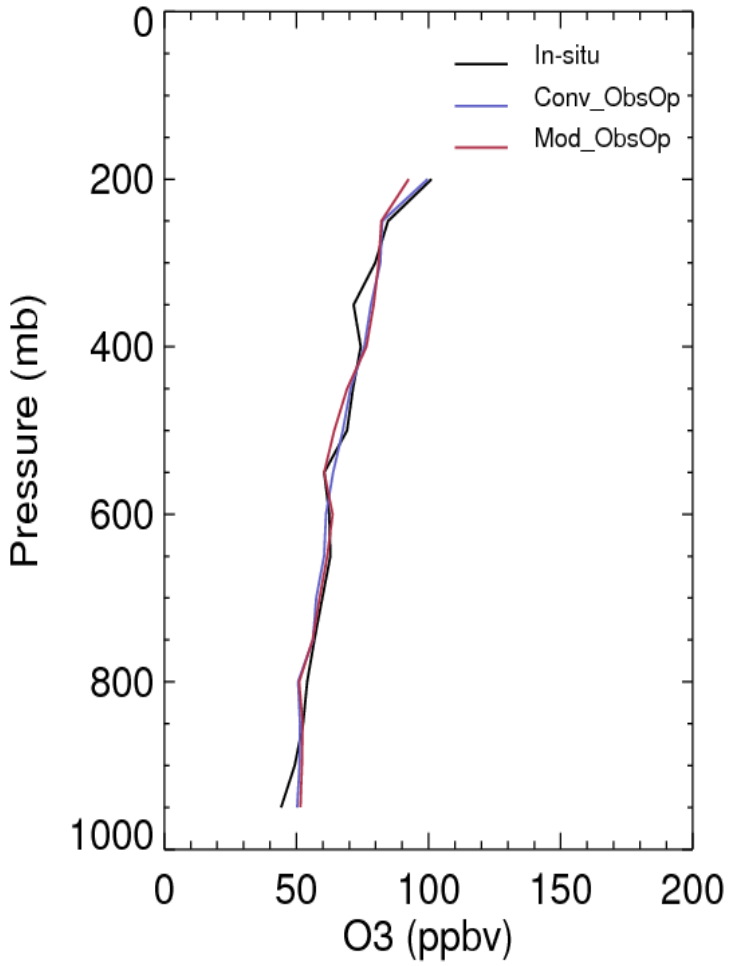

Figure 3.25: The O_3 analysis vertical profiles for the different choices of the observation operator. Plotted are the median profiles of the in situ aircraft data in black ("In-situ"), the conventional observation operator for the O_3 retrieval assimilation results in blue ("Conv_ObsOp"), and the modified observation operator for the O_3 retrieval assimilation results in red ("Mod_ObsOp"). All analysis results are with RAQMS O_3 production-loss parameterization and convective mixing of O_3 in the model.

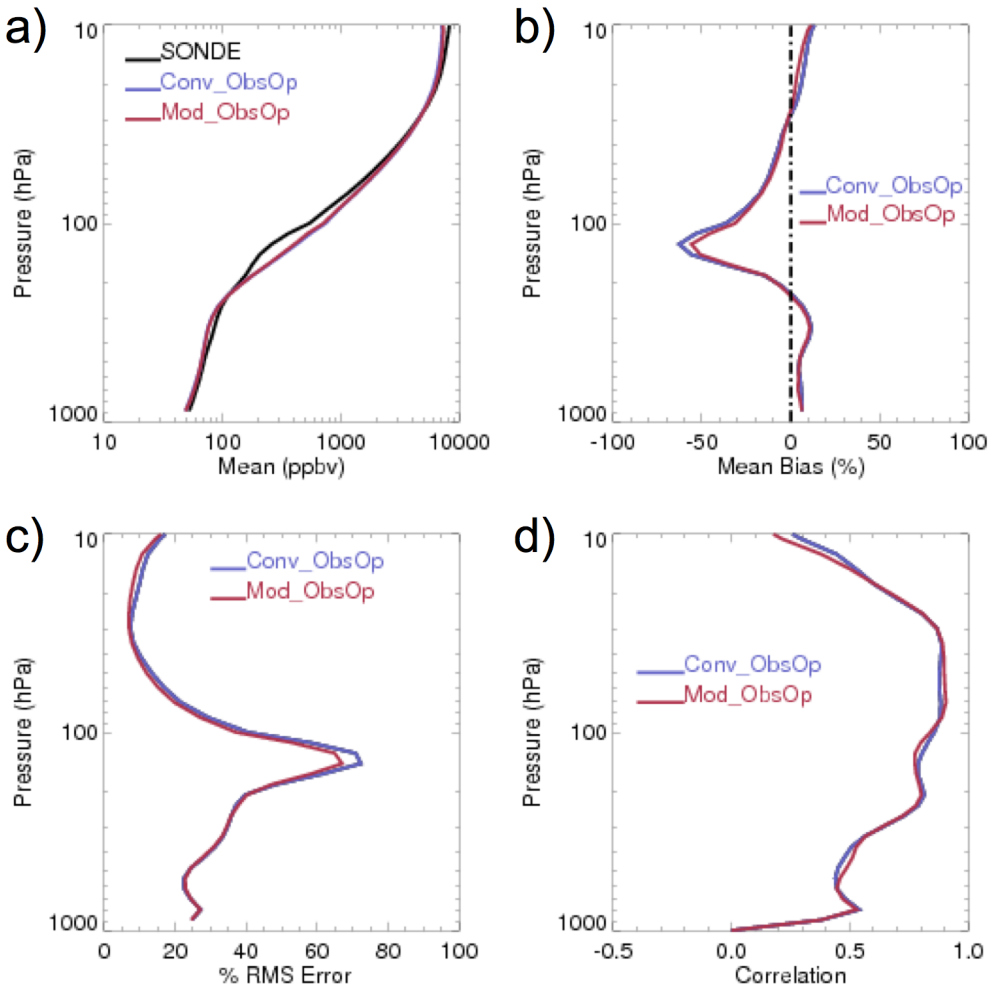

Figure 3.26: Vertical profiles of the O_3 analyses for the two different choices of the observation operator. Also shown is the O_3 profile based on the 217 ozonesondes launched between 10 July 2004 and 15 August 2004. In all panels "Conv_ObsOp" (blue) is analysis results using the conventional observation operator for the O_3 retrieval assimilation and "Mod_ObsOp" (red) is analysis results using the modified observation operator for the O_3 retrieval assimilation. All analysis results are with RAQMS O_3 production-loss parameterization and convective mixing of O_3 in the model. Panel (a) shows the time averaged mean vertical profiles (in ppb volume mixing ratio), panel (b) the mean bias (in percent), panel (c) the RMS error (in percent), and panel (d) the correlation between the model results and the ozonesondes.

and the assimilation of the O_3 retrieval affects only the O_3 fields. We compare the two systems using the RAQMS O_3 production-loss parameterization and the original value of the observation error for the O_3 retrievals. In the univariate system, the O_3 observation can have an effect on the analysis of the meteorological fields through the stratospheric radiative processes in the model integrations that provide the background forecasts.

In Figure 3.27 we compare the O_3 analyses to the aircraft-based measurements. We find that the multivariate assimilation of the O_3 retrievals provides more accurate analyses than the univariate assimilation at almost all atmospheric levels in the troposphere. A similar conclusion can be drawn for the stratospheric levels based on the verification against ozonesondes (Figure 3.28). However, the verification against the ozonesondes also suggests that the univariate assimilation provides more accurate results in the layers between 200 and 600hPa.

3.4 O_3 Results Discussion

We have described the results of the assimilation of SBUV/2 O_3 retrieval observations. Ours is the first attempt at multivariate assimilation of SBUV/2 O_3 retrieval observations into an operational model with an ensemble-based Kalman filter.

The performance of our implementation was assessed by comparing the O_3 field analysis results to aircraft and ozonesonde observations obtained from the INTEX-A field mission. We find that our data assimilation system provides an accurate

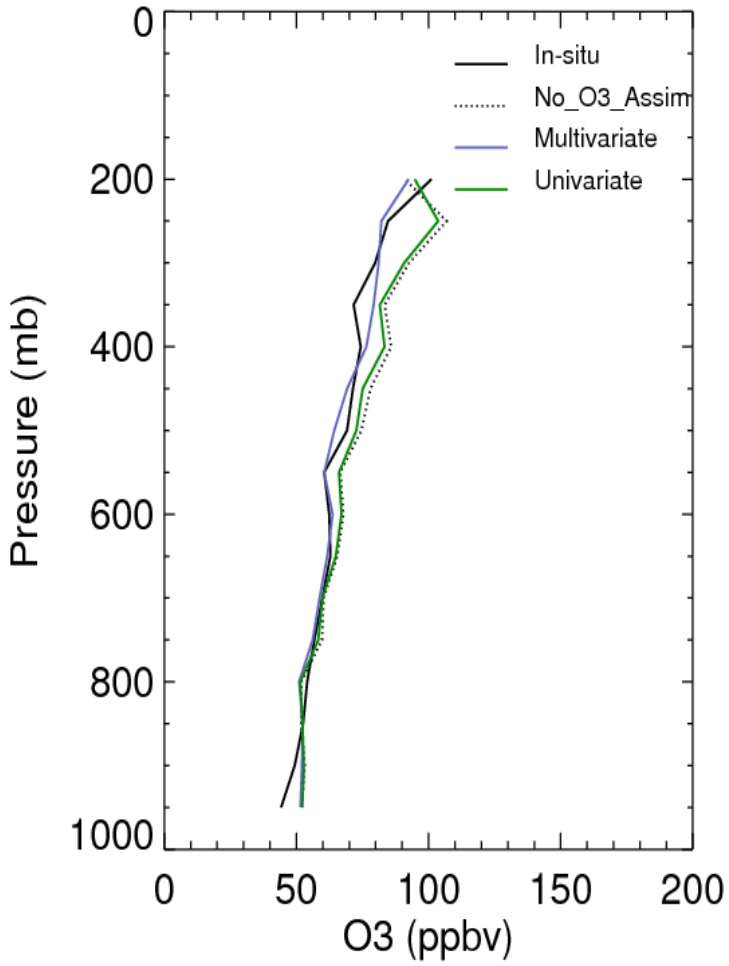

Figure 3.27: Comparison of the O_3 analysis profiles obtained by the multivariate and univariate assimilation of the O_3 retrievals to aircraft-based measurements of the O_3 field. Plotted are the median profiles of: the in situ aircraft data in solid-black ("In-situ"), no O_3 assimilation in dotted black ("No_O3_Assim"), multivariate O_3 retrieval assimilation in blue ("Multivariate"), and univariate O_3 retrieval assimilation in green ("Univariate"). All analysis results are with RAQMS O_3 production-loss parameterization and convective mixing of O_3 in the model.

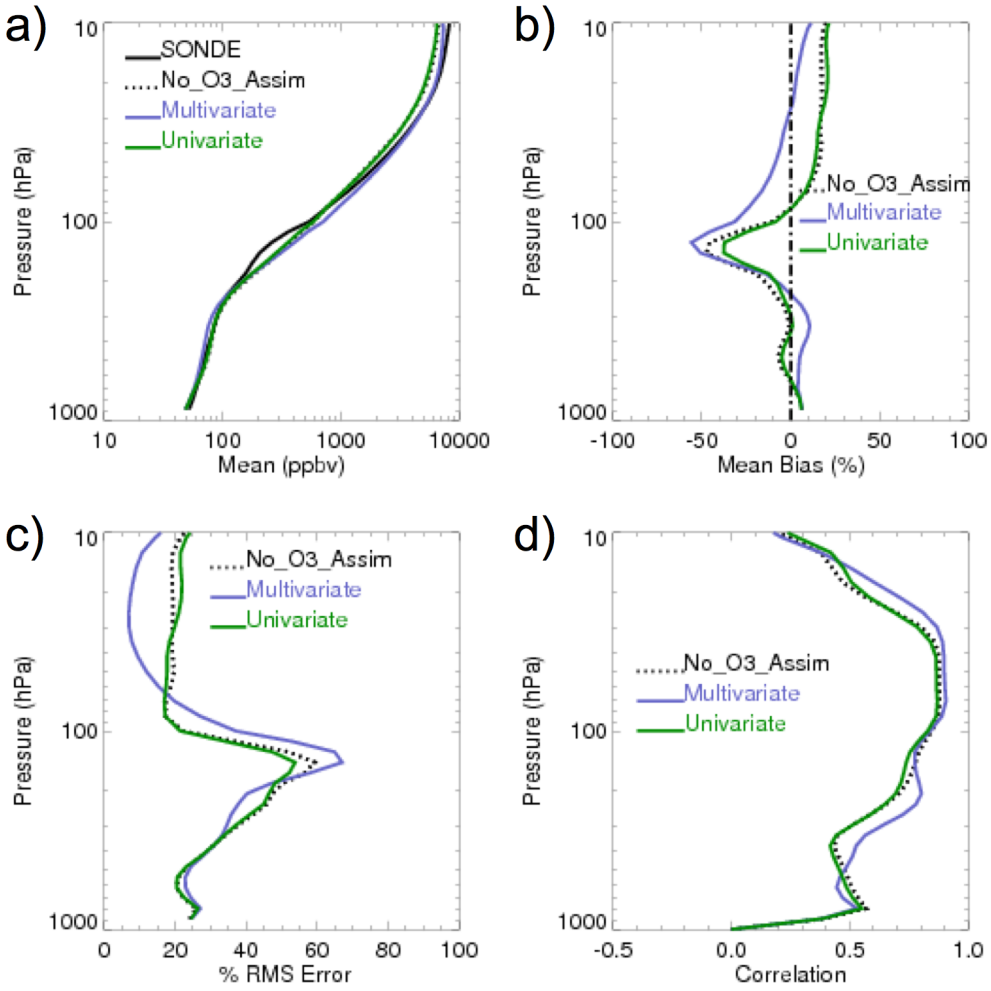

Figure 3.28: Comparison of the multivariate and univariate analysis of the O_3 profiles to the ozonesonde measurements. Ozonesonde measurements, "SONDE" (black solid in panel (a)), were acquired from 217 launched sondes between 10 July 2004 and 15 August 2004. In all panels "No_O3_Assim" (black dotted) is analysis results from no O_3 observations assimilated, "Multivariate" (blue) is analysis results from multivariate O_3 observation assimilation and "Univariate" (green) is analysis results from univariate O_3 observation assimilation. Panel (a) shows the time averaged mean vertical profiles (in ppb volume mixing ratio), panel (b) the mean bias (in percent), panel (c) the RMS error (in percent), and panel (d) the correlation between the model results and the ozonesondes.

estimate of the atmospheric state of the O_3 trace gas when realistic 3-dimensional time-dependent tropospheric background states are used. Most importantly, our tropospheric O_3 field analysis is far more accurate than that of the operational NCEP GFS analysis system. The accuracy of our system is also better than that of the RAQMS chemical modeling system, according to the median statistic for the comparison against aircraft observations, and the accuracy of our system is competitive with the RAQMS chemical modeling system when compared with the ozonesonde observations.

The impact of O_3 assimilation on the meteorological fields was assessed by comparing the NCEP-GFS with and without the O_3 observation assimilation. However, in these analysis and forecast experiments we saw, at times, a strong negative impact on most of the meteorological fields from the multivariate assimilation of O_3 observations when no observation inflation factor was applied. We cannot conclude whether this was caused by O_3 observation bias, deficiencies in the O_3 model (either from sub-grid scale processes or RAQMS O_3 production-loss estimates) and/or deficiencies in the O_3 observational error. However, we did find that by increasing the value of the prescribed O_3 observational error by a factor of 2 or 4 we eliminated the negative impact on the analysis and forecast of the meteorological fields, and obtained a positive impact on the geopotential height field in the stratosphere.

We also found that our modified observation operator performed better than the conventional form of the observation operator over the region of 200 to 100 hPa. Over all other vertical levels, the two operators were comparable. And we also found that the multivariate assimilation of O_3 out-performed the univariate assimilation

of ozone in both the troposphere and the upper statrosphere. Only in the region between 200 and 60 hPa did the univariate assimilation perform better.

Chapter 4

CO Assimilation Experiments

In this chapter, we discuss the multivariate assimilation of MOPITT CO retrievals. In what follows, we describe the assimilated MOPITT observations (the conventional meteorological observations are discussed in section 3.1.1), as well as the observations used for verification. The results of the assimilation of the MOPITT observations are verified in a similar manner as the experiment which we assimilated SBUV/2 observations.

4.1 CO Observations

4.1.1 Assimilated CO Observations

The CO observations assimilated are version 3 CO retrievals derived from the Measurements Of Pollution In The Troposphere (MOPITT) instrument deployed on the NASA Terra satellite (Drummond and Mand 1996, Emmons et al. 2007). We assimilate these observations for the period between 000UTC 1 July 2004 and 000UTC 15 August 2004. Vertical profiles of CO are derived from gas correlation spectroscopy of the observed emitted and reflected radiance. As the radiance enters the sensor, it passes along two different paths through onboard containers of carbon monoxide and methane. The different paths absorb different amounts of energy, leading to small differences in the resulting signals that correlate with the presence

of these gases in the atmosphere. For a more in-depth description of the instruments, see Drummond and Mand (1996). We assimilate the CO vertical profiles using the version 3 algorithm discussed in Deeter et al. (2003).

MOPITT CO data is quality controlled following the approach of Arellano et al. (2007). In particular, we limit the assimilated observation to retrievals that are (i) not at the surface, (ii) have less than 50% contribution form the a priori and (iii) report a mixing ratio value greater than 30ppb.

A map of 6 hours worth of MOPITT observations is shown in Figure 4.1. Every 6 hours approximately 40,000 vertical retrieval profiles are processed. Each of these vertical profile retrievals include up to 6-levels in the vertical. The reported MOPITT retrieval errors are, on average, 70-80% of the retrieved level value, but can be as low as 20% and as high as 200% of the retrieval level. In Figure 4.2 we show the distribution of percentage observation error for a sample of 12,000 observations. These errors were determined through a number of experiments comparing retrievals to in situ measurements from aircraft (Emmons et al., 2007).

Provided with the MOPITT CO retrieval observations are: the variances of the retrieval $\hat{\boldsymbol{\epsilon}}$, the a priori vertical profile $\mathbf{z_a}$ and the averaging kernel matrix $\mathbf{A}$. We are also provided with the variances and covariances of MOPITT retrievals. However, as mentioned earlier, the current version of the LETKF does not specify the covariance information.

The a priori vertical profile for the MOPITT CO retrievals is spatially and temporally invariant. The vertical profile is generated from 525 in situ profiles from aircraft during eight atmospheric chemistry field campaigns. At higher levels, the

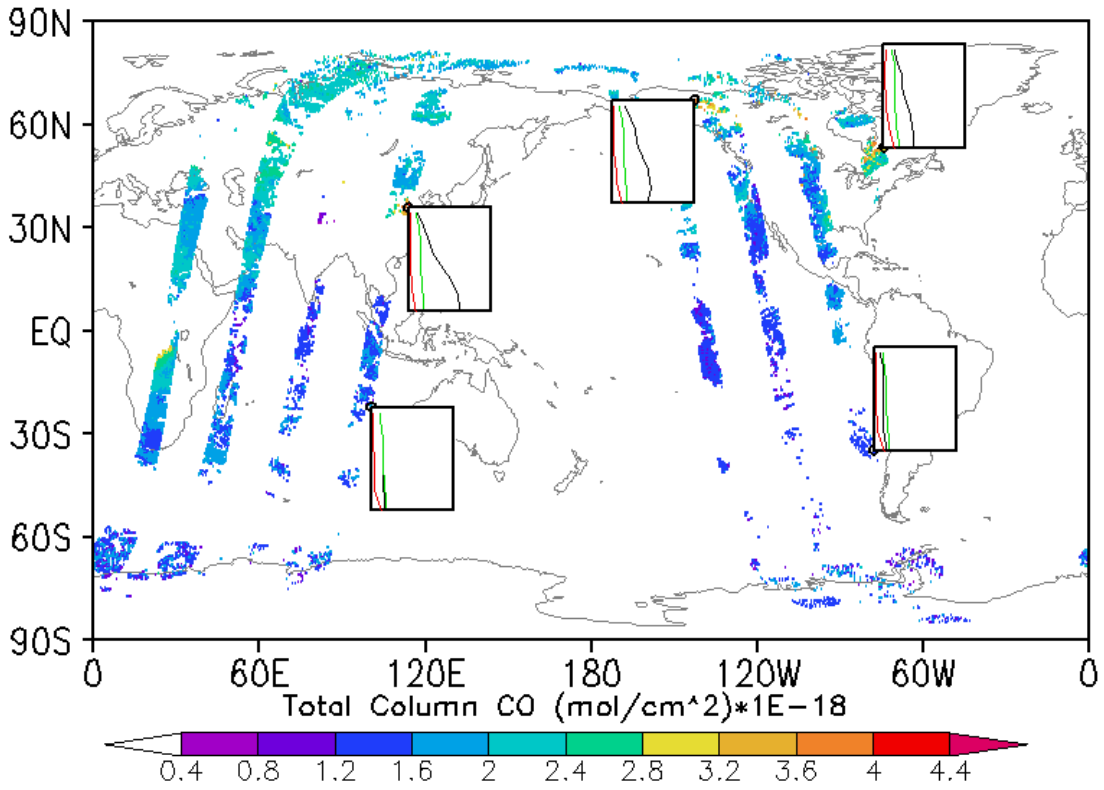

Figure 4.1: MOPITT CO observations +/- 3-hours 000UTC 19 July 2004. Colors represent total column amounts in molecules cm^{-2}. Inset figures show mixing ratio vertical profiles with ordinate pressure from 1000 to 100 hPa and abscissa from 0 to 600ppb. The inset figure show retrievals (black), retrieval error (red), and a priori vertical profile (green).

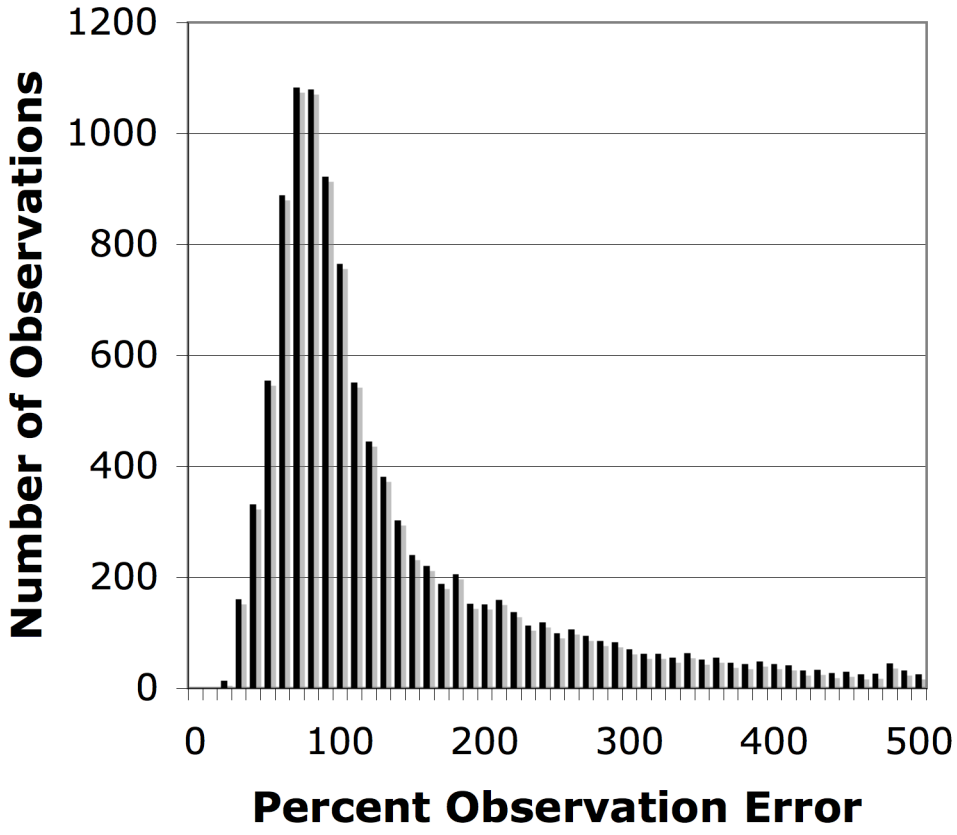

Figure 4.2: Histogram of MOPITT CO observation errors in percentage of retrieval for a sample of 12,000 observations +/- 3-hours 00UTC 1 July 2004.

in situ observations were extended vertically using the chemical transport model "MOZART" (Deeter et al., 2003).

A unique averaging kernel is provided for each of the MOPITT CO retrievals. It is not explicitly included with the retrievals; however, it is calculated from the retrieved error covariance matrix and a fixed a priori covariance matrix. For more details see Deeter et al. (2003).

4.1.2 CO Verification Aircraft Observations

The CO observations on the 13 DC-8 flights (see Figure 3.6) during the INTEX-A experiment were collected by G. Sachse using a fast response Tunable Diode Laser (TDL) absorption spectrometry instrument called DACOM (Differential Absorptions CO Measurement). Detection of CO is accomplished by modulating the TDL wavelength across a cell containing ambient air and then detecting the periodic attenuation experienced by the laser beam due to absorption by CO molecules. The accuracy of the measurements are 1ppb/5seconds (+/-5%) (Singh et al., 2006). The system is fully described in Sachse et al. (1987). The accuracy and density of this data set makes it extremely useful for tropospheric verification of our experimental results.

4.2 Impact on CO from Modeling Modifications

The methodology we use for the validation of the changes in the model for CO is identical to that we described in section 3.2. In Figure 4.3 we compare the

CO field from GFS model simulations with the in situ CO data. The comparison is made by interpolating the chemical fields from the model simulations to the DC-8 flight track, sampling the model at the frequency of the in situ measurements, then binning the modeled and measured values into 50 hPa pressure bins to calculate the median statistic.

In Figure 4.3 the black line is the median profile of the in situ aircraft observation results, the green line shows the median calculated analysis profile result without using convective mixing of CO and the red line shows the median calculated profile after adding convective mixing for CO. It can be seen that convective mixing improves the vertical distribution of the CO in the troposphere. When no convective mixing is included, there is an excessive amount of CO found near the surface. Convective mixing transports higher concentrations of CO at the surface to the upper troposphere.

There is no impact on the meteorological fields from the modifications of the model to incorporate the CO transport into the GFS model. This occurs because, unlike for the ozone, there is no feedback between the CO fields and the meteorological fields in the model.

4.3 Assimilation of CO Observations

In this section, we compare the performance of two different configurations of the analysis-forecast system. In the first configuration, no CO observations are assimilated. In the second configuration, CO observations are assimilated multivari-

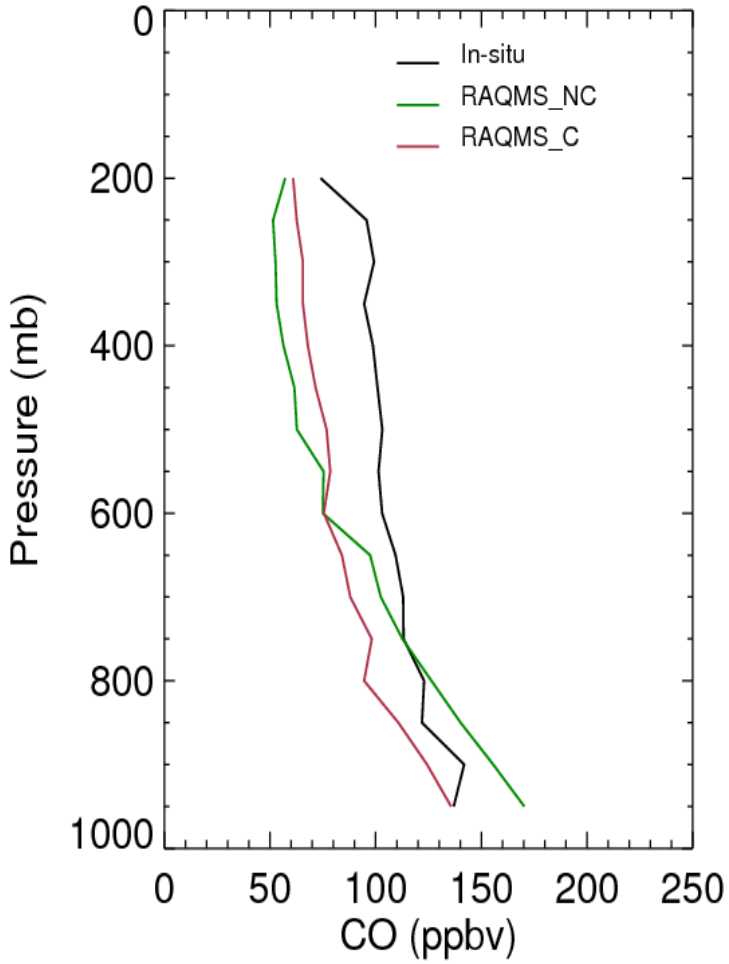

Figure 4.3: Comparison between different model modification CO fields and aircraft measurements. The aircraft measurements were acquired on 13 DC-8 flights between 10 July 2004 and 15 August 2004. Plotted are the median profiles of: the in situ aircraft data in black ("In-situ"), the analysis results using RAQMS CO production-loss parameterization and no CO convective mixing in the model in green ("RAQMS_NC"), and the analysis results using RAQMS CO production-loss parameterization and CO convective mixing in the model in red ("RAQMS_C"). All analysis results assimilated only conventional meteorological observations.

ately with the meteorological observations. Hereafter, we refer to the former as the "no-CO experiment" and the later as the "CO experiment."

4.3.1 CO Assimilation Impact on Meteorological Fields

We first compare the no-CO and CO experiments to the high resolution operational NCEP analyses (Figure 4.4). The error statistics are averaged in one of three regions of the globe: Northern Hemisphere (30N to 90N), Tropics (30S to 30N) and Southern Hemisphere (90S to 30S). In the figure, a negative value implies that the assimilation of CO observations has a negative impact on the verified field and a positive value implies that the assimilation of CO observations has a positive impact on the verified field. Similar to the assimilation of O_3 (Figure 3.11), the assimilation of CO observations has a clear negative impact on the meteorological fields. There is some positive impact on the Southern Hemisphere geopotential height field but these positive impacts are dwarfed by the negative impacts on the wind. The negative impact from the assimilation of CO observations on the meteorological fields is still present at the 48-hour forecast time (Figure 4.5). However, the magnitude of this negative impact is smaller in comparison to analysis time.

Finally, we compare the 48-hour forecasts started from analyses that assimilated CO observations to radiosonde observations (Figure 4.6). This figure does not show the negative impact on the meteorological fields that was seen in the comparison between the CO and no CO experiments.

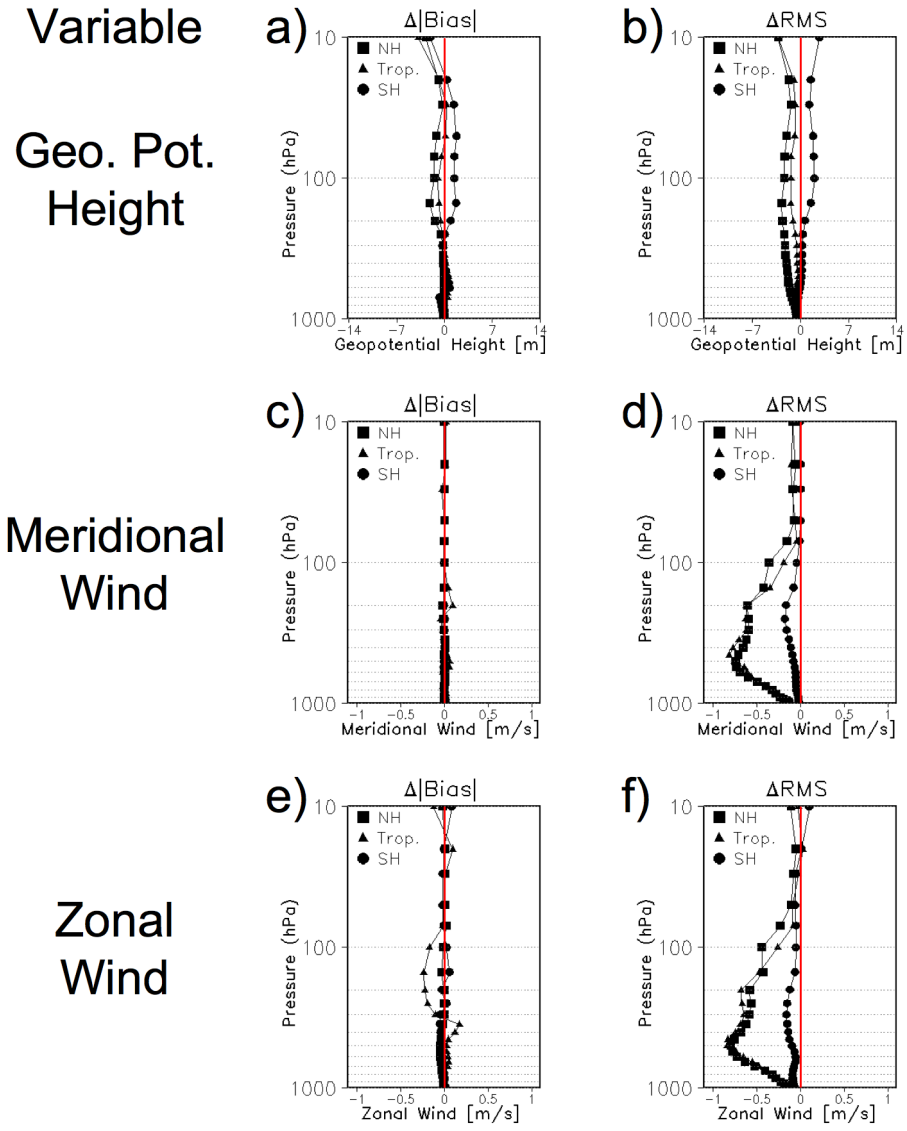

Figure 4.4: MOPITT CO observation assimilation impact on the meteorological fields. Same as Figure 3.11, except here CO observations were assimilated instead of O_3 observations.

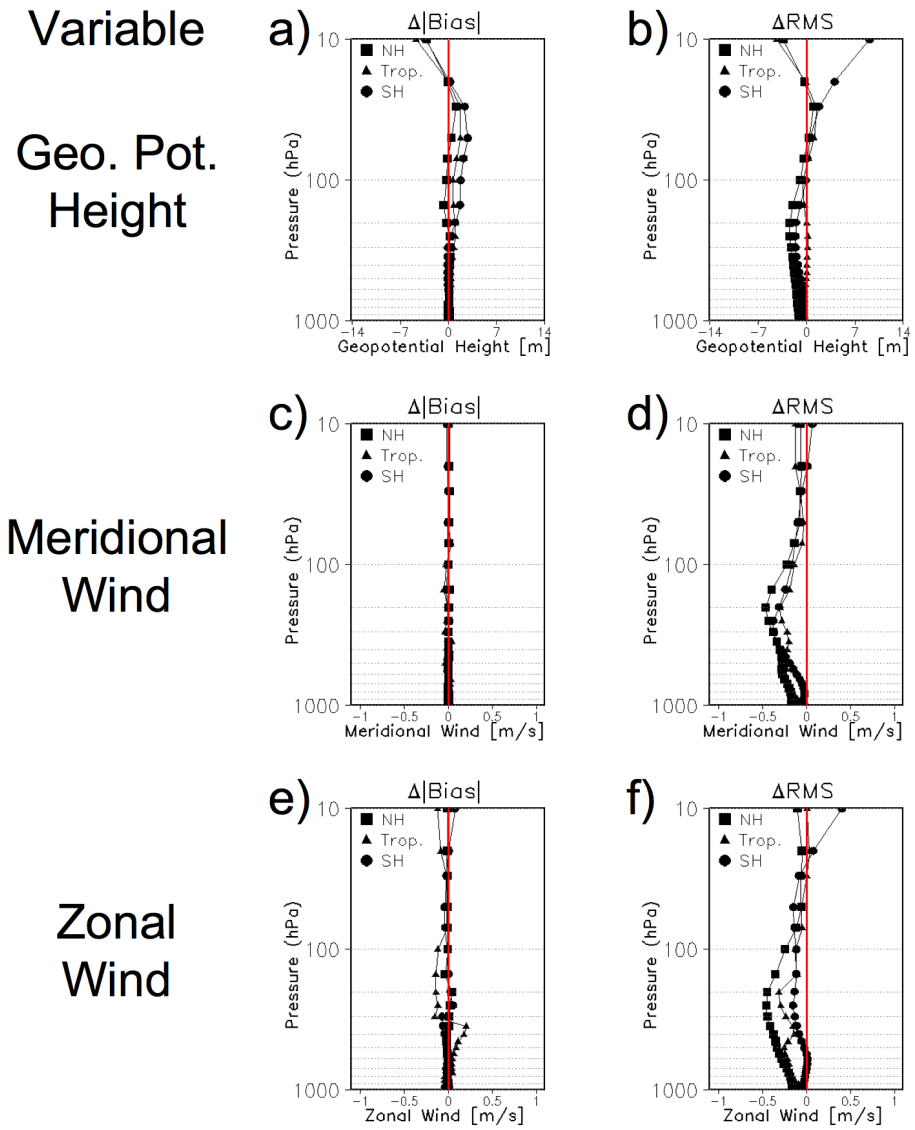

Figure 4.5: 48-hour forecast MOPITT CO retrieval observation assimilation impact on the meteorological fields verified with NCEP GFS analysis. Same as Figure 3.12, except here CO observations were assimilated instead of O_3 observations.

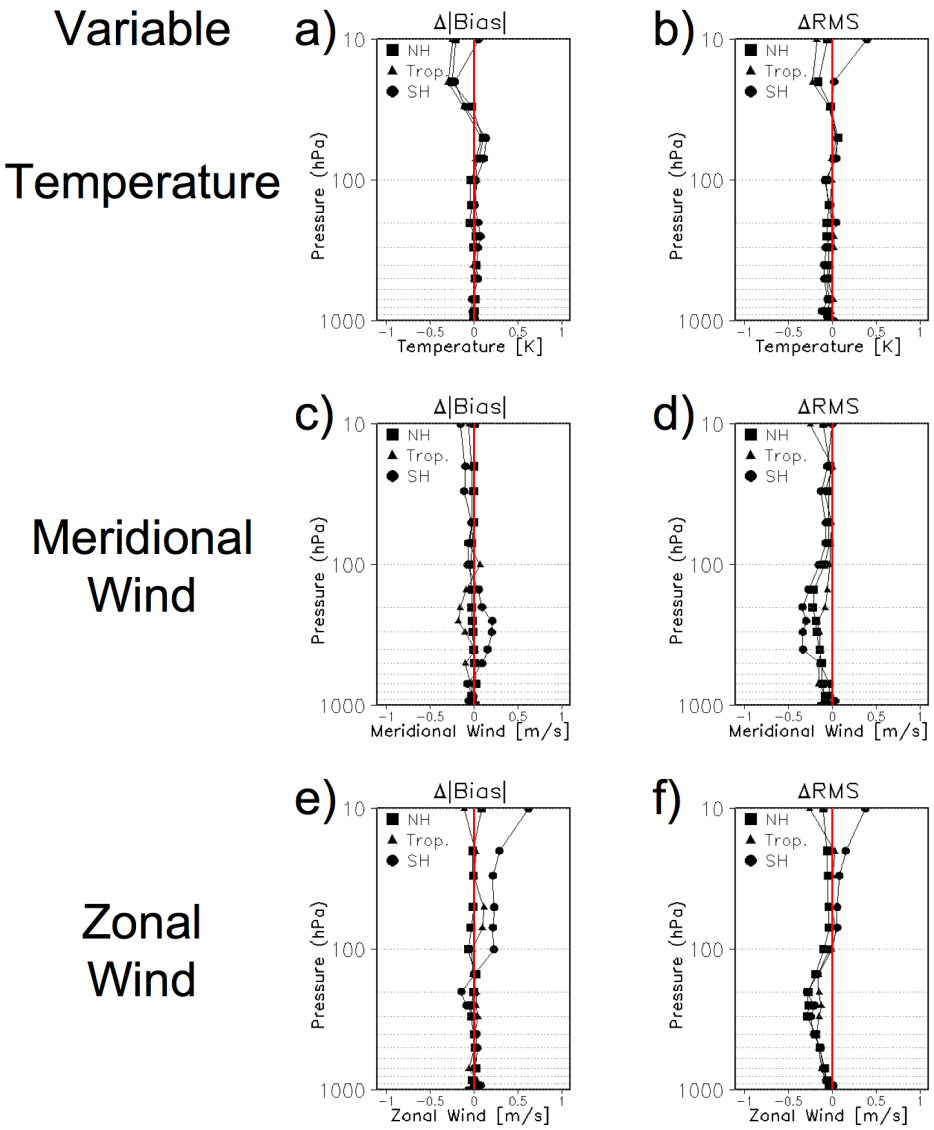

Figure 4.6: 48-hour forecast MOPITT CO retrieval observation assimilation impact on the meteorological fields verified with radiosonde observations. Same as Figure 3.13, except here CO observations were assimilated instead of O_3 observations.

4.3.2 CO Meteorological Field Impact Investigation

As for the ozone, we consider three potential factors that may contribute to the negative impact of the assimilation of CO on the meteorological files: bias in the CO observations, deficiencies in the CO modeling and misspecification of the CO observation error.

4.3.2.1 CO Observation Bias

The average bias in the version 3 MOPITT CO data was found to be between 1.9% and 14.4% of the retrieval values over the summer of 2004. This validation was made against the aircraft measurements from three experiments: CO2 Budget and Rectification Airborne (COBRA), Measurement of OZone, water vapor, carbon monoxide and nitrogen oxides by Airbus In-service airCraft (MOZAIC) program, and the INTEX-A aircraft observation (Emmons et al., 2007). This bias should be compared with the 70-80% average reported error of the MOPITT retrievals used in the assimilation. The average bias is at least 4 times less than the reported error, but still not negligible.

4.3.2.2 CO Model Error

The RAQMS model of CO was found to have a bias of less than 1% of the computed mixing ratio globally and less than 1.2% over the continental United States (Pierce et al., 2007). However, similar to the case of ozone, it is known that the sub-grid scale process parameterizations, such as convective mixing, are

deficient in modeling sub-grid scale transport processes and, as discussed in section 2.1.2 this deficiency could lead to a negative impact on the meteorological fields. This deficiency is of particular importance for CO, since this problem mainly affects the troposphere and the errors in the wind analysis are seen in the troposphere.

4.3.2.3 CO Observation Error

The primary known deficiency of our specification of the CO observation error in the analysis system is that we neglect the covariance between the retrievals. As for the ozone, we account for the neglected covariance by inflating the prescribed variance of the CO observation error. We also tested two other potential approaches: superobing (i.e., averaging several nearby observations (Lorenc, 1981)), and thinning the observations (i.e., using only a few observations in a given local region). The latter two approaches did not have as clear of an impact on our results as the observation error inflation; therefore, we do not show results from these experiments. As for the ozone observation error inflation experiments, we multiply the standard deviation of the CO observation error by a gradually increasing factor of 2, 4 and 10.

Shown in Figure 4.7 is the zonal wind field verified against the NCEP GFS analysis at analysis time. In Figure 4.8 we show the zonal wind field verified against the NCEP GFS analysis at 48-hour forecast time. In Figure 4.9 we show the zonal wind field verified against radiosonde observations at 48-hour forecast time.

Based on Figure 4.7 the conclusion would be to use an observation error infla-

tion factor between 4 and 10; however, taken together with the other two verification figures one would favor a factor between 1 and 2. Although at analysis time we decreased the negative impact on the meteorological field by inflating the standard deviation of the observation error by as much as a factor of 10, it is clear from the forecast verification that the optimal inflation factor is less than 10.

4.3.3 CO Assimilation Impact on CO Fields

In Figure 4.10, we summarize the results of the observation error inflation experiments for CO. In contrast to the behavior we observed for the ozone, as the observation error inflation factor is increased, the analyzed median value of the CO drifts from the in situ measurements. Comparing our results to that for the RAQMS analysis (Figure 4.11), it can be seen that an observation inflation factor of 2 performs better than the RAQMS analysis for most vertical levels.

4.4 CO Results Discussion

We have described the results of the assimilation of MOPITT CO retrieval observations with an implementation of the LETKF data assimilation algorithm on the NCEP GFS model. Ours is one of the first successful attempts at multivariate assimilation of MOPITT CO retrieval observations with a model of operational complexity and an ensemble-based Kalman filter. The only other similar attempt we are aware of is by Arellano et al. (2007), who assimilated MOPITT CO data using a global atmosphere model, the Community Atmosphere Model (CAM3).

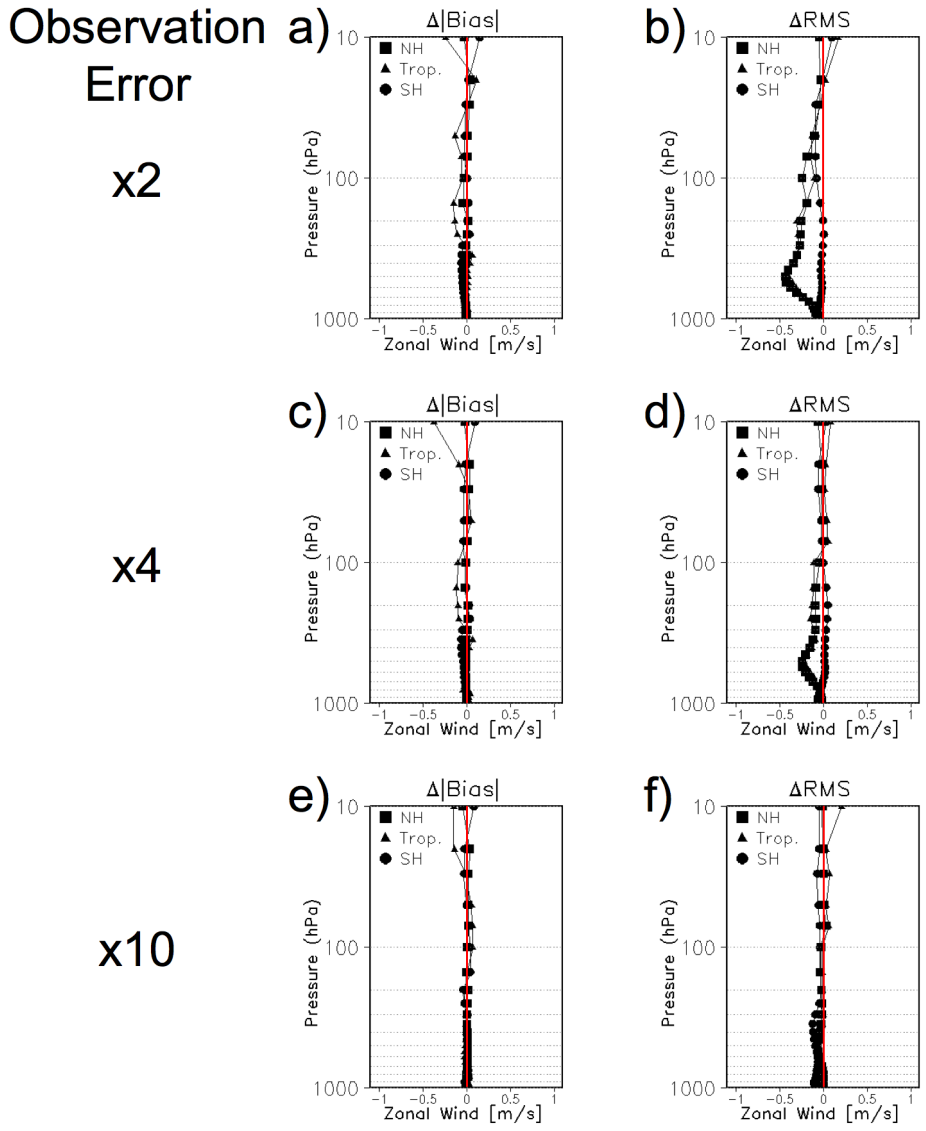

Figure 4.7: CO observation error inflation impact on the zonal wind field verified with NCEP GFS analysis. Same as Figure 3.15, except here CO observations were assimilated instead of O_3 observations.

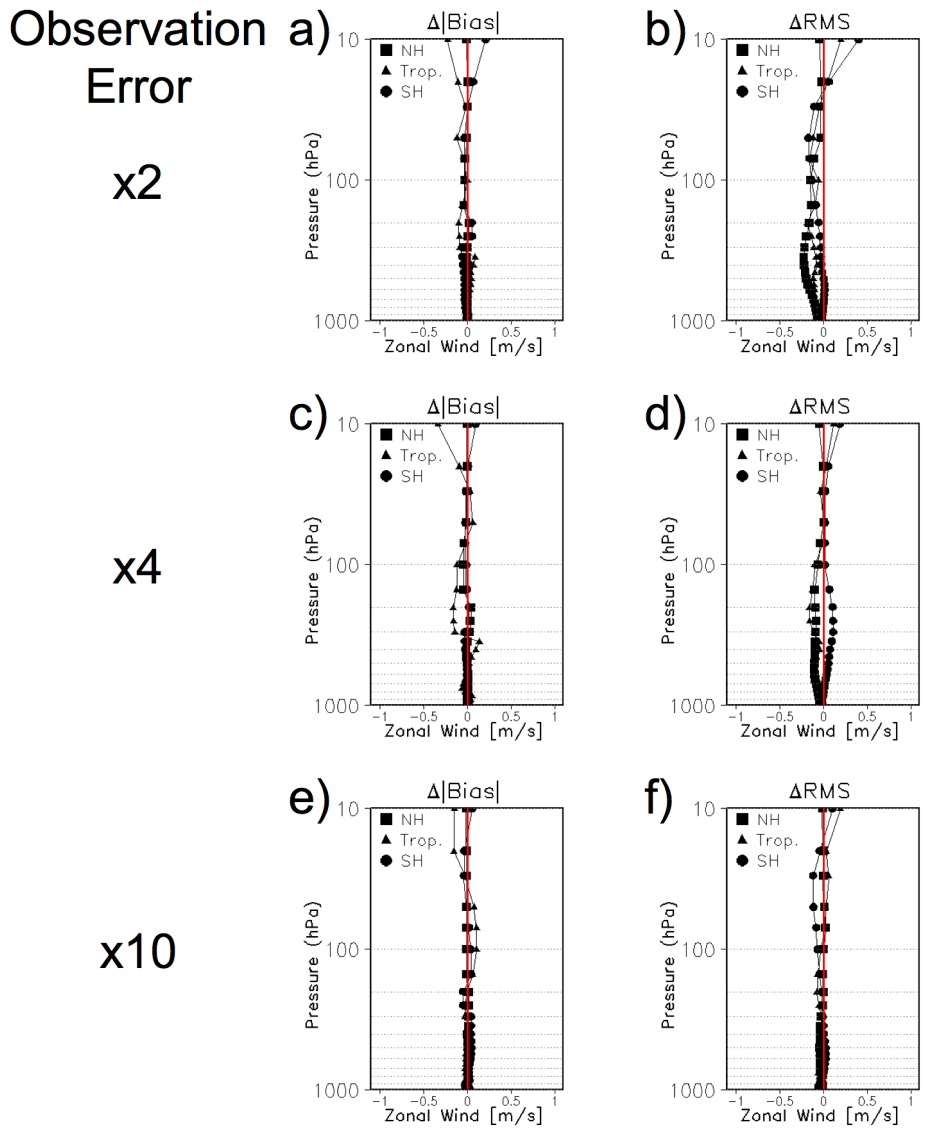

Figure 4.8: CO observation error inflation impact on the zonal wind field 48-hour forecast from the analysis and verified with the NCEP GFS analysis. Same as Figure 3.16, except here CO observations were assimilated instead of O_3 observations.

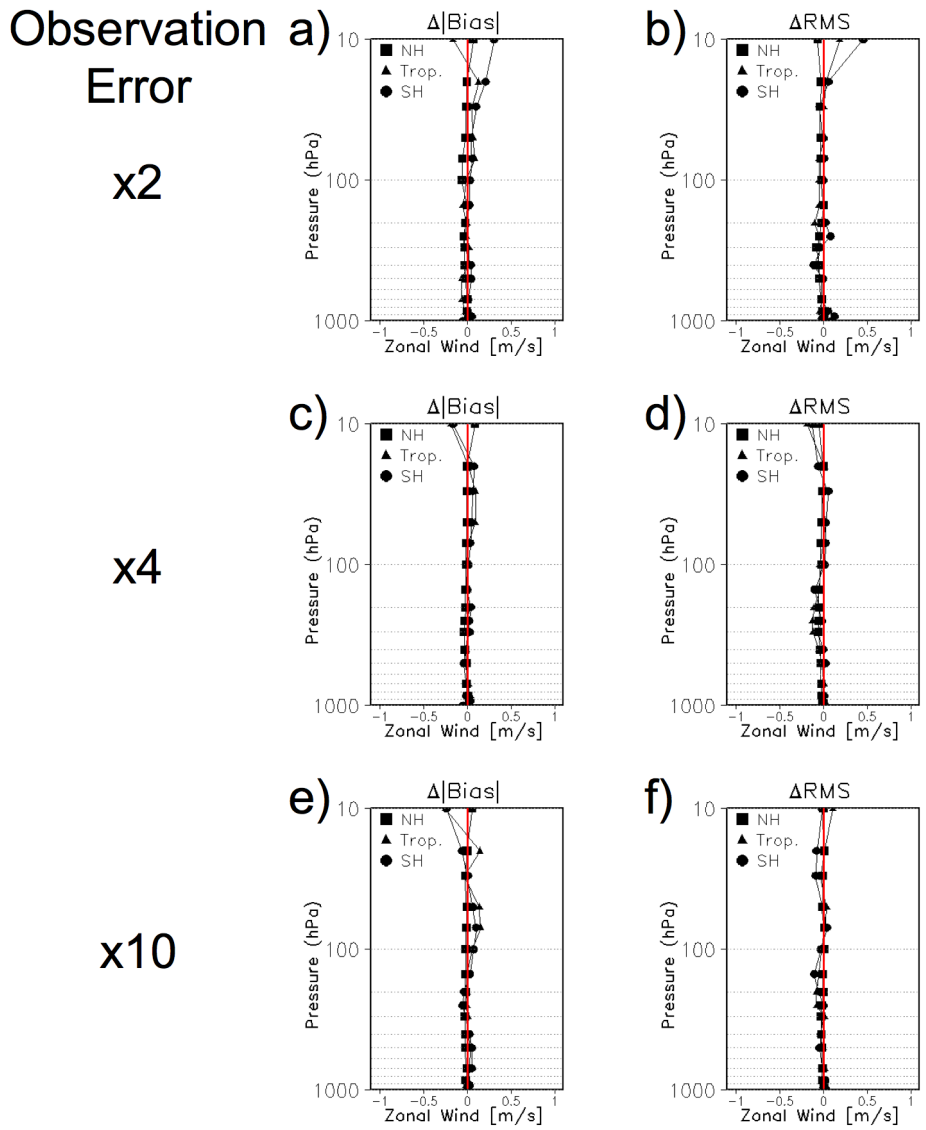

Figure 4.9: CO observation error inflation impact on the zonal wind field 48-hour forecast from the analysis and verified with the radiosonde observations. Same as Figure 3.17, except here CO observations were assimilated instead of O_3 observations.

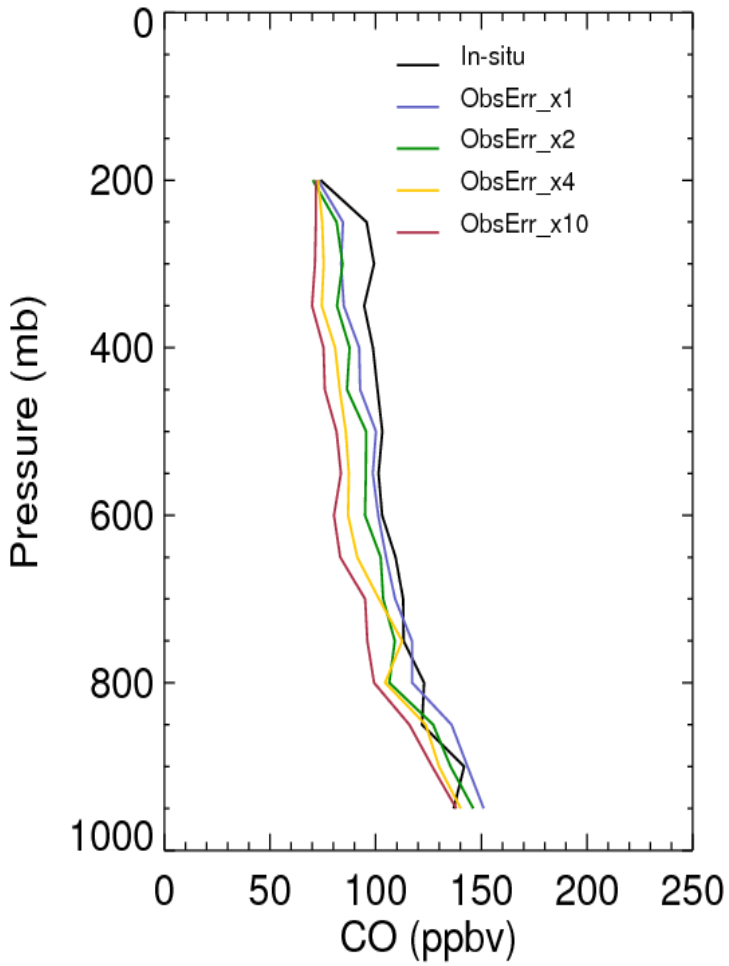

Figure 4.10: Comparison between different CO observation error inflation and aircraft measurements. Same as Figure 3.21, except here CO observations were assimilated instead of O_3 observations.

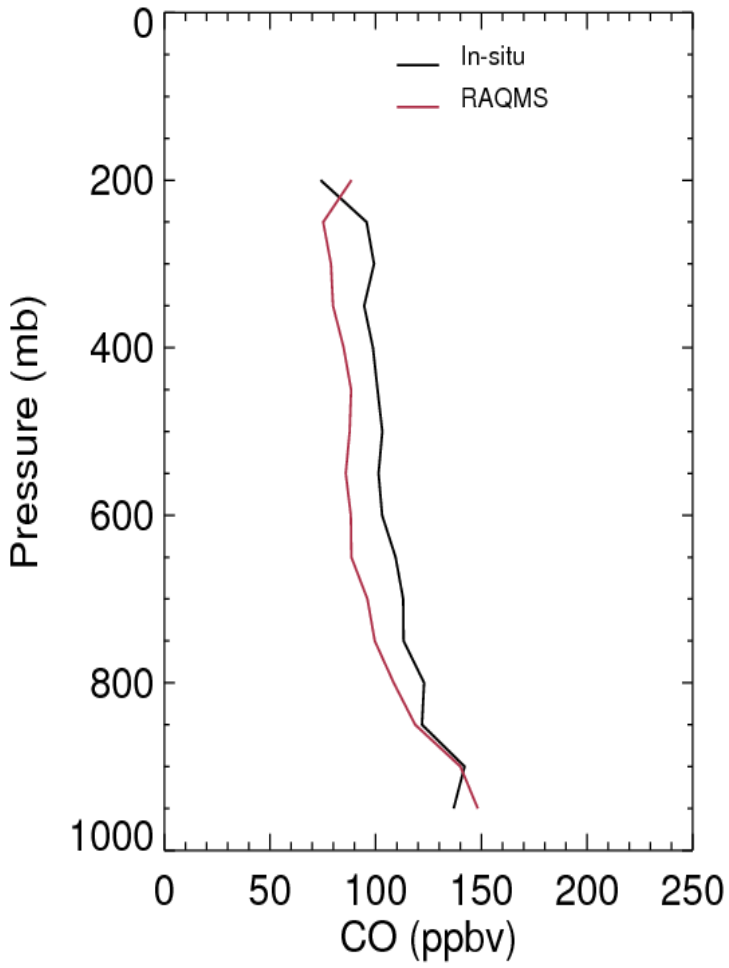

Figure 4.11: Comparison between RAQMS analysis CO results and aircraft measurements. Same as Figure 3.22, except here only RAQMS analysis CO results are reported.

The performance of our system was assessed by comparing the CO field analyses to aircraft observations collected in the INTEX-A field mission. We find that our data assimilation system provides an accurate estimation of the atmospheric state of CO. The accuracy of our system is competitive with the RAQMS chemical modeling system when verified against the aircraft observations. For cases of no observation error inflation and inflation by a factor of 2, the accuracy of our system exceeds that of the RAQMS chemical modeling system.

The impact of the assimilation of CO on the meteorological fields was assessed by comparing the performance of the system that included the assimilation of CO to the performance of the system that did not include the assimilation of CO. The quality of the analysis in these experiments was assessed by verifying the analyzed and forecast meteorological fields against the high resolution NCEP GFS analysis. In these experiments, we found a strong negative impact of the CO assimilation on the analysis and forecast of the meteorological fields. We cannot rule out that CO observation bias or deficiencies in the CO model from sub-grid scale processes contributed to this negative result. We did find, however, that by increasing the standard deviation of the prescribed observational error by a factor of 2 we were able to eliminate most of the negative impacts on the wind fields in the 48-hour forecasts. Unlike the case of the O_3 assimilation, we were not able to improve the analysis or forecast of any of the meteorological parameters by the assimilation of the CO observations.

Chapter 5

Conclusions

We have described an implementation of the LETKF data assimilation system on a modified form of the operational NCEP GFS model for the assimilation and prediction of trace gas concentration. Our modifications to the NCEP GFS include: (1) the addition of convective mixing for the trace gases to the parameterization package and (2) the definition of production-loss terms in the prognostic equations for the concentration of the trace gases by the output of the state-of-the-art atmospheric chemical model, RAQMS. Our study is the first attempt at a multivariate assimilation of SBUV/2 O_3 retrievals in an operational model with an ensemble-based Kalman filter. In addition, the results presented in the dissertation are one of only two successful attempts of ensemble-based Kalman filter assimilation of MOPITT CO retrieval observations in a state-of-the-art global circulation model.

The performance of our implementation in analyzing and predicting the trace gas concentrations was assessed by comparing the analyses and forecasts to observations collected in the INTEX-A field mission. We find that the accuracy of our system is competitive with that of the RAQMS chemical modeling system. In addition, our system is far more accurate than the operational NCEP system in analyzing the tropospheric O_3 concentration.

The impact of trace gas assimilation on the meteorological fields was assessed

by comparing the results of the experiments to the results of the analysis-forecast experiments in which no trace gas was assimilated. We find that the assimilation of O_3 has a mixed impact on the accuracy of the analyzed and forecasted meteorological fields, while the assimilation of CO has a negative impact. We find that, by inflating the prescribed observation error for the trace gases, we can eliminate most of the negative impact on the analysis and forecast of the meteorological fields, without much reduction to the positive impact on the analysis of the concentration of the trace gases.

Appendix A

Poleward Movement of Upper-Tropospheric Fronts and Regional Surface Temperatures: A Case Study of the U.S. Great Plains, 1980 to 2001

Authors: D. Kuhl, D. Baker, R. Hudson

Submitted to the Journal of Climate

A.1 Abstract

This paper explores the relationship of the poleward movement of upper-tropospheric fronts and jet streams with long-term regional temperature changes. A case study of the United States Great Plains for 1980-2001 reveals that this region had an average daily temperature rise over this period of $0.35°C$ based on station data. Using the total column ozone data from the Total Ozone Mapping Spectrometer to identify upper-tropospheric fronts on a daily basis, this region was divided into three meteorological regimes: (1) tropical (between the equator and subtropical jet); (2) midlatitude (between the subtropical and polar jet); and (3) polar (between the polar jet and the polar vortex or 60N). All three regime temperatures not only did not rise but showed a cooling trend. The regional warming was due to a percentage increase of the average area in the tropical regime and a percentage decrease of the average area in the midlatitude and polar regimes, consistent with

poleward movement of atmospheric circulation patterns. Over the 22-year period, the tropical regime expanded an additional 7.5% or $1.38 \times 10^5 km^2$, a rate of 3.4% or $6.26 \times 10^4 km^2$ per decade. The results suggest that regional climate change in the midlatitudes may be detected through trends in the average percentage areas of ozone-defined meteorological regimes.

A.2 Introduction

Large-scale atmospheric circulation systems include the polar and subtropical jet streams, upper-tropospheric fronts, baroclinic zones, and storm tracks, all of which are dynamically linked. These systems can be altered by global climate change. The Intergovernmental Panel on Climate Change (IPCC) Fourth Assessment Report (AR4) stated that circulation patterns have moved poleward in both hemispheres over the last 50 years (Trenberth et al., 2007). This shift has the potential to change climate zones by modifying regional winds, clouds, and precipitation patterns. The question explored in this paper is whether it also may cause long-term changes in regional surface temperatures.

There is growing observational evidence for the poleward movement of circulation patterns in research too recent to have been included in AR4. Seidel and Randel (2007) used radiosondes from 1979-2005 to show an increased frequency of high-tropopause ($> 15km$) days, consistent with a widening of the tropical belt by $5^\circ - 8^\circ$ latitude through poleward movement of the subtropical jet. Using satellite measurements of outgoing longwave radiation, Hu and Fu (2007) found evidence

that the Hadley cell has expanded poleward by $2^\circ - 4.5^\circ$ in both hemispheres in 1979-2005. Fu et al. (2006) calculated a poleward shift of approximately one degree for the combined jet streams using satellite-borne microwave sounding unit data. Hudson et al. (2006) reported a poleward movement of 1.1° per decade latitude for the subtropical front and 0.5° per decade latitude for the polar front in the Northern Hemisphere midlatitudes ($25^\circ - 60^\circ N$) from January 1979 to August 2003. Wang et al. (2006), using reanalysis datasets, showed that between the 1958-77 and 1982-2001 periods, the mean zonal position of the storm track moved poleward 181 km in the North Atlantic and 259 km in central Canada.

The dynamical basis for poleward movement of upper-tropospheric fronts, jet streams, and storm tracks is not fully understood. However, studies that use numerical models to simulate global climate change suggest the poleward shift of circulation patterns is a potential climate feedback related to increased greenhouse gases (Hall et al. (1994); Knippertz et al. (2000); Geng and Sugi (2003); Fyfe (2003); Yin (2005); Bengtsson et al. (2006); Jiang and Perrie (2007); Lu et al. (2007); Pinto et al. (2007)). However, their predictions of the poleward shift are an order of magnitude below the observations (Hu and Fu, 2007).

In this study, the connection between poleward movement of atmospheric circulation systems and long-term changes in regional temperature is investigated by using daily satellite measurements of total column ozone to identify the position of upper-tropospheric fronts. Gordon Miller Bourne Dobson was the first to note the correlation between ozone and meteorological variables, including tropospheric temperature, pressure distribution, air density, tropopause height, and tropopause

pressure, in a series of articles during 1926-30 (Dobson and Harrison (1926); Dobson et al. (1927), Dobson et al. (1928); Dobson (1930)). Melvyn A. Shapiro documented the mechanism that links abrupt changes in ozone concentrations with upper-tropospheric fronts and jet streams (Shapiro (1978); Shapiro (1980); Shapiro (1981); Keyser and Shapiro (1986)). He was the first to suggest the use of total column ozone measurements from the Total Ozone Mapping Spectrometer (TOMS) to identify daily front positions (Shapiro et al. (1982)).

Ozone can be used as a dynamical tracer because its chemical lifetime near the tropopause is ≈ 90 days, much longer than its dynamical lifetime of a few days (Holton et al. (1995); Zachariasse et al. (2000)). The fronts can be traced using ozone concentrations because they are marked by the descent of a tongue containing ozone-rich stratospheric air below the tropopause (Gill, 1982). High-ozone air from the stratosphere is believed to enter the troposphere near upper-tropospheric fronts and jet streams through tropopause folds associated with upper-level frontogenesis and the statistically persistent tropospheric breaks near the jet streams, also known as double tropopauses (Koch et al. (2005); Pan et al. (2004); Randel et al. (2007)). Ozone mixing ratios are the highest along the tropopause fold but remain large along the frontal zone compared to air outside the zone Hipskind et al. (1987). When strong lee waves obscured other frontal indicators, Rao and Kirkwood (2005) found ozone concentrations still had a good correspondence with the location of the frontal system observed. These gradients do not dissipate quickly because of strong dynamic resilience to cross-tropopause transport Holton et al. (1995).

It is known that there is a link between upper-tropospheric fronts and surface

temperature. According to potential vorticity theory, the growth of baroclinic eddies is due to the mutual reinforcement of a potential vorticity anomalies on the upper-tropospheric front and surface temperature anomalies. The upper-level jet stream triggers surface wind fluctuations which advect surface temperature anomalies downstream (Takamura et al., 2004). A link has also been documented between surface temperatures and total column ozone. Kiss et al. (2007) conclude that the large number of local factors that could influence temperature fluctuations as well as the complex chemistry that could influence ozone fluctuations are subsidiary and that dynamics dominate both parameters.

Hudson et al. (2003) developed an algorithm to identify high-ozone gradients in TOMS measurements and found that these locations agreed closely with daily front positions in National Center for Atmospheric Research / National Centers for Environmental Prediction reanalysis data. They used the location of subtropical and polar fronts to divide the Northern Hemisphere into three meteorological regimes: tropical, midlatitude, and polar regimes. These regimes can be identified by their distinctive ozone characteristics (see Table A.1). Hudson et al. found that the regional daily mean for total ozone value was relatively constant between the fronts but changed abruptly in concentration and altitude at each front and that these properties vary smoothly from day to day.

The existence of these meteorological regimes has since been confirmed by other studies. Ozone jumps up to one percent have been observed between the tropics and midlatitudes and up to two percent from the midlatitudes to the polar regions (Coldewey-Egbers et al., 2005). Ladstatter-Weissenmayer et al. (2007)

Table A.1: The three meteorological regimes as identified from column ozone data.

Regime	Lower boundary	Upper boundary	Altitude of ozone peak	Seasonal maximum	Seasonal minimum
Tropical	Equator	Subtropical jet	126 ± 26 hPa	July	December
Midlatitude	Subtropical jet	Polar jet	229 ± 46 hPa	April	October
Polar	Polar jet	Polar vortex	338 ± 39 hPa	February	September

found that the total vertical column density of ozone in the East Mediterranean region was highly dependent on whether the area was in a tropical or midlatitude regime. Similarly, Diab et al. (2003) analyzed 56 complete vertical ozone profiles from throughout the year in Johannesburg, South Africa (26S) and found that the seasonality in some of the profiles reflected the differing influences of the tropical and midlatitude source regions. Finally, Seidel and Randel (2007) found a clear distinction between tropical and extratropical regimes, which had a three to five kilometer difference in tropopause height.

Using the Hudson et al. (2006) algorithm, this experiment examines whether long-term changes in the mean latitudes of upper-tropospheric front positions may be responsible for a portion of rising average regional surface temperatures. This analysis focuses on the United States Great Plains during 1980-2001. The next section describes the data and analysis methods, the third section summarizes the temperature and area results, and the fourth section presents discussion and conclusions.

A.3 Methodology

The U.S. Great Plains region was chosen for this study because it has high-density surface temperature observations, contains all three meteorological regimes for most of the year, and minimizes some of the more significant causes of temperature variation such as large orographic or coastal effects. This study defines the Great Plains as $30°-48°N$ and $95°-105°W$ (see Figure A.1). The Great Plains is one of the few remaining areas in the United States that is dominated by agriculture. The terrain is relatively flat with increasing elevation from east to west. The climate is categorized as semi-arid. It has extreme and variable conditions with strong meridional temperature gradients increasing from north to south and zonal precipitation gradients increasing from west to east (Polsky and Easterling, 2001).

TOMS data were used to create daily ozone masks delineating the location of fronts and the area covered by each regime in the site (TOMS, cited 2009). TOMS uses reflected ultraviolet solar radiation to measure total column ozone and daily data are taken over a 24-hour period. The ozone retrieval algorithm accounts for cloudy conditions, solar zenith angle, and radiative transfer processes (McPeters and Labow, 1996). The archived datasets used in this experiment were the version eight, level three hierarchical data format product with improved climatology for ozone vertical profiles (McPeters et al., 2007). Each grid square was $1.00° \times 1.25°$ resolution and the Great Plains region contained a total of 160 grid boxes. The ozone masks labeled each grid box by regime excluding one degree boundaries between regimes, an average of 20 grid boxes per day (see Figure A.1). Mask data were

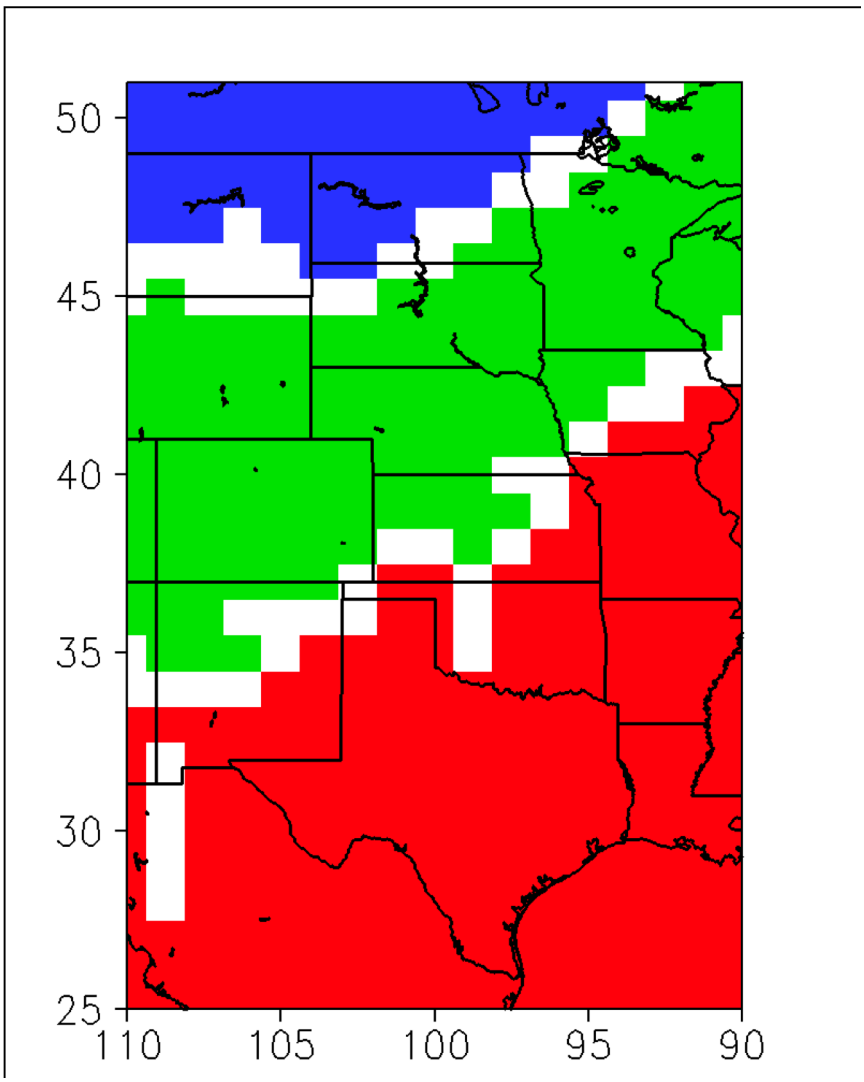

Figure A.1: Division of the Great Plains region (black box) into ozone-defined meteorological regimes for 6 August 1987. The three regimes are tropical (red), midlatitude (green), and polar (blue).

categorized as missing if the algorithm did not converge after five iterations, there were no TOMS data for that day, or over 50% of the TOMS data for that day were missing. More information on the ozone mask algorithm can be found in Hudson et al. (2006). The study period chosen was 1980-2001 to match the availability of these ozone masks.

Station data for daily surface temperature were obtained from U.S. Historical Climatology Network Daily Temperature, Precipitation, and Snow Observations from the Carbon Dioxide Information Analysis Center (CDIAC, cited 2009). Daily resolution is preferable for studies attempting to detect regional climate change. These data have uncorrected inhomogeneities due to changes in observing time, site location, and instrumentation and no adjustment for heat island effects. However, the quality of the data was assessed for completeness, reasonableness, and accuracy before distribution. Out of the 1221 stations in the continental United States, 226 weather stations were in the designated region for the period 1980-2001.

The mean daily temperature used is the average of the daily maximum and minimum temperatures. Daily regime areas were calculated as percentages of the total area of the Great Plains based on a grid box count. Both the temperature and area data were deseasonalized by subtracting a calendar day average for the month over the 22-year period to arrive at a daily anomaly and its standard deviation. A weakness in our data analysis is that autocorrelation is not considered and not using a variance inflation factor may result in an overestimate of the confidence limit (Wilks, 2006). A linear least squares trend line was fitted to the daily data to calculate the 22-year trend. This analysis was done separately for each of the

three regimes along with an "other" category that included regime boundaries, areas above the polar vortex, and empty data cells.

Since the fluctuations of the surface temperature can be calculated directly from the station data, a Monte Carlo method was employed to determine the likelihood that the observed trends occurred by chance. A Monte Carlo simulation was first recommended to establish statistically significant in atmospheric science studies by Neumann et al. (1977) and has since become a commonly used approach in climate studies (Livezey and Chen (1983); Karl et al. (1996); Hanna et al. (1998); Karoly and Wu (2005); Serra et al. (2006)). In the IPCC, the 90% confidence interval is sometimes determined by a Monte Carlo simulation based on known error (Forster et al., 2007). The standard deviation for each of the respective datasets was used to randomly perturb the data within its one-standard-deviation band (von Storch and Zwiers, 1999). After each iteration, a trend line was fitted to the randomized data and the standard deviation was calculated for the slopes. After approximately 1000 iterations, the standard deviation of the slope converged to a single value. All uncertainty ranges presented in this paper are one sigma.

The mean temperature measured over an area can be separated into a balance between the temperatures in individual regimes and the area occupied by those regimes:

$$A_t\overline{T_t}^{\cdot} + A_m\overline{T_m}^{\cdot} + A_p\overline{T_p}^{\cdot} + A_o\overline{T_o}^{\cdot} = 1 \tag{A.1}$$

where A is the daily fractional area covered by a regime and is the average

daily temperature over a regime area divided by the total-area daily temperature in Kelvin units. The subscript t represents the tropical regime, m represents the midlatitude regime, p represents the polar regime, and o represents other. Each term corresponds to the percentage effect each regime had on the temperature of the total area. The time derivative of Equation A.1 can be used to investigate the relative effects of regime temperature and regime area on the change in regional average surface temperature:

$$A_t\frac{\partial\overline{T_t}}{\partial t}+A_m\frac{\partial\overline{T_m}}{\partial t}+A_p\frac{\partial\overline{T_p}}{\partial t}+A_o\frac{\partial\overline{T_o}}{\partial t}+\overline{T_t}\frac{\partial A_t}{\partial t}+\overline{T_m}\frac{\partial A_m}{\partial t}+\overline{T_p}\frac{\partial A_p}{\partial t}+\overline{T_o}\frac{\partial A_o}{\partial t}=0 \tag{A.2}$$

The first four terms on the left-hand side of Equation A.2 are the temperature effect terms and the last four are the area effect terms.

A.4 Results

The mean daily temperature in the Great Plains averaged over 1980-2001 was $10.9°C$. As expected the highest mean temperature was $14.1°C$ for the tropical regime followed by $8.7°C$ for the midlatitude regime and $6.5°C$ for the polar regime (see Figure A.2 panel a). The average percentage area for each regime shows that the region is dominated by the tropical regime with 44% and midlatitude regime with 37%, but only 4% in the polar regime and 15% in the "other" category (see Figure A.2 panel b).

The data show that there was a statistically significant warming in the Great

Plains over the 22-year period. The overall regional temperature trend for 1980-2001 is a rise of $0.35^\circ \pm 0.11^\circ C$. In contrast, trends in average regime temperatures showed a decrease during 1980-2001 (see Figure A.2 panel c). The tropical regime had a relatively small drop of $-0.14^\circ \pm 0.09^\circ C$ as did the midlatitude regime, which was $-0.13^\circ \pm 0.09^\circ C$ cooler, and the polar regime had a larger decrease of $-0.71^\circ \pm 0.14^\circ C$.

The percentage area occupied by each regime had a statistically significant change over the time period. The average area of the tropical regime grew by 7.4% ± 2.7% of the total region, the midlatitude regime contracted by -10.0% ± 3.0%, and the polar regime decreased by -1.37% ± 1.2% (see Figure A.2 panel d). Note that the reason these changes do not offset each other is due to the variability of the frontal boundary region, usually about 13% of the area, and the 4% rise in missing data over the time period.

Given that the area of the Great Plains is $1.86 \times 10^6 km^2$, it is estimated that the tropical regime moved northward to cover on average 1.38105 km2 more of the region during 1980-2001. Its rate of encroachment was $6.26 \times 10^4 km^2$ per decade. The subtropical jet shifted farther north on average than the polar jet so the midlatitude regime was compressed on average by $-1.86 \times 10^5 km^2$ at a rate of $-8.45 \times 10^4 km^2$ per decade. The polar regime lost a total of $2.56 \times 10^4 km^2$ at a rate of $1.16 \times 10^4 km^2$ per decade.

The trend for each of the terms in Equation 1 shows the tropical regime effect grew by 6.44% ± 0.02% over the period while the midlatitude regime effect declined by 8.64% ± 0.02% and the polar regime effect also fell by 1.13% ± 0.01% (see

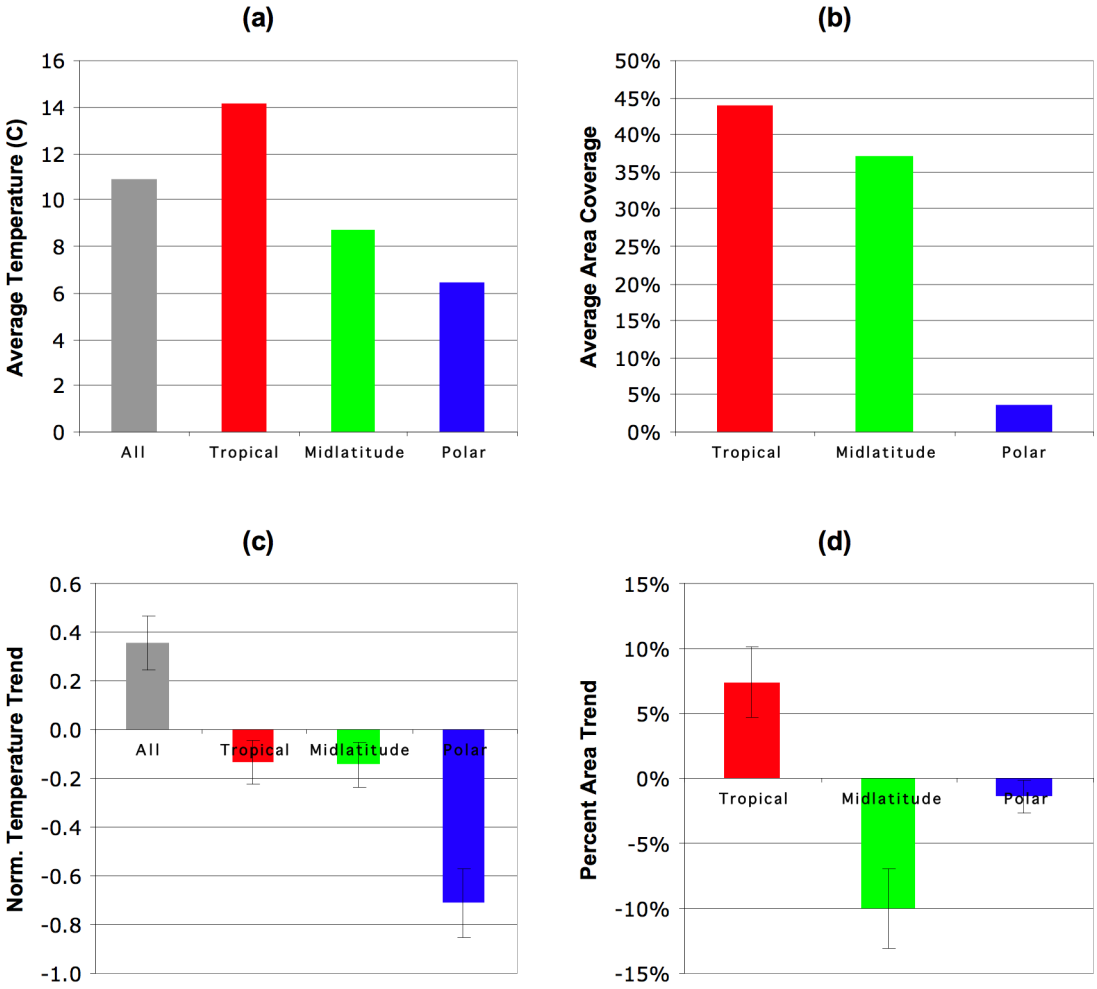

Figure A.2: Results for the Great Plains, 1980-2001 (Error bars are for one standard deviation): (a) mean temperature of the region as a whole and each regime; (b) average percentages of area occupied by the three regimes; (c) temperature trend for the region and the regimes; and (d) area trends for the regimes.

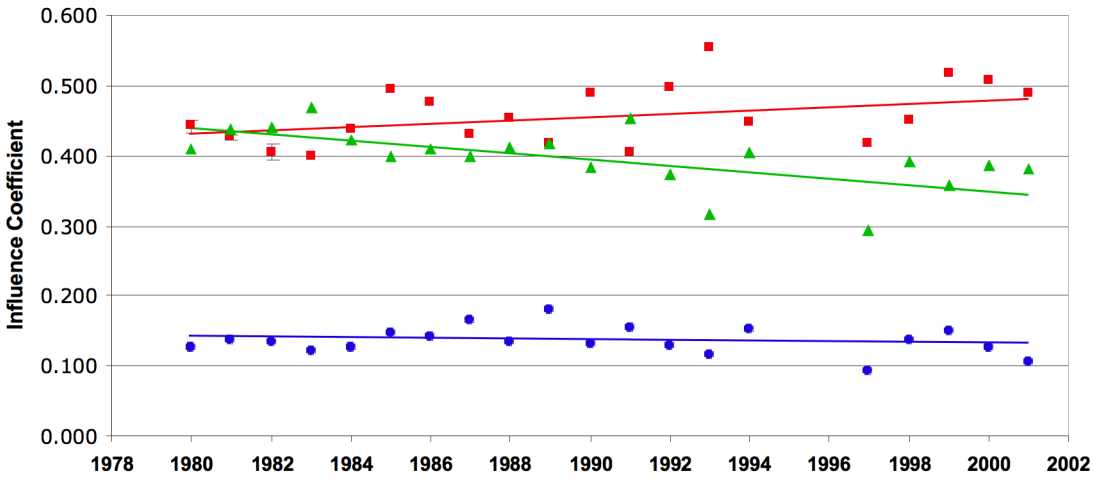

Figure A.3: The trend in effect on regional temperatures of the tropical regime (red), midlatitude regime (green), and polar regime (blue). (Annual averages were used to construct this figure while the influence trends discussed in the text were calculated on a daily basis).

Figure A.3). The results for Equation A.2 show that all the area effect terms are two orders of magnitude larger than the temperature effect terms (see Table A.2). The regional temperature is influenced most by changes in regime area, particularly in the tropical and midlatitude regimes.

A.5 Discussion and Conclusion

The finding of a $0.35°C$ rise in 1980-2001, $0.16°C$ per decade, in the Great Plains is in the same direction and similar in magnitude to the IPCC estimate that the Central United States in 1979-2005 shows a temperature increase between $0.1°-0.3°C$ per decade (Trenberth et al., 2007). The warming observed in the Great Plains is also consistent with proxy studies (Hu et al. (2005); Grundstein (2003)).

Table A.2: The regime area influence and regime temperature influence as calculated from Equation A.2. All results are $\times 10^{-5}$ and unitless.

	Tropical	Midlatitude	Polar	Other
Area influence (T*dA)	341	-451	-61	231
Temp influence (A*dT)	-5	-5	-0	-2
Sum (T*dA + A*dT)	336	-456	-61	229

The results show that average temperature increased in the U.S. Great Plains despite the temperature decrease in all three of the meteorological regimes in the region during 1980-2001. This seemingly paradoxical result can be explained by the changing area of each of the regime (see Figure A.4). As the tropical regime occupied a larger area, its warmer temperatures compared to the retreating midlatitude and polar regimes resulted in an overall average temperature increase in the Great Plains. This result is consistent with findings of the IPCC on global circulation changes (Trenberth et al., 2007).

Seidel and Randel (2007) made a similar finding that the subtropics ($28-40^{\circ}$) had one to three additional weeks in the tropical regime during recent decades in both the Northern and Southern Hemispheres. They found a maximum in tropospheric warming and stratospheric cooling in the $15^{\circ}-45^{\circ}$ latitude band in both hemispheres. There was a statistically significant correlation between poleward movement of the subtropical jet and midtropospheric temperature ($r = 0.49$).

If the regional temperature rise was due solely to the direct effect of the increased radiative forcing, one would expect regime temperatures to also rise. The

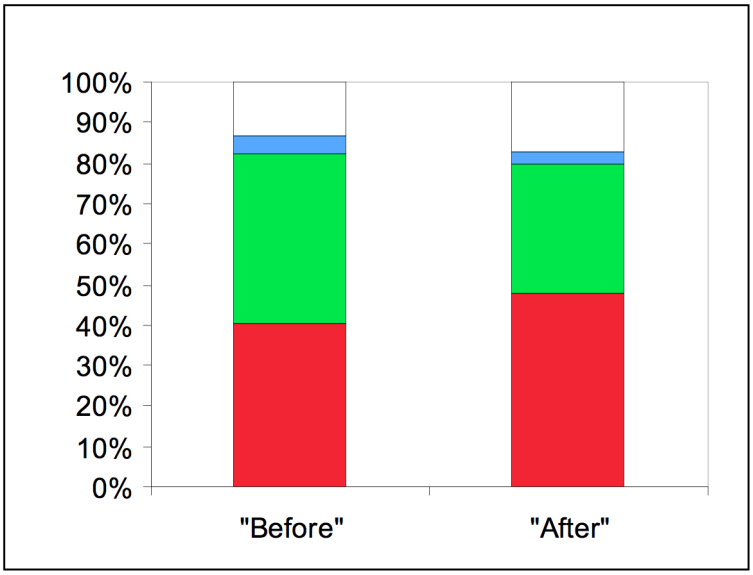

Figure A.4: Illustration of how tropical (red), midlatitude (green), and polar (blue) regime temperatures can fall but the overall temperature can rise due to changes in regime area.

finding that regime temperatures did not rise suggests that the poleward movement of the upper-tropospheric front-jet streams was responsible for the regional temperature rise. As the IPCC noted in AR4, the response to radiative forcing can be altered drastically if it affects the structure or circulation of the atmosphere (Solomon et al., 2007).

The "chicken and egg" problem of which came first, poleward front movement or rising temperature, is difficult to resolve. Warmer temperatures could cause poleward front movement by the changes in mean stationary wave patterns caused by higher temperatures (McCabe et al., 2001). Another theory is that the temperature rise is due to the movement of the front. Given that the fronts separate air masses of different temperatures, the poleward movement of the subtropical and polar fronts

is likely to extend the influence of higher tropical regime temperatures northward into areas that were dominated by the midlatitude regime in the past. It would also extend the warmer temperatures of the midlatitude regime into areas previously cooled by the polar regime. As the average latitude of the regimes moved northward, the average solar zenith angle in the individual regimes would fall, causing a slight drop in regime temperatures. Both scenarios are consistent with the results of this study.

Leroy et al. (2006) identified poleward movement of the polar jet symmetrically between the two hemispheres as the most robust indicator of climate change. One of the reasons that a poleward movement of the polar jet is observable within 7-12 years is that it has little natural variability. In contrast, surface temperature predictions are poor indicators because of the large regional uncertainty among the models. This means the relationship between poleward movement of circulation patterns and long-term temperature change provides a rich opportunity for examining regional variations and detecting regional climate change.

Detection of poleward front movement could be achieved through techniques using ozone gradients to identify the daily position of upper-tropospheric fronts and jet streams, such as the Hudson et al. (2006) algorithm used in this study. This paper demonstrates the power of this approach and its strong relationship to regional temperature. This technique also opens up the possibility of further work on the relationship of poleward movement of upper-tropospheric fronts and jet streams to other important climate variables such as precipitation patterns.

This study shows that average temperature within the meteorological regimes

in the U.S. Great Plains did not rise during 1980-2001 despite the overall average temperature increase in the region as a whole. This suggests that the poleward movement of the subtropical and polar jets was responsible for all or part of the overall temperature rise. As the tropical regime occupied a larger area, its warmer temperatures compared to the retreating midlatitude regime resulted in an overall average temperature increase in the Great Plains. Given the limitations of this study, the results observed in the Great Plains over 22 years cannot be extrapolated to other regions but poleward front movement has been observed in throughout the Northern and Southern Hemispheres (Trenberth et al., 2007). It is critical for climate scientists to better understand this phenomenon and its regional implications.

A.6 Acknowlegements

David Kuhl was supported by a Rising Star Fellowship from the National Institute for Aerospace in Hampton, Virginia. Debra Baker was supported under a National Science Foundation Graduate Research Fellowship. This research was carried out in partial fulfillment of their University of Maryland doctoral requirements. The authors would also like to thank Melanie Follette, Ning Zeng, Alfredo Ruiz-Barradas, and Eugenia Kalnay for their help and suggestions.

Appendix B

Assessing Predictability with a Local Ensemble Kalman Filter

Authors: D. Kuhl, I. Szunyogh, E. Kostelich, G. Gyarmati, D. J. Patil, M. Oczkowski, B. Hunt, E. Kalnay, E. Ott, and J. A. Yorke

Published: 2007 Journal of the Atmospheric Sciences, vol. 64, pp. 1116-1140.

B.1 Abstract

In this paper, the spatio-temporally changing nature of predictability is studied in a reduced-resolution version of the National Centers for Environmental Prediction (NCEP) Global Forecast System (GFS), a state-of-the-art numerical weather prediction model. Atmospheric predictability is assessed in the perfect-model scenario for which forecast uncertainties are entirely due to uncertainties in the estimates of the initial states. Uncertain initial conditions (analyses) are obtained by assimilating simulated noisy vertical soundings of the "true" atmospheric states with the *Local Ensemble Kalman Filter* (LEKF) data assimilation scheme. This data assimilation scheme provides an ensemble of initial conditions. The ensemble mean defines the initial condition of 5-day deterministic model forecasts, while the time-evolved members of the ensemble provide an estimate of the evolving forecast uncertainties. The observations are randomly distributed in space to ensure that the geographical distribution of the analysis and forecast errors reflect predictability limits due to

the model dynamics and are not affected by inhomogeneities of the observational coverage.

Analysis and forecast error statistics are calculated for the deterministic forecasts. It is found that short-term forecast errors tend to grow exponentially in the extratropics and linearly in the tropics. The behavior of the ensemble is explained by using the E-dimension, a spatio-temporally evolving measure of the evenness of the distribution of the variance between the principal components of the ensemble-based forecast error covariance matrix.

It is shown that in the extratropics the largest forecast errors occur for the smallest E-dimensions. Since a low value of the E-dimension guarantees that the ensemble can capture a large portion of the forecast error, the larger the forecast error, the more certain that the ensemble can fully capture the forecast error. In particular, in regions of low E-dimension, ensemble averaging is an efficient error filter and the ensemble spread provides an accurate prediction of the upper bound of the error in the ensemble mean forecast.

B.2 Introduction

In dynamical systems theory, predictability is often characterized by the largest Lyapunov exponent of the system. This characterization is based on studying the evolution of initially small perturbations to a nonlinear trajectory, assuming that a numerically-computed, sufficiently long trajectory can explore the small neighborhood of all possible states of the system (e.g., Ott 2003). Such a characterization may not apply for finite time forecasts and is especially inappropriate when the dimensionality of the dynamics is so high that exploration of the attractor by a typical trajectory takes a very long time. This is the case for a high-dimensional weather prediction model that mimics the evolution of the atmosphere.

Patil et al. (2001) introduced the E-dimension (originally called BV-dimension) to characterize the spatio-temporally changing complexity of the dynamics for a physically extended large system, such as a state-of-the art numerical weather prediction model. The E-dimension is a local, spatio-temporally evolving measure of complexity (Patil et al. 2001; Oczkowski et al. 2005). The calculation of this measure is based on the singular value decomposition of an ensemble-based estimate of the analysis (or forecast) error covariance matrix in a local region. Heuristically, the E-dimension measures the evenness of the distribution of the variance between the principal components of the ensemble-based estimate of the forecast error covariance matrix. The lowest possible value of the E-dimension, which is 1, occurs when the estimated variance is confined to a single spatial pattern of uncertainty. The highest possible value of the E-dimension, which is equal to the number of ensemble

members N, occurs when the variance is evenly distributed between N independent patterns of uncertainty.

Patil et al. (2001) applied the E-dimension diagnostic to operational forecast ensembles of the National Centers for Environmental Prediction (NCEP). They found an intriguing relationship between the regions of low E-dimensionality and the magnitude of the ensemble perturbations: the lowest-dimensional regions were often the regions of largest estimated forecast uncertainties. Patil et al. (2001) hypothesized that there was a large potential for analysis and forecast improvements in the regions of low E-dimensionality due to the simple structure of potential analysis and forecast error patterns in those area. Most importantly, this result motivated the development of the Local Ensemble Kalman Filter (Ott et al., 2004) data assimilation scheme.

While the results of Patil et al. (2001) with the NCEP forecast ensembles were encouraging, they could not be considered conclusive due to some important limitations of the ensemble used in the study. Most importantly, there were only five independent ensemble members available for the calculation. Secondly, the NCEP ensembles were initialized with the breeding algorithm (Toth and Kalnay, 1993, 1997), which tends to force the initial ensemble perturbations toward a few dominant error patterns (e.g. Szunyogh et al. 1997). These limitations of the Patil et al. (2001) study motivated Oczkowski et al. (2005) to repeat the calculations of Patil et al. (2001) with much larger ensembles. Oczkowski et al. (2005), who also employed local energetics diagnostics to identify the atmospheric dynamical processes that led to the development of local low dimensionality, confirmed the earlier result that

local low dimensionality was often the result of strong local instabilities that led to the rapid growth of simple error patterns.

The study of Oczkowski et al. (2005) was also based on a bred-vector ensemble. As mentioned earlier, the main problem with this approach is that extreme low-dimensionality tends to occur in the initial ensemble as a result of the ensemble generation technique. The main goal of the present study is to investigate the role that changes in the complexity of the local dynamics play in predictability, using an ensemble of initial perturbations that has high E-dimension and is consistent with the estimated analysis uncertainties. To achieve this goal, we take advantage of our previous work to test an implementation of the LEKF on the NCEP GFS model (citealtSzunyogh2005; SEA05 hereafter). We investigate the evolution of the E-dimension and the role it plays in predictability in forecasts started from analysis ensembles of SEA05. For a 40-member bred-vector ensemble, the typical values of the E-dimension vary between 5 and 25 (Oczkowski et al., 2005), but for a 40 member LEKF ensemble the E-dimension is never smaller than 25 and is typically larger than 30 (SEA05).

We carry out experiments for the perfect model scenario: a "true" nonlinear trajectory is generated by a long integration of the model from a realistic Northern Hemisphere winter initial condition. Then, imperfect (perturbed) initial conditions are obtained by assimilating simulated noisy observations of the "true" states with the LEKF data assimilation system. An important feature of the hypothetical observing network is that the observations are randomly distributed. Thus, unlike a real observing network, the simulated observing network may be assumed to have

no effect on the geographical distribution of the analysis and forecast uncertainties (provided that the observational network is not too sparse). Here, the focus is on the spatio-temporal evolution of the forecasts and the forecast uncertainties started from the analyses of SEA05. Although the unique features of the LEKF algorithm make the close relationship between local dimensionality, error growth, and skill of the ensemble to capture the space of forecast uncertainties especially transparent, we believe that our results could be reproduced with any suitably formulated ensemble-based Kalman filter scheme (e.g., Anderson 2001; Bishop et al. 2001; Houtekamer and Mitchell 2001; Evensen 2003; Keppenne and Rienecker 2002; Whitaker and Hamill 2002). In addition, we hope that our results help strengthen the theoretical foundation of the operational practice of using small ensembles to predict the evolution of uncertainties in high-dimensional operational numerical weather prediction models (e.g., Kalnay 2003).

The analysis-forecast system used in our experiments, as well as the experimental design, are described briefly in Section 2. Section 3 investigates the geographical distribution and typical evolution of the forecast errors. This section also provides a detailed account of a case of explosive error growth. Section 4 investigates the relationship between the E-dimension, forecast error growth, and the skill of the ensemble in tracking the space of the spatio-temporally evolving forecast uncertainties. Section 5 is a summary of our main conclusions.

B.3 Experimental design

The LEKF scheme is a model-independent algorithm to estimate the state of a large spatio-temporally chaotic system (Ott et al., 2004). The term "local" refers to an important feature of the scheme: it solves the Kalman filter equations locally in model grid space. More precisely, the state estimate at a grid point P is obtained independently from the state estimate at the other grid points, considering the observations and the background state only from a local cube centered at P. The LEKF scheme also provides an estimate of the analysis uncertainty at P and generates an ensemble of analysis perturbations that represent the estimated uncertainty at P. When the LEKF is applied to the assimilation of observations of a perfect model, we use a 4% multiplicative variance inflation (Anderson and Anderson, 1999) at each analysis step to increase the estimated analysis uncertainty to compensate for the loss of ensemble variance due to sampling errors and the effects of nonlinearities. In addition to the variance inflation coefficient, the scheme has two tunable parameters: the number of grid points in the local cube and the number of ensemble members.

Here, as well as in SEA05, the LEKF is implemented on a reduced resolution version of the 2001 operational implementation of the NCEP GFS model. With the exception of the resolution, which is reduced to T62 in the horizontal direction and to 28 levels in the vertical direction, the model we use is identical to the full operationally implemented version of the 2001 NCEP GFS (detailed documentation of the model can be found at http://www.emc.ncep.noaa.gov/modelinfo).

A time series of "true" states was generated by a 60-day integration of the model starting from the operational NCEP analysis at 0000 UTC on 1 January 2000. The two components of the horizontal wind vector and the temperature were observed at all model levels, and the associated surface pressure was also observed. The assumed observational errors were normally distributed with zero mean and standard deviations of 1 m/s, 1 K and 1 hPa, respectively. Initially, observations were generated at all 17,848 horizontal grid point locations. Then, reduced observational networks were created by gradually removing observational locations at randomly selected grid points. This approach was applied to construct three additional observational networks that take vertical soundings of the atmosphere at 2000, 1000, or 500 fixed locations every six hours.

In what follows, we investigate the subsequent evolution of the distribution of the forecast errors. Most of the results presented here are for a configuration of the LEKF that consists of a 40-member ensemble, $7 \times 7 \times v$ grid point local cubes (v is the number of vertical grid points in the cube and changes with altitude; see SEA05 for details), and 2,000 simulated vertical soundings. We note that 7 grid points is equivalent to a distance of 13.4 degrees in the meridional direction and to a distance of 13.1 degrees in the zonal direction. The initial ensemble perturbations are generated by adding random noise to the operational NCEP background forecast, truncated to the resolution used in this paper, at 0000 UTC 1 January 2000. The distribution of the random noise is identical to that of the simulated observations. That is, except for the effects of statistical fluctuations and truncation errors, the initial background is identical to the operational NCEP background at 0000 UTC

1 January 2000 and in the initial estimate of the background error covariance matrix the error variance is about the same as the observational error variance, while the errors of the different variables at the different grid point locations are uncorrelated.

B.3.1 Data sets

A state estimate is obtained every six hours by assimilating the simulated observations with the LEKF scheme. Deterministic forecasts are started from the 0000 UTC, 0600 UTC, 1200 UTC, and 1800 UTC ensemble mean analyses each day. An ensemble of forecasts is also started every 12 hours, using the analysis ensemble provided by the LEKF as the initial conditions. Forecast error statistics are generated by comparing the deterministic forecasts to the true states. (The only exceptions are the results presented in section 4.3, where the ensemble mean forecast is compared to the true states.) The forecast error statistics are computed for the 40-day period that starts at the fifteenth day along the "true" trajectory. We refer to time using the 40-day period as reference, i.e., the first forecast that we verify starts at 0000 UTC on day 1, and the last forecast we verify starts at 1200 UTC on day 40. The model outputs are processed on a 2.5×2.5 degree resolution grid. We present error statistics in the following formats:

- Snapshots of errors are presented by mapping the difference between the forecast and the true state on the grid.

- Maps of the time mean absolute error are generated by first computing the absolute value of the difference between the forecasts and the true states at

the grid points, then computing the 40-day mean of the absolute values.

- The error for a geographical region is obtained by computing the root-mean-square of the error over all grid points in the geographical region. Plots showing time series of the errors are based on this information. Errors are shown for three geographical regions: NH extratropics ($30°N - 90°N$), tropics ($30°S - 30°N$) and SH extratropics ($90°S - 30°S$).

- The spectrally-filtered errors for a geographical region are obtained by first spectrally filtering the grid point values along each latitude, based on the zonal wave numbers, then computing the rms over the region.

- The time-mean absolute error for a geographical region is obtained by computing the 40-day mean of the root-mean square error for the given geographical region.

B.4 Evolution of the forecast errors

The simulations in SEA05 found that the largest wind and temperature analysis errors were in the main regions of deep convection in the tropics, while the smallest analysis errors were found in the mid-latitude storm track regions. Figure B.1 illustrates the rapid change in the geographical distribution of the errors as the forecasts progress, showing the time mean of the forecast errors for the meridional component of the wind vector at the 500 hPa level (the figure shows the time mean over all 160 forecast cycles). There seems to be a relationship between the

errors in the region of deep convection and the early amplification of the errors in the North Pacific storm track region. Then the errors propagate westward along the upper tropospheric waveguides. Although a clear indication of rapidly growing errors in the North Atlantic and Southern Hemisphere storm track regions can be seen first at the 48-hour forecast lead time, the storm track regions become the location of the dominant error patterns in the extratropics by the 72-hour forecast lead time.

B.4.1 Dependence on the geographical region

The difference between the error growth characteristics in the extratropics and the tropics becomes obvious by investigating the time evolution of the root-mean-square forecast errors for the different geographical regions (shown by closed squares in Figure B.2 and B.3). The most striking difference between the extratropics and the tropics is in the functional dependence of the error growth on the forecast lead time. (Notice that while the vertical scale in Figure B.2 is logarithmic, the vertical scale in Figure B.3 is linear.) In the extratropics, the root-mean-square of the forecast error is approximately an exponential function of the forecast lead time for the first 72 hours, i.e., $z_f(t) = z_a e^{rt}$, where the scalar r denotes the *exponential* error growth rate. After about 72 hours, the error growth starts slowing down, indicating an initial stage of nonlinear error saturation. In contrast, in the tropics, the root mean square of the forecast error, $z_f(t)$, is a linear function of the forecast lead time, i.e., $z_f(t) = bt + z_a$, where $z_a \approx z_f(0)$ is the root-mean-square analysis error and the

scalar b is the *linear* error growth rate.

We obtain estimates of the parameters z_a and r by calculating their values for the curves that best fit the forecast errors for the first 72 hours in the least-squares sense. Although the initial errors are very slightly larger in the SH extra-tropics (not shown) than in the NH extra-tropics (0.42 ms^{-1} versus 0.39 ms^{-1}), the forecast errors grow a bit more slowly in the SH (not shown) than in the NH extra-tropics; the error doubling time $T = r^{-1} \ln 2$ is 38.5 hours in the SH extratropics versus 34.7 hours in the NH extratropics.

The shape of the error growth curves indicates that the magnitude of the errors in the first 72 hours is governed by the differential equation

$$dz_f(t)/dt = rz_f(t), \qquad z_f(0) = z_a, \tag{B.1}$$

in the extratropics and by the differential equation

$$dz_f(t)/dt = b, \qquad z_f(0) = z_a \tag{B.2}$$

in the tropics.

Interestingly, the functional dependence of the error growth is independent of the spatial scale in both regions: except for the zonal mean term ($k = 0$), the initial error grows exponentially for all wave number ranges in the extratropics (Figure B.2), while the error grows linearly for all wave number ranges in the tropics (Figure B.3). The linear error growth rate b and the initial exponential growth rate r are larger for the wave number ranges $k = 1$–10 and $k = 11$–20 than for the range $k = 21$–40. Also,the errors tend to start saturating earlier for the smaller scales (larger wave numbers).

B.4.2 Dependence on the LEKF parameters

We have carried out experiments to test the sensitivity of the forecast results to the free parameters of the analysis scheme (results are not shown). We find that, within a reasonable range of the parameters, the forecast errors depend only weakly on the parameters. More precisely, the small initial differences between the analyses for $5\times5\times v$, $7\times7\times v$, and $9\times9\times v$ local cubes show negligible growth in the forecast phase. Likewise, for a $5 \times 5 \times v$ local region size, the advantage of the 80-member ensemble filter over the 40-member ensemble filter is negligible in the first 72 hours. Since the dominant errors grow exponentially in the extra-tropics, our result shows that differences in the analysis due to changes of the free parameters have only a very small projection on the dominant instabilities. This indicates that, when the parameters of the LEKF scheme are chosen from a reasonable range, the scheme can efficiently remove the growing error components. This is a nontrivial result, since the scheme corrects errors that were growing before the analysis time, while the forecast errors are governed by errors that are growing after the analysis time. An important practical consequence of the weak sensitivity to the tunable parameters is that it greatly increases the generality of our predictability assessment.

B.4.3 Dependence on the number of observations

In sharp contrast to the aforementioned weak sensitivity to the tunable parameters, the observational density has a significant influence on the accuracy of the forecasts. Increasing the number of observations substantially improves the accuracy

of the forecasts in all geographical regions (results are not shown).

In the tropics, the improvement is essentially constant in time, due to a weak dependence of the linear error growth rate on the number of observations. This result suggests that increasing the number of observations in the tropics leads to a reduction of the magnitude of the forecast errors, but it does not change the characteristics of error growth. Likewise in the extra-tropics, the influence of the observational density on the exponential error growth rate is modest, although the error growth is slightly faster for the higher observational density (Table B.1).

B.4.4 Temporal variability of the forecast errors

Among the three geographical regions considered in this paper, the temporal variability of the forecast errors is highest in the NH extra-tropics and lowest in the tropics (Figure B.4). The high variability in the NH extratropics is due to episodes of unusually large forecast errors. The first such episode is a pattern of extremely large errors in forecasts started between 1200 UTC on day 4 and 0000 UTC on day 7. We find (results not shown) that improving the accuracy of the analysis, by adding more observations and/or increasing the ensemble size, leads to minuscule reductions in the forecast errors at these verification times. This indicates that the unusually large forecast errors in this case are more associated with low predictability of the atmospheric states than with the accuracy of the analyses. An inspection of the atmospheric flow regimes reveals that the relatively low predictability of these states is associated with the rapid amplification of errors in the presence of an unusually

strong jet stream in the North Atlantic storm track region (further details on this event are provided in sections B.4.5 and B.5.2).

The second episode involves a pattern of unusually large analysis errors between about day 16 and day 24, which lead to a proportionally elevated level of forecast errors at the associated verification times. An inspection of the spatio-temporal evolution of the errors for this period (not shown) reveals that the relatively large errors are due to exceptionally large analysis error in the region of Indonesia that later propagate into the NH extra-tropics. The visible propagation of the time-mean forecast errors from the tropics to the extratropics shown in Figure B.1 is associated with this episode.

B.4.5 A case of explosive error growth

To gain a better understanding of the processes that lead to the explosive error growth in the aforementioned first episode, we select the forecast started at 1200 UTC on day 6 for further inspection. Maps of the forecast errors show that the explosive error growth at the 36-hour lead time occurs in a very localized region off the coast of Newfoundland (Figure B.5).

For the next 24 hours, the dominant error pattern is characterized by an eastward-propagating, rapidly-amplifying dipole structure. This structure and the fast propagation speed indicate that the dominant error pattern takes the shape of a packet of synoptic-scale Rossby waves. This conclusion can be confirmed by calculating the packet envelope of the forecast errors for the 4- to 9-wavenumber

range with a Hilbert transform-based method Zimin et al. (2003) and Zimin et al. (2006). Using the technique of Zimin et al. (2006), Figure B.6 depicts an amplifying eastward-extending envelope of errors. An inspection of the vertical cross-section of the errors (not shown) also confirms that the error growth starts in the jet layer with an overestimation of the wind speed in the core of the jet and a small distortion of the upper tropospheric wave near the core of the jet. Although downstream development (an initial divergence of the ageostrophic fluxes that triggers a baroclinic energy conversion; see Orlanski and Chang (1993) and Orlanski and Sheldon (1995) leads to the development of a closed low associated with the upper tropospheric wave, the largest forecast errors occur further downstream, near the leading edge of the wave packet shown in Figure B.6. Such propagation of the dominant errors was documented and analyzed in detail in Persson (2000), Szunyogh et al. (2000), Szunyogh et al. (2002), Zimin et al. (2003) and Hakim (2005) and was foreseen long ago by the pioneers of numerical weather prediction (Rossby 1949; Charney 1949; Phillips 1990).

In our example of rapid error growth, the atmospheric instability that drives the propagation of the errors is a growing uncertainty in the characteristics (phase and amplitude) of finite amplitude waves generated by an earlier downstream baroclinic development. (Here the term "instability" is used in the mathematical sense, i.e., it refers to a growing uncertainty in the solution due to an uncertainty in the initial condition.) The potential importance of an instability process, in which an earlier baroclinic or barotropic instability leads to uncertainties in the characteristics of the developing finite-amplitude waves, was first pointed out by Snyder (1999).

That the dominant errors propagate along the upper tropospheric wave guides (Figure B.1 and related discussion earlier) suggests that this may be the most important instability in the model solutions (forecasts). The importance of this instability process, in which temporal evolution and spatial propagation play equally important roles, reinforces our view that the atmosphere should always be approached as a spatio-temporally chaotic system.

B.5 The role of local dimensionality

SEA05 found that the efficiency of the LEKF algorithm was inversely proportional to the E-dimension. More precisely, a strong negative correlation was found between the grid-point values of the time mean E-dimension and the grid-point values of the time mean of the explained variance. The explained variance measures the portion of the error that is captured by the ensemble. In what follows, we investigate the relationship between E-dimension, explained variance and the magnitude of forecast errors.

B.5.1 E-dimension, explained variance and forecast error

While the choice of the coordinates of the state vector does not affect the state estimates, it has a profound effect on the singular value decomposition (SVD) of the error covariance matrices. Thus, the choice of coordinates has an important effect on such SVD-based diagnostics as the E-dimension. We follow the strategy of Oczkowski et al. (2005) and transform the ensemble perturbations so that the

square of the euclidean norm of the transformed perturbations has dimensions of energy. The local state vector is defined by all grid point variables in a local volume that contains a 5×5 horizontal grid (at 2.5-degree resolution in both direction) and the entire model atmosphere in the vertical direction.

This definition of the local state vector differs from that used for the calculation of the E-dimension in SEA05. There, the local volume was defined by the local volume used in the LEKF algorithm, in which only a few model levels were included in the vertical direction and the number of model levels in the vertical layers was height dependent. The rationale for this change is that in SEA05, the goal was to evaluate the assumptions made in the implementation of the LEKF on the NCEP GFS; here, the goal is to study the role of local dimensionality in shaping the local predictability.

As expected based on the results of SEA05, the E-dimension is typically higher in the tropics (Figure B.7) than in the extra-tropics for the entire 5-day forecast range. While the E-dimension decreases with increasing forecast time over the entire globe, the decrease of the dimension is much faster in the storm track regions than elsewhere. One may wonder whether this effect is associated with an inherent property of the model dynamics or arises from an unexpected collapse of the ensemble due to some unforeseen problem with the ensemble generation technique. To answer this question, we apply the explained-variance diagnostic (see SEA05) to the forecast error and the forecast ensemble. The explained variance diagnostic measures the portion of the forecast error that lies in the space spanned by the evolving ensemble perturbations. (Formally, it is calculated by projecting the forecast error

on the space of the ensemble, then taking the square of the projection, which is finally normalized by the square of the forecast error to obtain the measure). In the extreme cases, when the ensemble perfectly captures the space in which the forecast error evolves, the explained variance is one, and when the forecast error falls entirely outside of the ensemble space, the explained variance is zero. The close relationship between the typical regions of low dimensionality and the typical regions of high explained variance can be deduced subjectively by comparing Figures B.7 and B.8. This observation motivates us to assess the relationship between the two quantities in a more quantitative way. In addition, we would like to know whether such a strong relationship exists only for the temporal means of the two quantities or whether one is also present for the spatio-temporally evolving fields. To achieve these two objectives, we study the joint probability distribution of the E-dimension and the explained variance in the NH extratropics (Figure B.9) and the tropics (Figure B.10). (The joint probability distribution for the SH extratropics is similar to that for the NH extratropics, thus it is not shown.)

The joint probability distribution function is obtained by counting the number of cases when a pair of values for the E-dimension and the explained variance falls into a bin defined by a small interval ΔE of the E-dimension and a small interval ΔEV of the explained variance. Then the number of cases is normalized by $\Delta E \times \Delta EV \times n$ and the bin is color shaded based on the result. The total sample size n is equal to the total number of grid points in the given geographical region times the the number of verification times, 160, on which the sample is based. This normalization ensures that the integral of the plotted values over all bins is equal

to one.

The most important common feature of the joint probability for the NH extratropics and tropics is that the smaller the E-dimension, the larger the possible smallest value of the explained variance. In other words, the lower the E-dimension, the higher the confidence we can have that the ensemble captures the actual forecast error. In addition, as the forecast time increases, the lowest possible value of the E-dimension decreases, and the lowest values of the E-dimension become an increasingly sharper predictor of a high explained variance. We also note that the boundary between the NH extratropics and the tropics is not sharp: when the two figures are merged (not shown) there is no visible jump in the probability distribution, since the high E-dimension end of the distribution for the NH extratropics and the low E-dimension end of the distribution for the tropics is populated by values from the transient region between the two areas.

What makes the close relationship between low E-dimension and high explained variance potentially valuable from a forecasting point of view in the extratropics is that fast error growth always leads to low E-dimension. (We note that the opposite is not true, the forecast error can be small for a case of low E-dimension at any forecast time.) That is, we can have the highest confidence in the ability of the ensemble to predict the space of possible errors, when the errors are the largest. This property of the ensemble is illustrated by Figures B.11 and B.12. Figure B.11 shows the joint probability distribution for the analysis and forecast errors and the explained variance in the NH extratropics. It can be seen, that as the forecast lead time increases, the ensemble captures an increasingly larger portion of the forecast

errors for the cases of large errors. This can be explained by the fact that the fast error growth always leads to low E-dimension, that is, to high explained variance (Figure B.12).

The picture is very different for the tropics (Figures B.13 and B.14). In this region, the magnitude of the forecast error is more directly related to the magnitude of the analysis error due to the linear nature of the error growth. Since the analysis errors are smaller for the lower E-dimensions, the forecast errors are also small for the low E-dimensions. (We can start seeing a shift of the larger errors toward the smaller E-dimensions only after 72 hours.) Thus the highest explained variance occurs for relatively small errors.

B.5.2 Local low dimensionality and explosive local error growth

So far we have shown that there is a close statistical relationship between E-dimension, explained variance, and forecast error. Here we illustrate this close relationship using the example of the explosive forecast error growth described in Section B.4.5. In this case, the overlap between the regions of large errors and low dimensionality is almost perfect (figure B.15), especially at and after the 36-hour forecast lead time. Likewise, the explained variance rapidly grows in the regions of rapidly decreasing dimensionality, where the explained variance exceeds 90 percent at and beyond the 24-hour forecast lead time (figure B.16).

B.5.3 Local low dimensionality and the spread-skill relationship

It has been long thought that the spread (the second moment) of a suitably-prepared ensemble forecast can be used as a predictor of the skill of the ensemble-mean forecast (Leith 1974). It has also been observed, however, that the positive correlation between the spread and the forecast error is disappointingly small; even in the perfect-model scenario, the correlation was found to be less than 0.5 (Barker 1991). The theoretical explanation for this result was provided by Houtekamer (1993) and Whitaker and Loughe (1998) using a simple stochastic model of the spread-skill relationship: a large correlation can be expected only when the temporal variability of the forecast (or analysis) error is large. This rule explains the behavior of the spread-skill relationship for the LEKF system shown in Figure 17: (i) initially the correlation increases due to the increasing variability of the forecast errors as the forecast time increases (see Figure B.4); (ii) the correlation peaks at a level slightly below 0.5 at the 72-hour forecast lead time in all three geographical regions; (iii) the maximum value of the correlation is the largest in the NH extratropics, the region where variability of the forecast errors is the largest. The low initial correlation can be explained by the fact that an ensemble-based data assimilation system, such as the LEKF, is designed to remove that part of the analysis error that is successfully captured by the ensemble. The only surprising feature in Figure 17 is the relatively high initial correlation in the tropics. The only plausible explanation for this is that in the tropics, the *location* of the dominant analysis errors is better captured by the ensemble than the *structure* of the errors. This result reinforces

our earlier conjecture, drawn in section 3.3, that the assimilation of observations in the tropics reduces the magnitude of the errors in the state estimation but does not change drastically the structure of the errors. This indicates that there is no strong relationship between errors at the different grid points in the tropics.

The joint probability distribution function for the ensemble spread and the error in the ensemble-mean forecasts is shown in Figure 18. This figure indicates that the ensemble spread is typically smaller than the error in the ensemble mean. This finding is not unexpected, since as was shown earlier (e.g., Figure B.8), part of the forecast error is not captured by the ensemble. (For short forecast lead times, the ensemble-mean forecast and the forecast started from the analysis mean are nearly identical due to the nearly linear initial evolution of the ensemble perturbations.) In addition, the ensemble spread predicts the upper bound of the error most reliably at locations where the E-dimension is the smallest (Figure 19). In contrast to the case of the single deterministic forecast, where the largest errors occur for the smallest E-dimensions, the errors in the ensemble-mean forecast are relatively small in the regions of the smallest E-dimensions. This is due to the efficient error-filtering effects of ensemble averaging in regions where the ensemble efficiently captures the space of uncertainties, i.e., in regions of high explained variance.

B.6 Conclusions

In this paper, we assess atmospheric predictability with the help of a state-of-the-art numerical weather prediction model (at a reduced resolution) and the Local

Ensemble Kalman Filter data assimilation scheme. Our experimental design addresses the issue of determining the degree to which uncertainty in the knowledge of the initial state influences the predictability of a high-dimensional, spatio-temporally chaotic system. We assume that the numerical model provides a perfect representation of the true atmospheric dynamics. Our main findings are as follows:

- For this specific choice of the model and data assimilation system, the forecast errors grow exponentially in the extra-tropics and linearly in the tropics. As exponential growth has been found in many previous studies that considered different types of uncertainties in the knowledge of the true initial conditions, the dominance of exponentially-growing features seems to be an important property of predictability in the extra-tropics. Our earlier research indicates that these dominant instabilities are closely related to the synoptic-scale local generation and propagation of the eddy kinetic energy. Since these processes can be well-simulated by the models, there are good reasons to believe that exponentially-growing instabilities dominate real atmospheric dynamics in the extra-tropics. The linear growth of errors in the tropics is a more unique result of our experiments. While this result may be an artifact of the model dynamics, which rely heavily on parameterized physical processes in the tropics, we tend to believe that the real atmosphere behaves similarly.

- The explained variance is always highest for the lowest E-dimension, independently of the geographical region and the forecast lead times. (As was shown in SEA05, this guarantees that the analysis errors are the smallest for the

smallest E-dimension independently of the geographical region)

- In the extratropics, large forecast errors gradually become more likely to occur in regions of low E-dimension as the forecast time increases. Thus, the ensemble gradually becomes more likely to capture a large portion of the forecast error as the forecast time increases. The larger the forecast error, the larger the portion of the forecast error that the ensemble captures with high certainty.

- Since the ensemble captures a larger portion of the forecast error with high certainty in the regions of low E-dimension, in those regions ensemble averaging becomes an efficient error filter and the ensemble spread provides an accurate prediction of the upper bound of the error in the ensemble mean forecast.

- In the tropics, due to the linear error growth, the magnitude of the forecast error is closely tied to the magnitude of the analysis error. Since the analysis errors are small for the smallest E-dimensions, the forecast errors are also small for the smallest E-dimensions. In our experiments, this pattern starts breaking up beyond a forecast lead time of 72 hours.

Do these results have any practical use when the forecast model is not perfect? First of all, it is safe to assume that the local dimensionality of the true atmosphere is higher than in our global forecast model. This would degrade the ability of the model-based ensemble to capture the space of forecast uncertainties. We note that, in principle, the LEKF algorithm could be used to estimate the effect of forecast errors on the E-dimension. The extension of the LEKF algorithm described in Baek

et al. (2006) provides an estimate of the model errors in addition to the estimate of the state. More precisely, it provides an estimate of the augmented state, where the state is augmented by the parameters that describe the model errors. The E-dimension could be determined by using the augmented state to define the local background covariance matrix. It is yet to be seen, however, whether the model errors can be efficiently parameterized for a complex weather prediction model, such as the NCEP GFS.

Local low dimensionality is a property that eventually breaks down with increasing forecast lead time. Eventually, predictability is completely lost, and the predictive value of the ensemble becomes the same as that of a set of randomly-drawn samples from the much larger set of climatologically realizable states of the model. The larger the magnitude of the initial ensemble perturbations, the earlier the breakdown of local low dimensionality occurs. For instance, Oczkowski et al. (2005) observed such breakdowns at forecast lead times of as little as 24 to 48 hours when investigating the evolution of a set of bred vectors. In our experimental design, the magnitude of the analysis uncertainty is small (presumably an order of magnitude smaller than in an operational weather analysis), so our results are not affected by an overall breakdown of local low dimensionality in the first 120 hours of model integration. Our plan is to investigate the process of the breakdown of low dimensionality in a future paper for both simulated and real observations.

B.7 Acknowledgments

The authors would like to thank one of the anonymous reviewers for insightful comments. D. K. was supported by a Rising Star Fellowship from the National Institute for Aerospace, Hampton, Virginia. This work was also supported by a National Oceanic and Atmospheric Administration THORPEX grant, by the Army Research Office, by a James S. McDonnell 21st Century Research Award, by the NPOESS Integrated Program Office (IPO), by the Office of Naval Research (Physics), and by the National Science Foundation (Grants #0104087 and PHYS 0098632). E.J. K. gratefully acknowledges support from the National Science Foundation (Grant DMS-0408102).

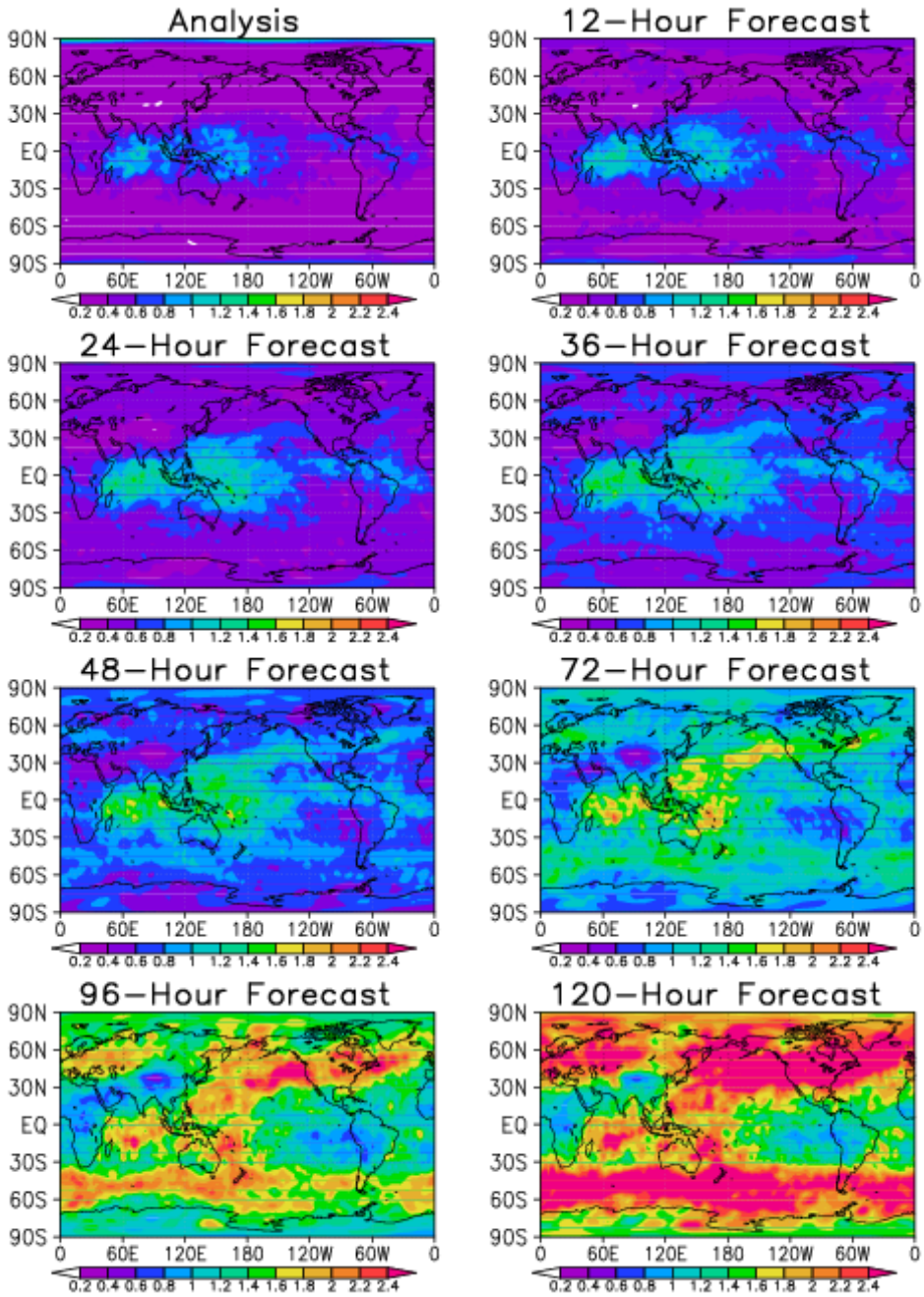

Figure B.1: Time-mean absolute error in forecasts of the meridional wind component at the 500 hPa pressure level at different forecast lead times.

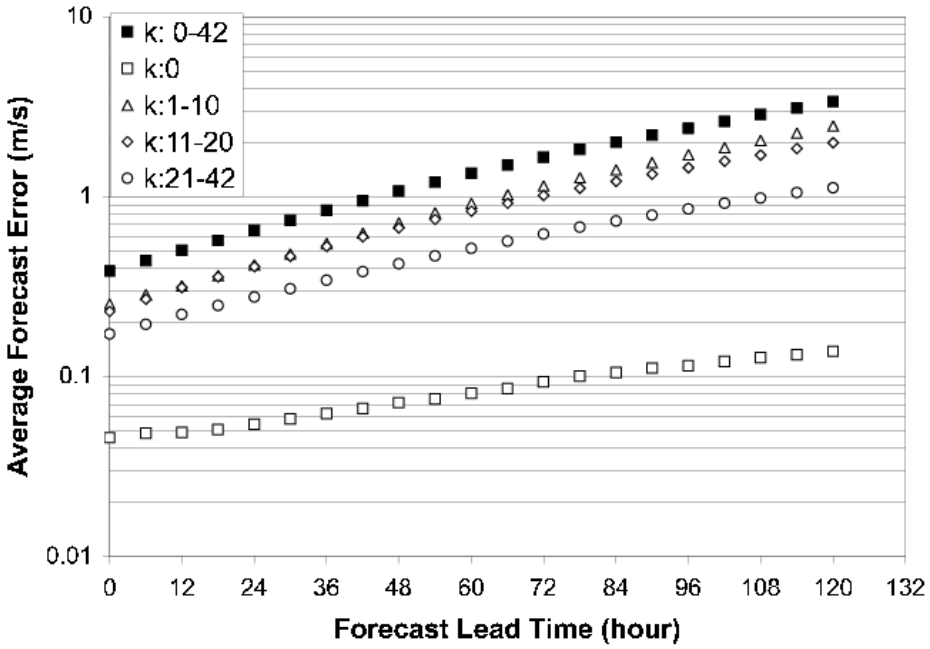

Figure B.2: Dependence of the time mean forecast error on the forecast lead time for the meridional wind component at the 500 hPa level in the NH extratropics. The evolution of the forecast error is shown for different ranges of the zonal wavenumber k.

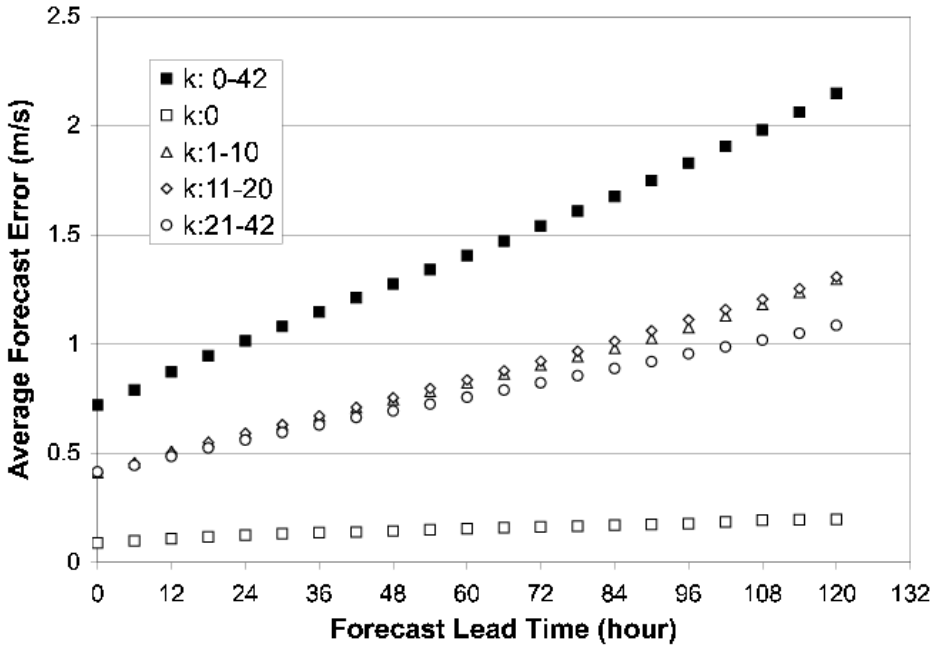

Figure B.3: Dependence of the time mean forecast error on the forecast lead time for the meridional wind component at the 500 hPa level in the tropics. The evolution of the forecast error is shown for different ranges of the zonal wavenumber k.

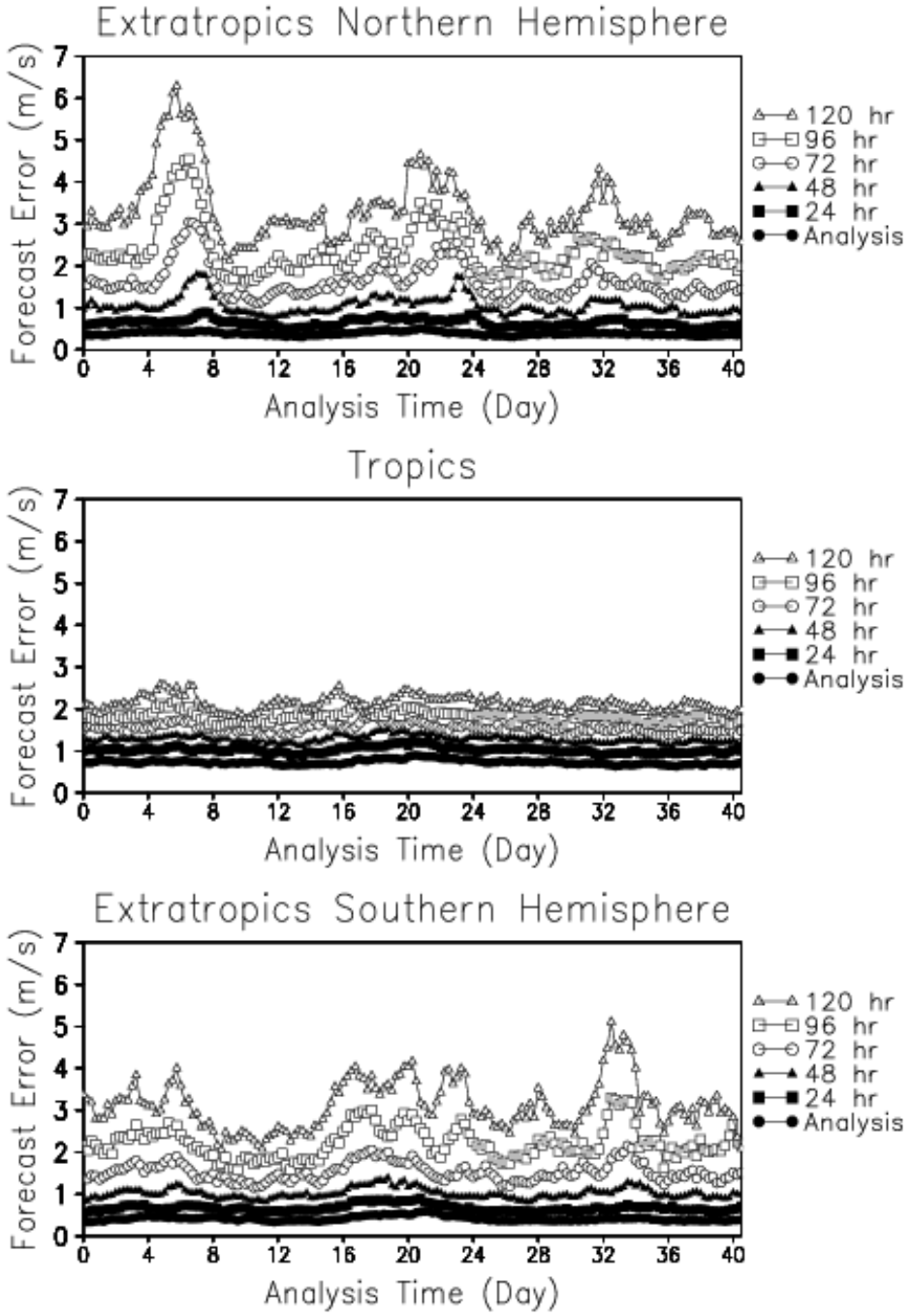

Figure B.4: Time series of the root-mean-square forecast error for different forecast lead times. Shown is the forecast error for the meridional wind component at the 500 hPa level.

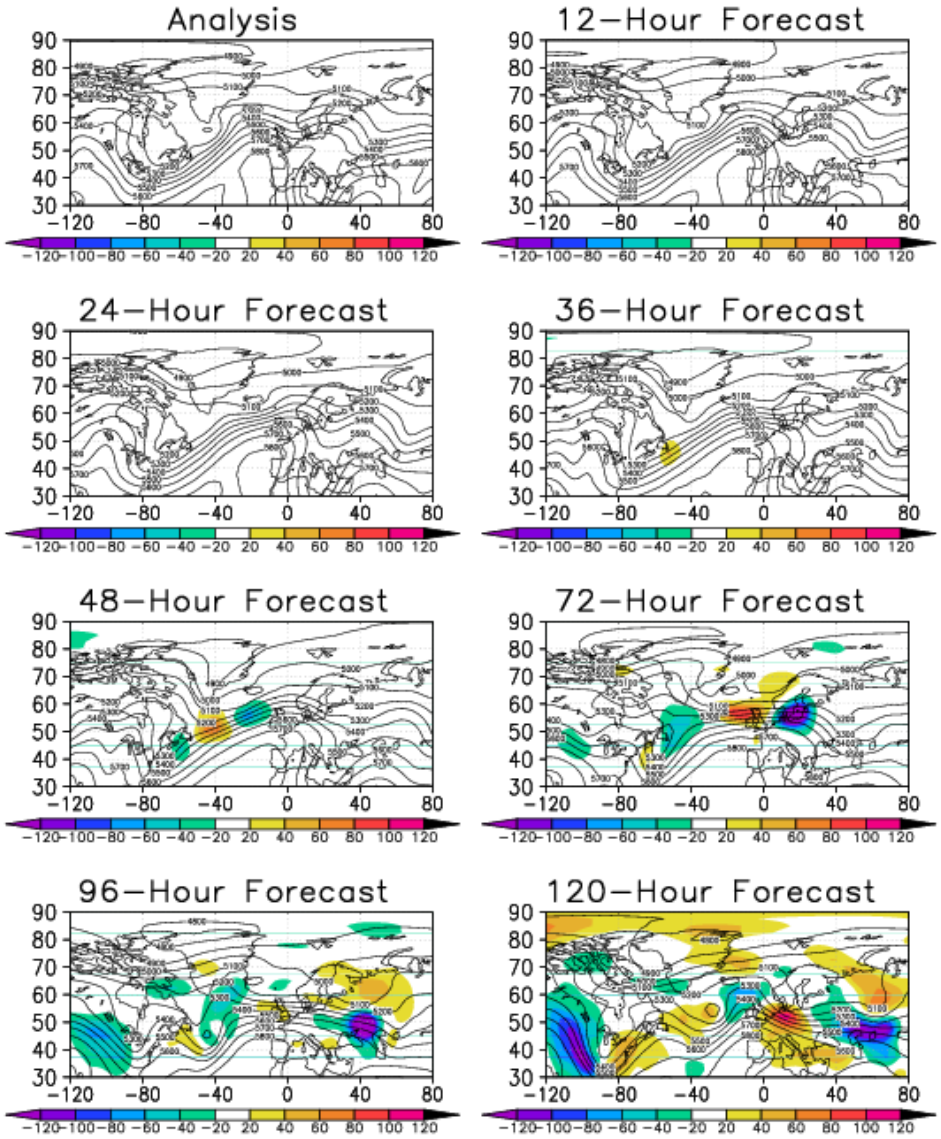

Figure B.5: Time evolution of the errors in the forecast started at1200 UTC on day 7. Shown are the errors (color shades) and the "true" state of the geopotential height of the 500-hPa pressure level.

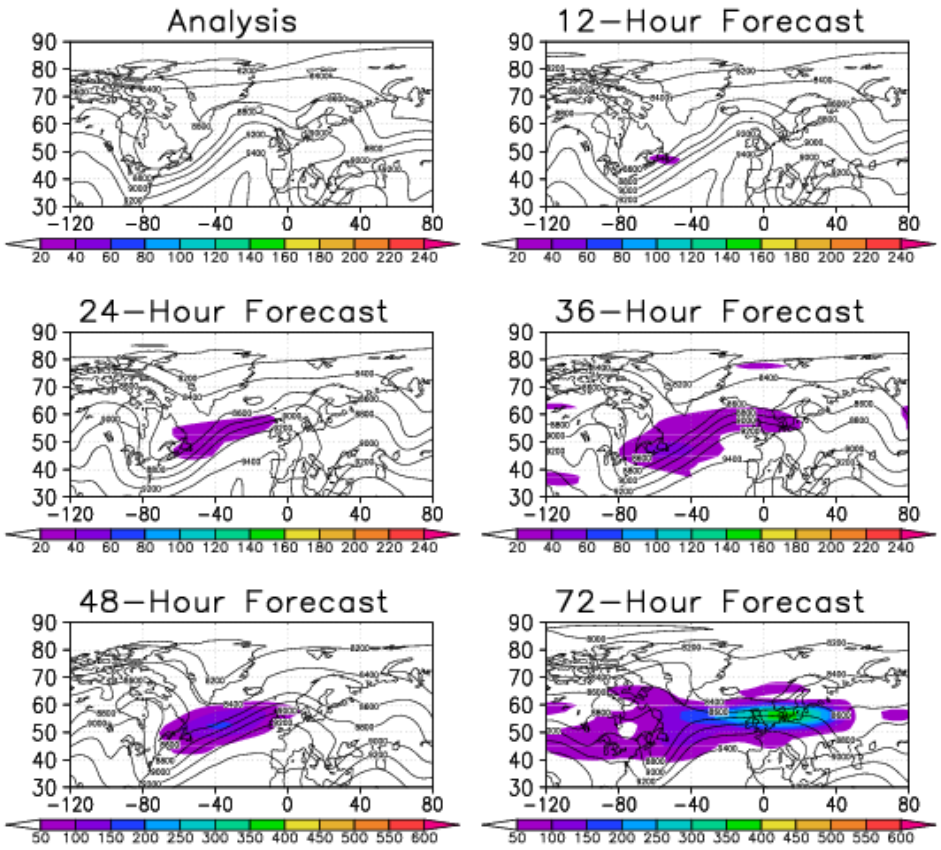

Figure B.6: Time evolution of the wave packet envelope of errors in the forecast started at 1200 UTC on day 6. The wave packet envelope is calculated based on errors in the prediction of the meridional component of the wind vector in the zonal wavenumber range from 4 to 9. Notice the change in the color scheme between the 36-hour and 48-hour forecast lead times.

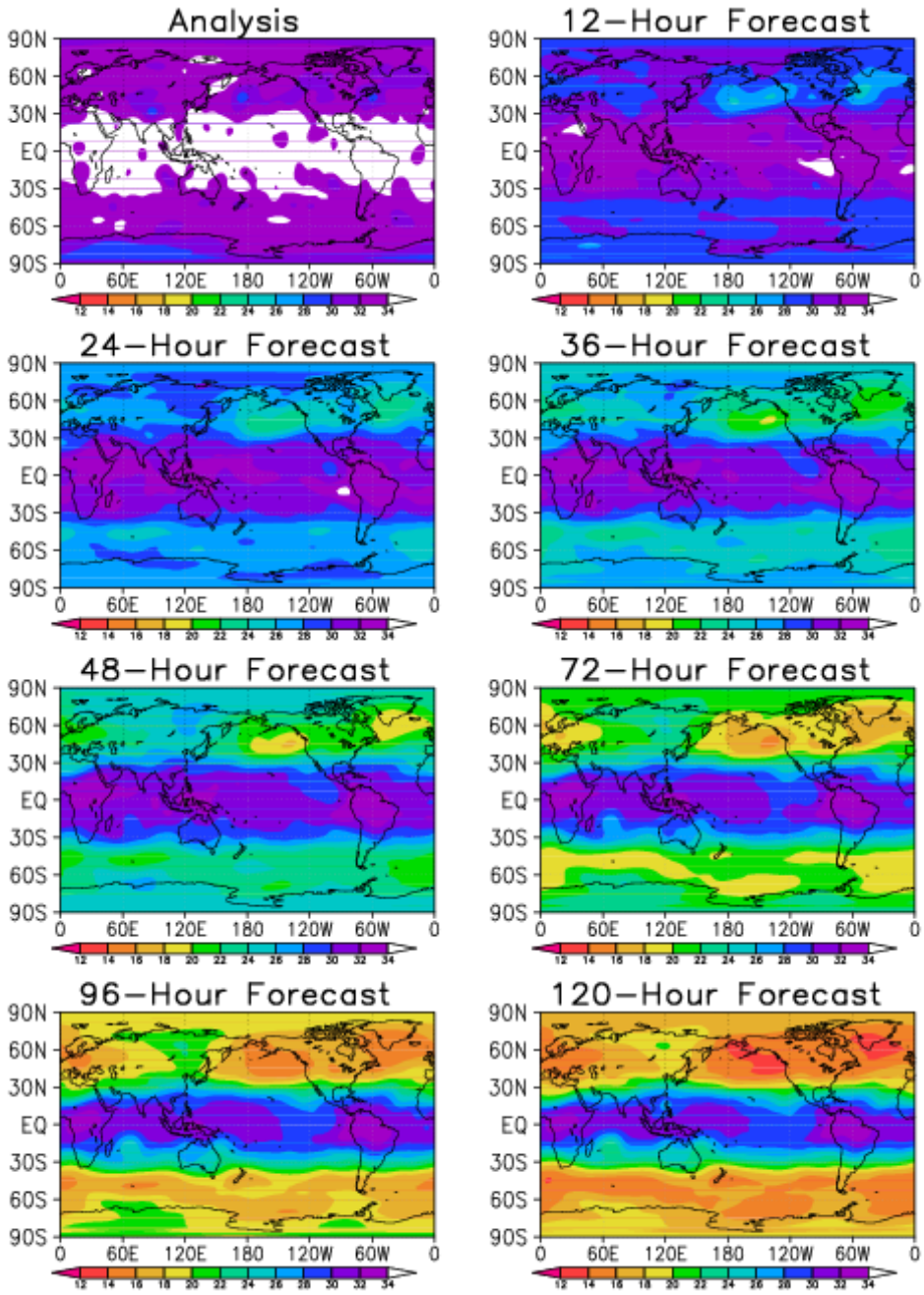

Figure B.7: Time mean E-dimension at different forecast lead times.

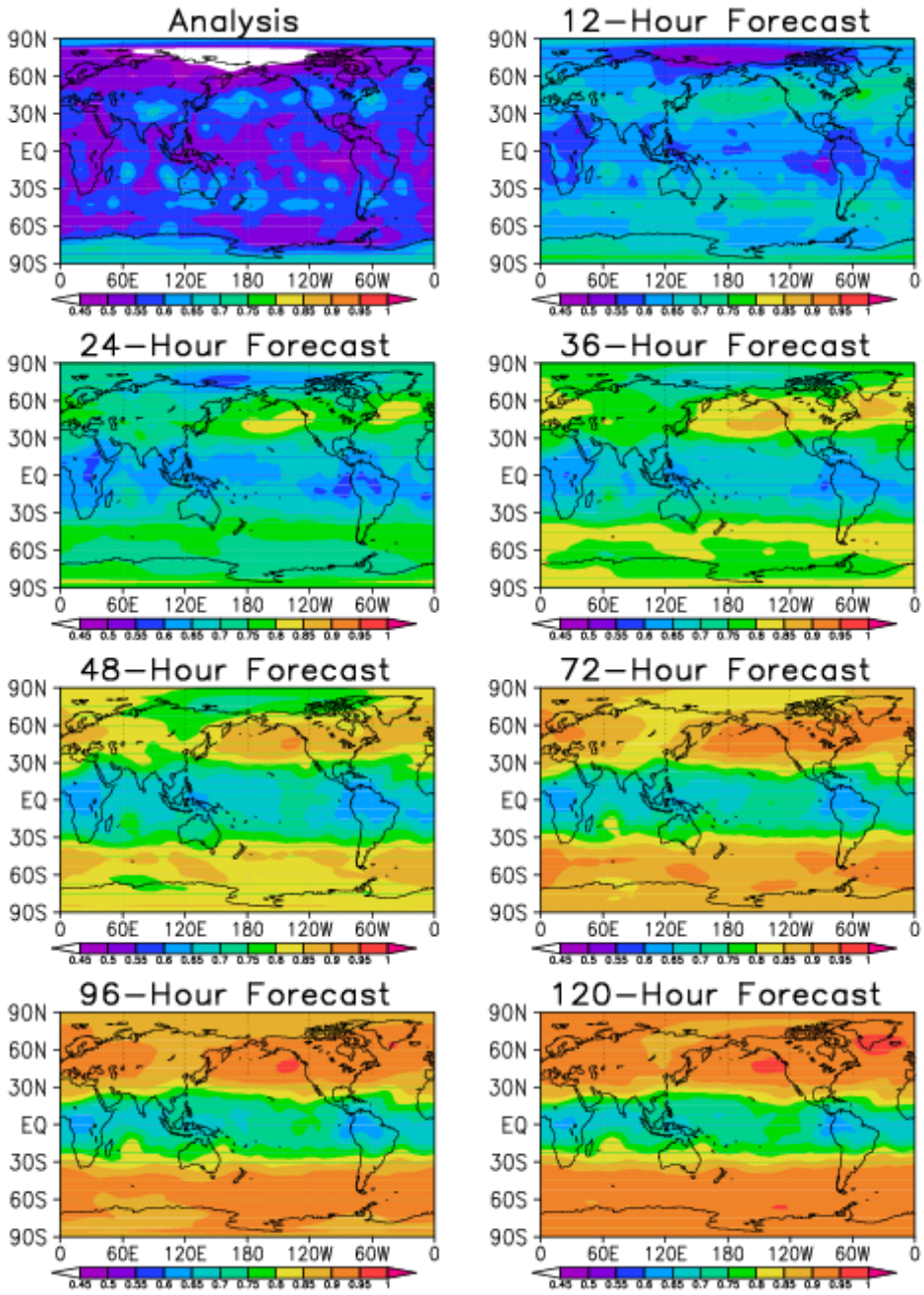

Figure B.8: Time mean explained variance at different forecast lead times.

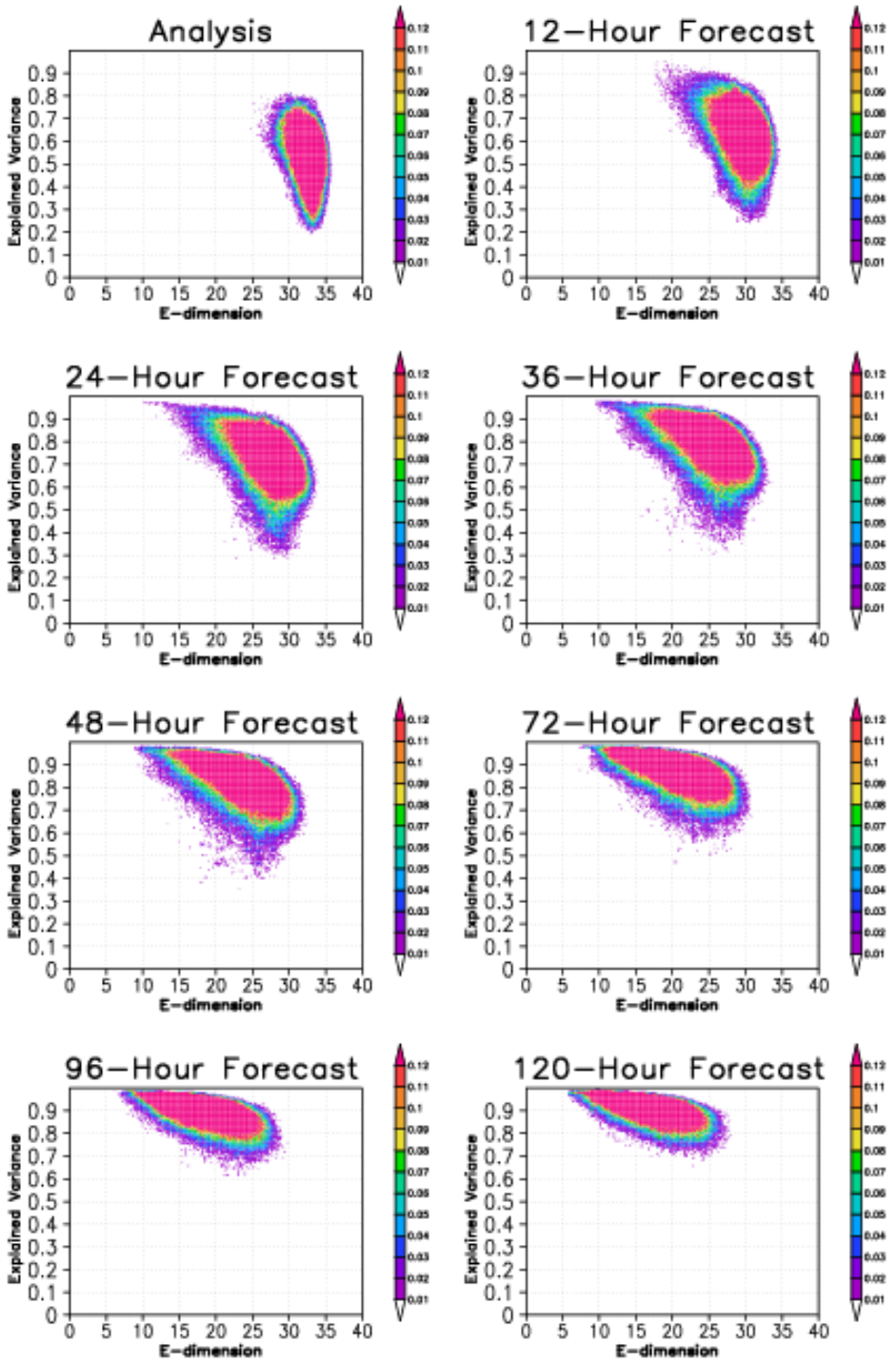

Figure B.9: Joint probability distribution of the E-dimension and the explained variance in the NH extratropics. The bins are defined by $\Delta E = 0.2$ and $\Delta EV = 0.005$.

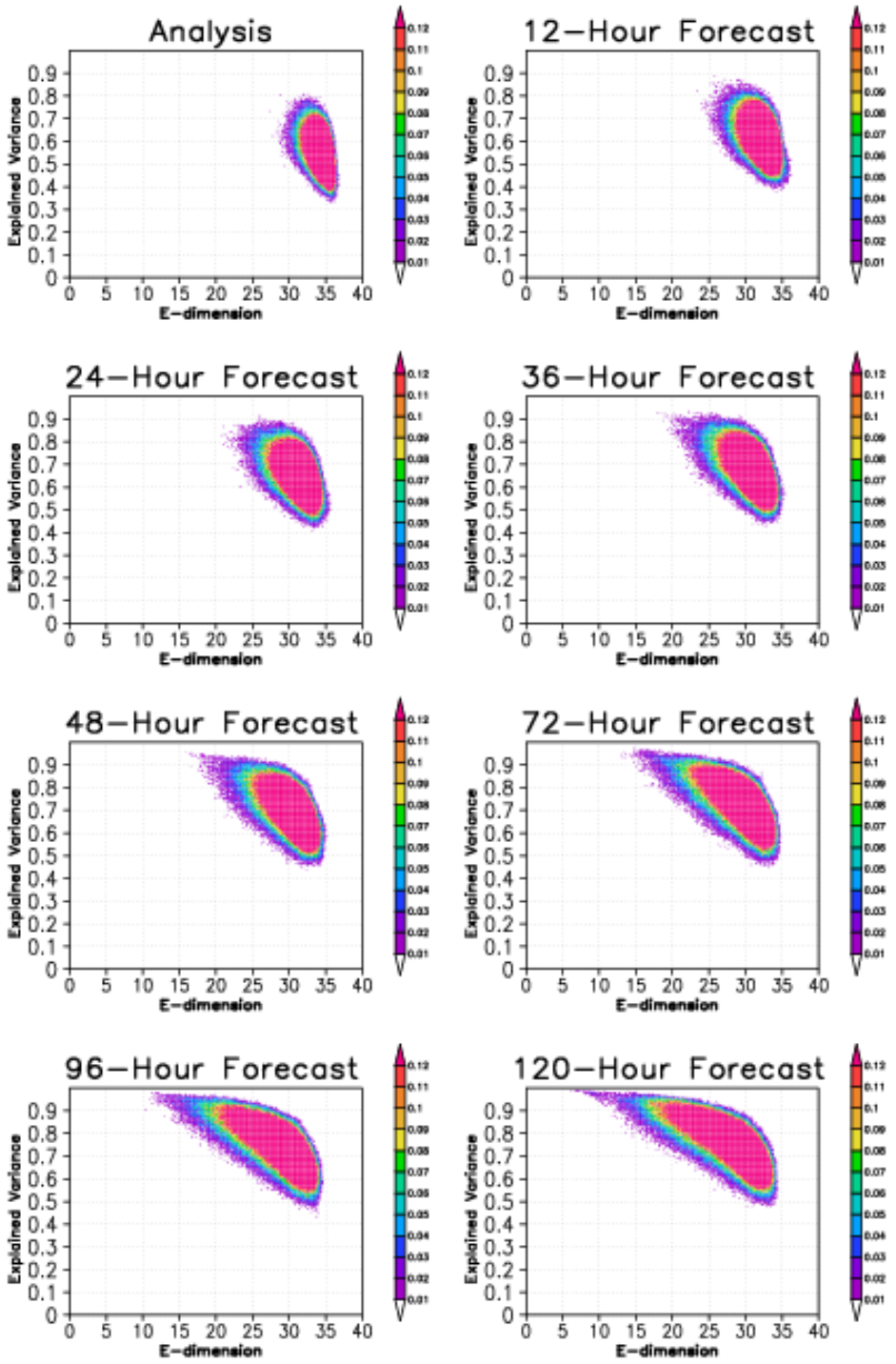

Figure B.10: Joint probability distribution of the E-dimension and the explained variance in the tropics. The bins are defined by $\Delta E = 0.2$ and $\Delta EV = 0.005$.

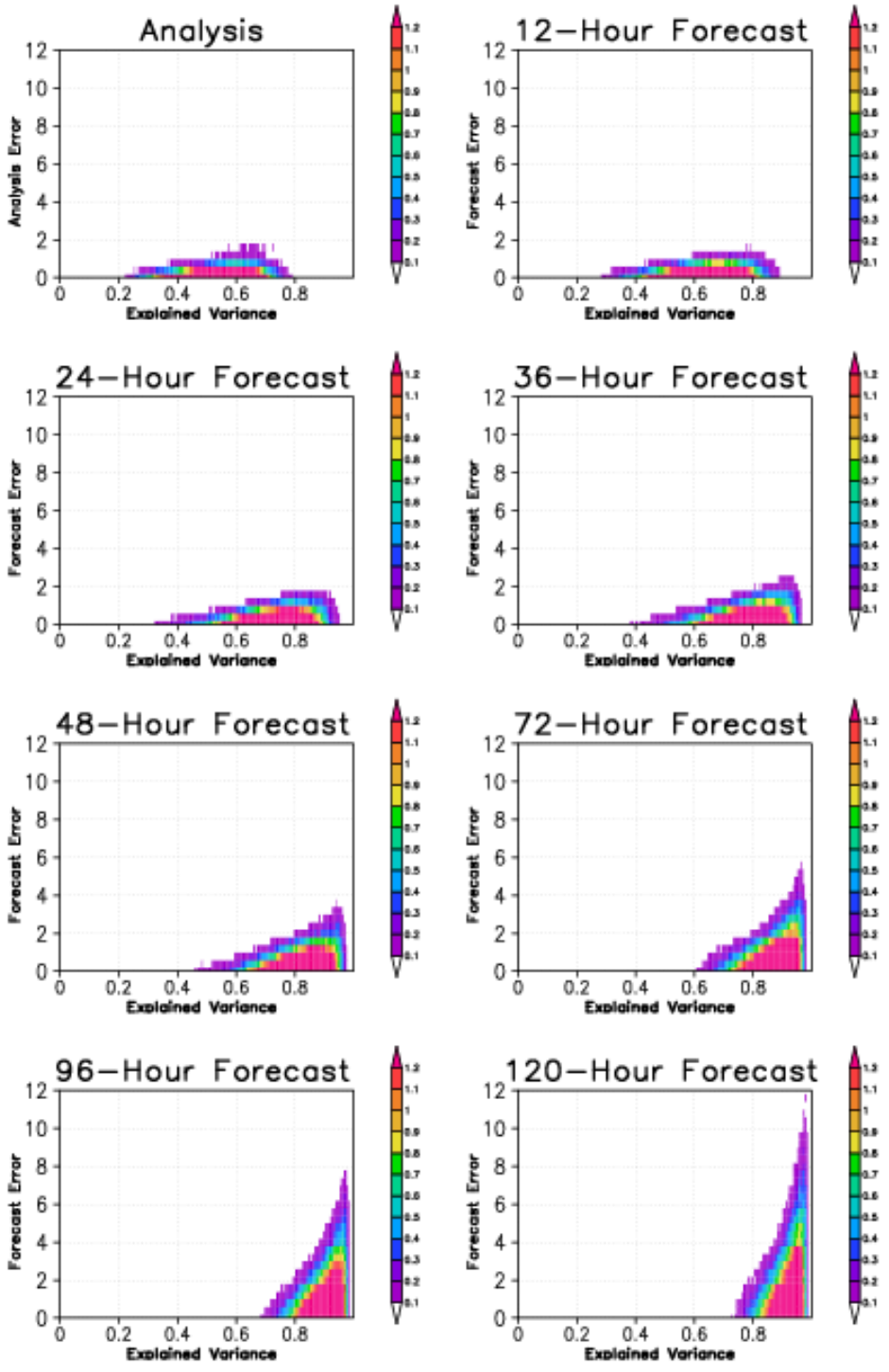

Figure B.11: Joint probability distribution of the explained variance and the magnitude of the error in the forecast of the meridional component of the wind at the 500 hPa level in the extratropics. The bins are defined by $\Delta E = 0.005$ and $\Delta ER = 0.4$, where ΔER is the interval for the forecast error.

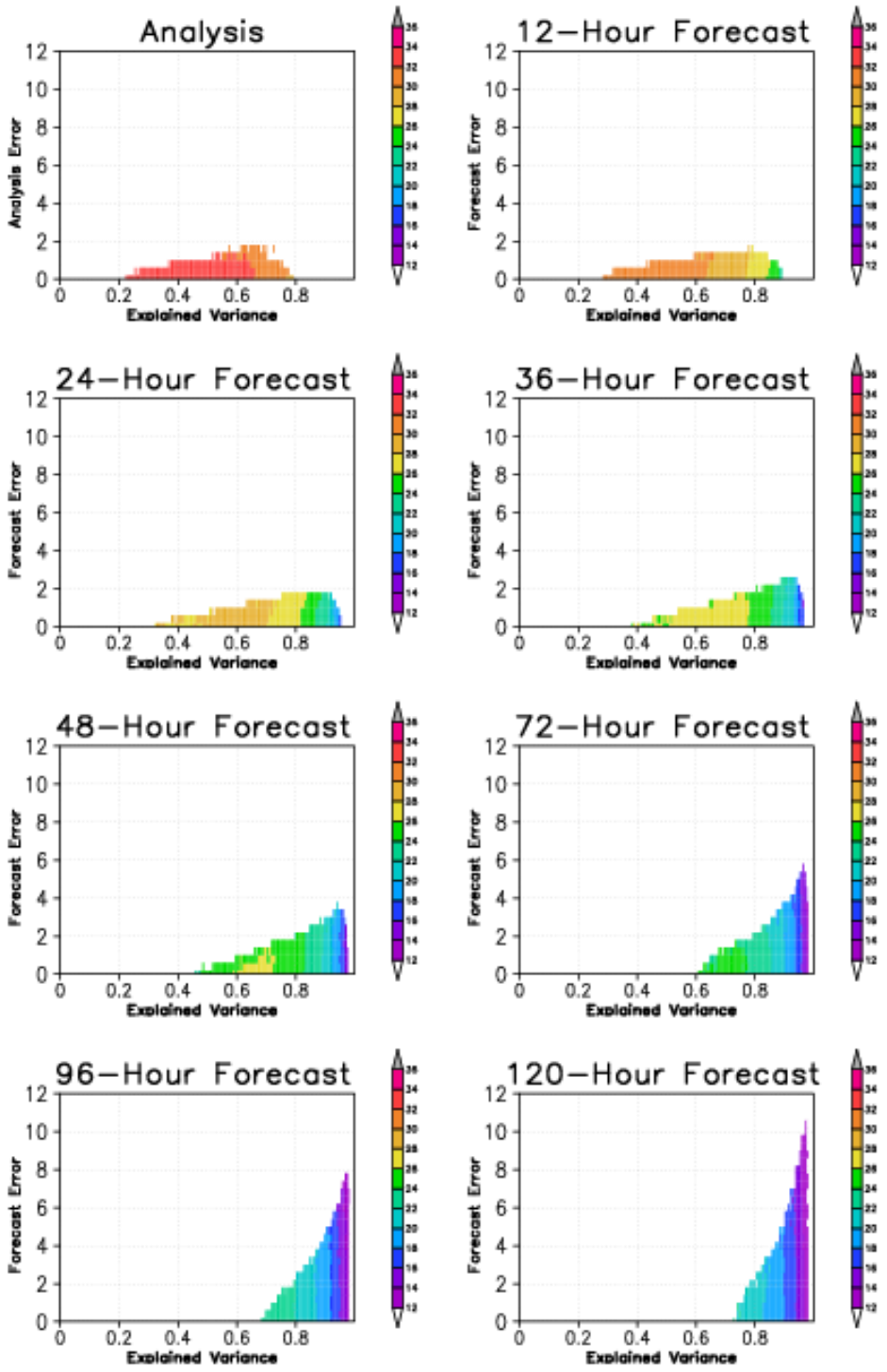

Figure B.12: Mean E-dimension for the bins shown in Figure B.11.

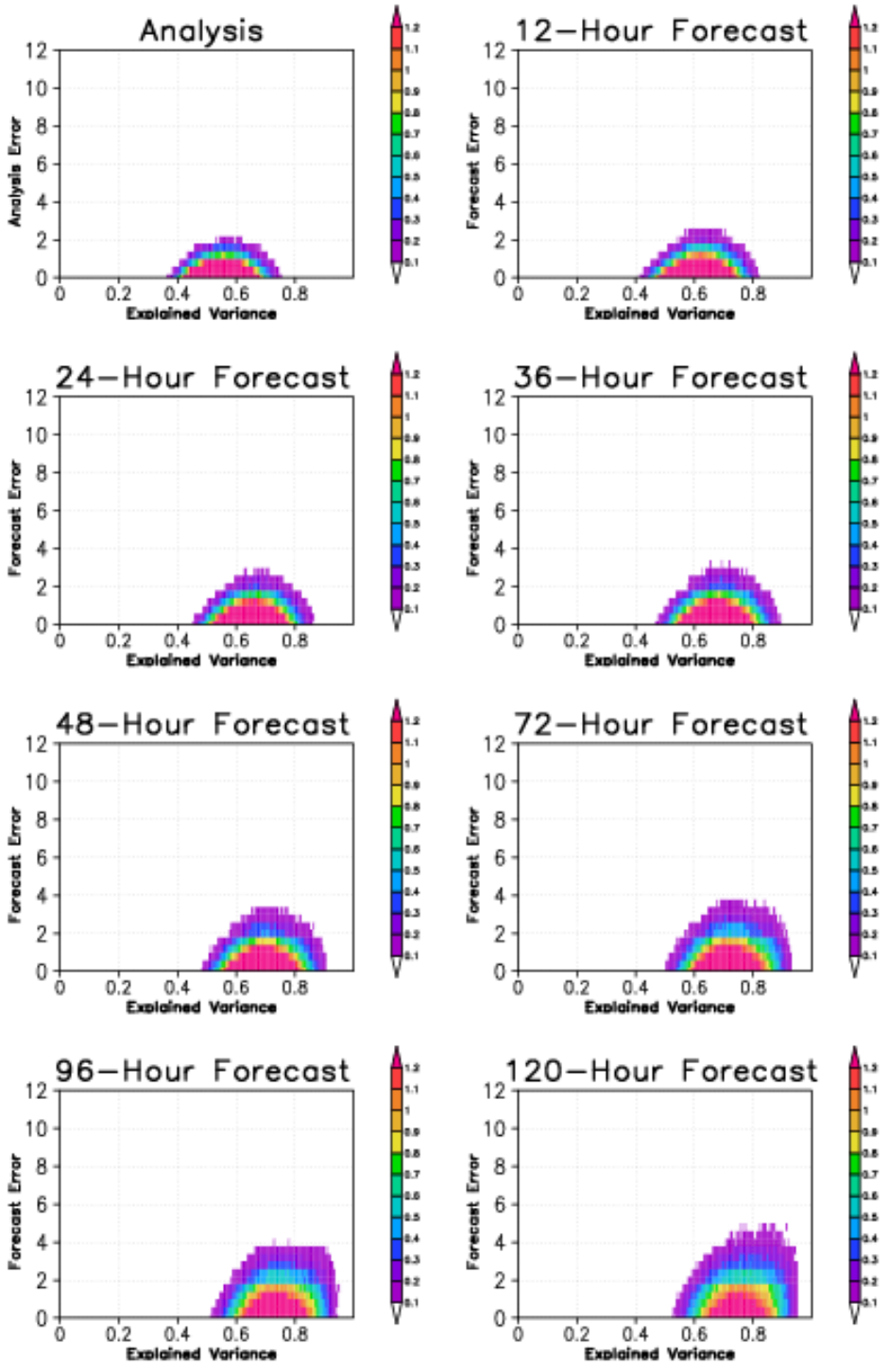

Figure B.13: Joint probability distribution of the explained variance and the magnitude of the error in the forecast of the meridional componet of the wind at the 500 hPa level in the tropics. The bins are defined by $\Delta E = 0.005$ and $\Delta ER = 0.4$.

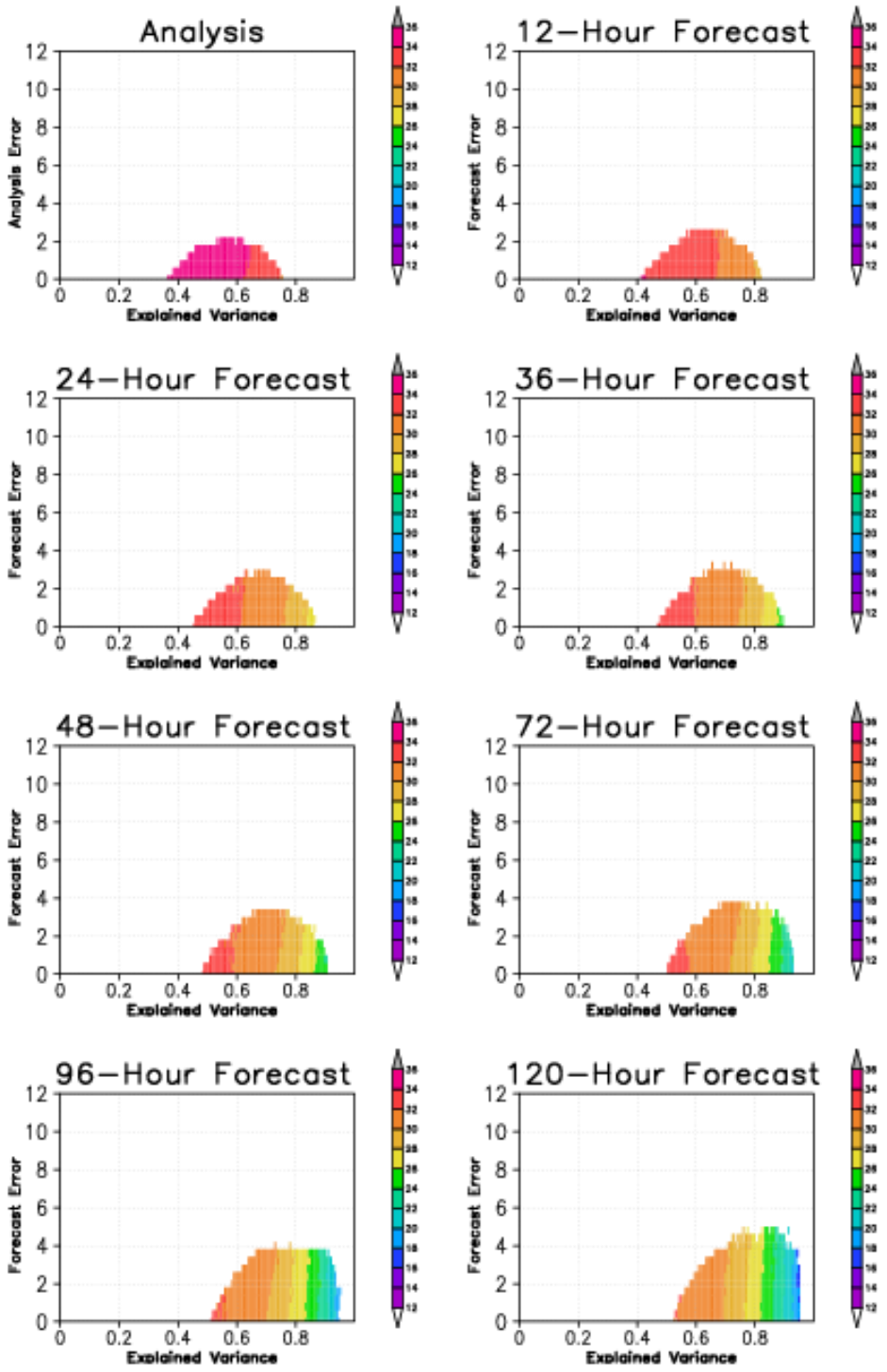

Figure B.14: Mean E-dimension for the bins shown in Figure B.13

.

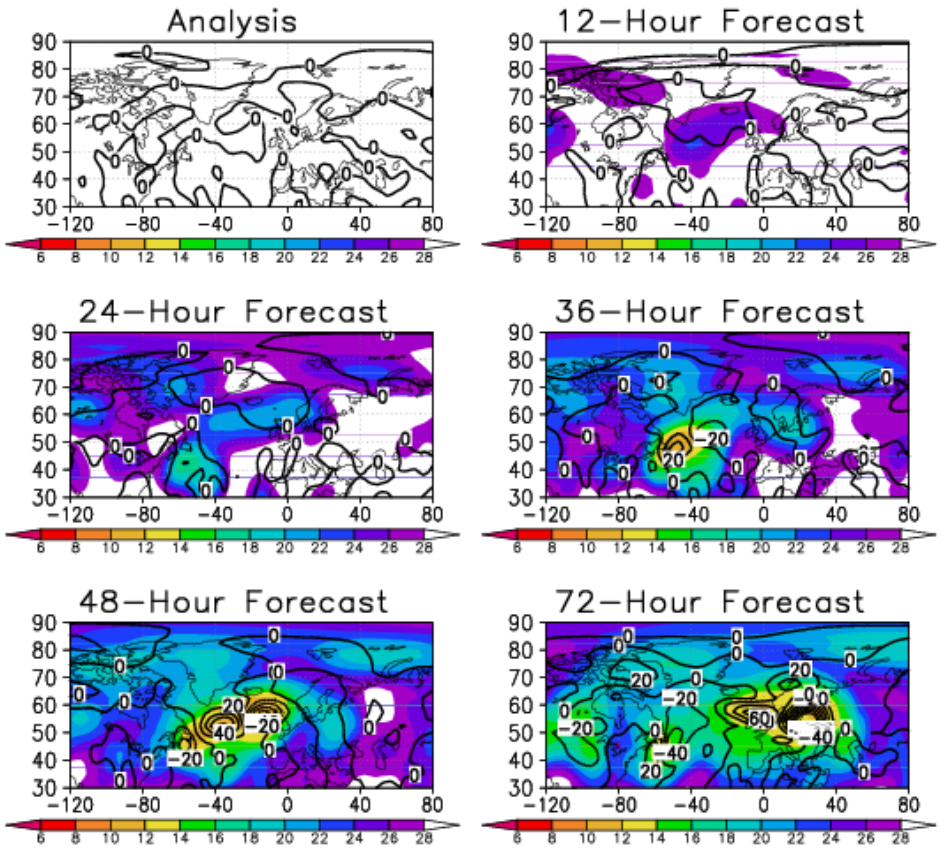

Figure B.15: Shown are the E-dimension (color shades) and the geopotential height forecast error at the 500 hPa level in the forecasts started at 1200 UTC on day 6.

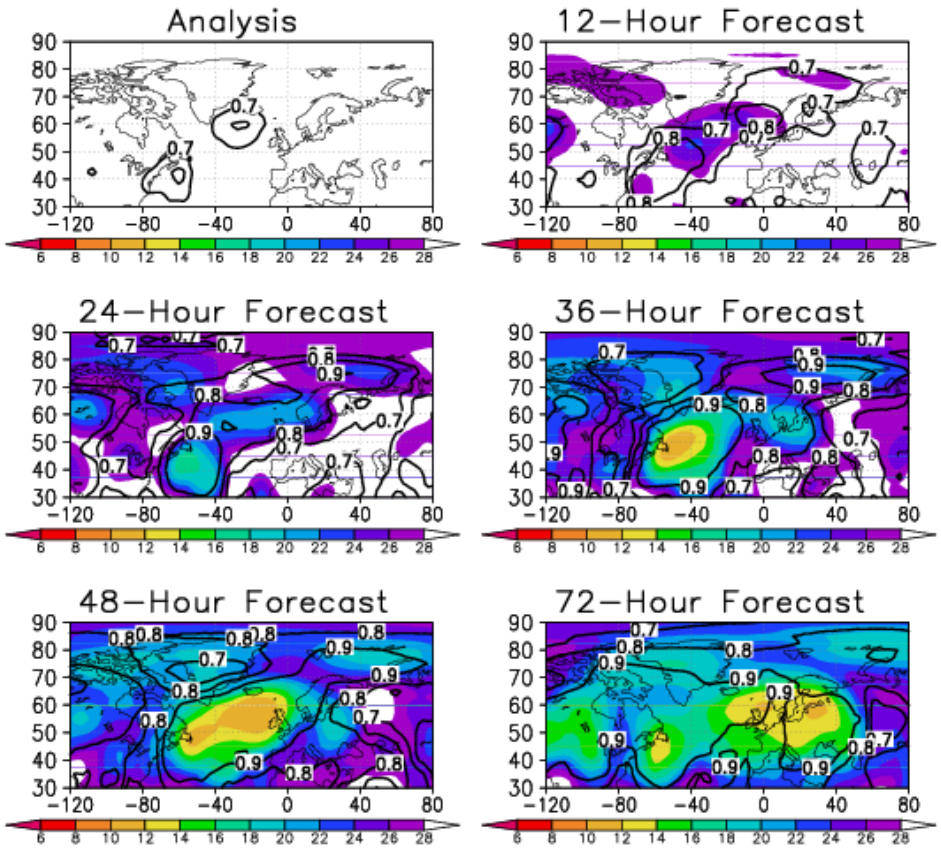

Figure B.16: Shown are the E-dimension (color shades) and the explained variance (contours) in the forecasts started at 1200 UTC day-6. The contour interval is 0.1 and values smaller than 0.7 are not shown.

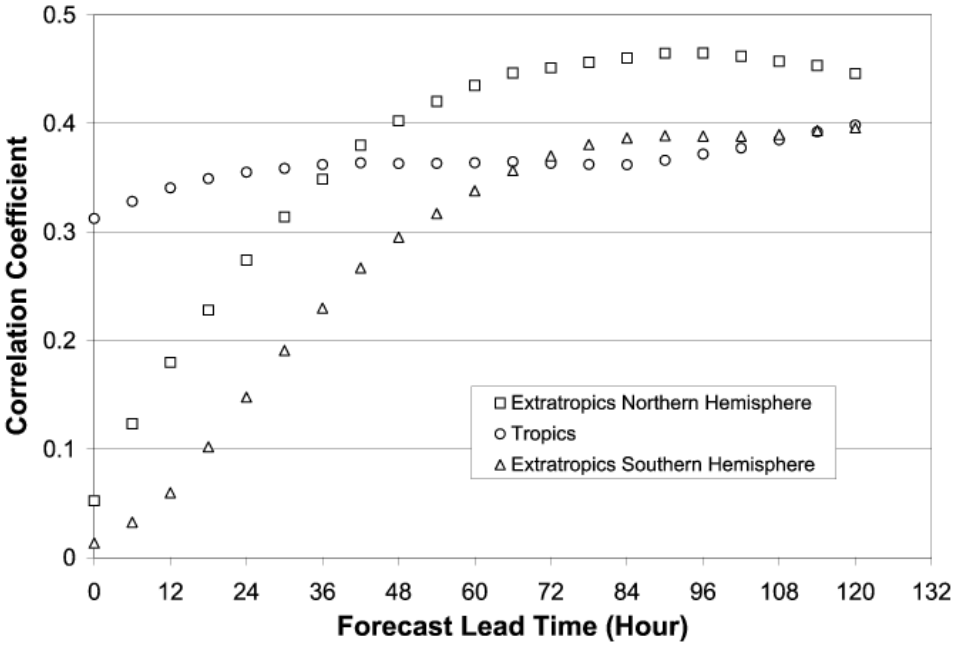

Figure B.17: Correlation between ensemble spread and error in the ensemble mean forecast as a function of forecast time.

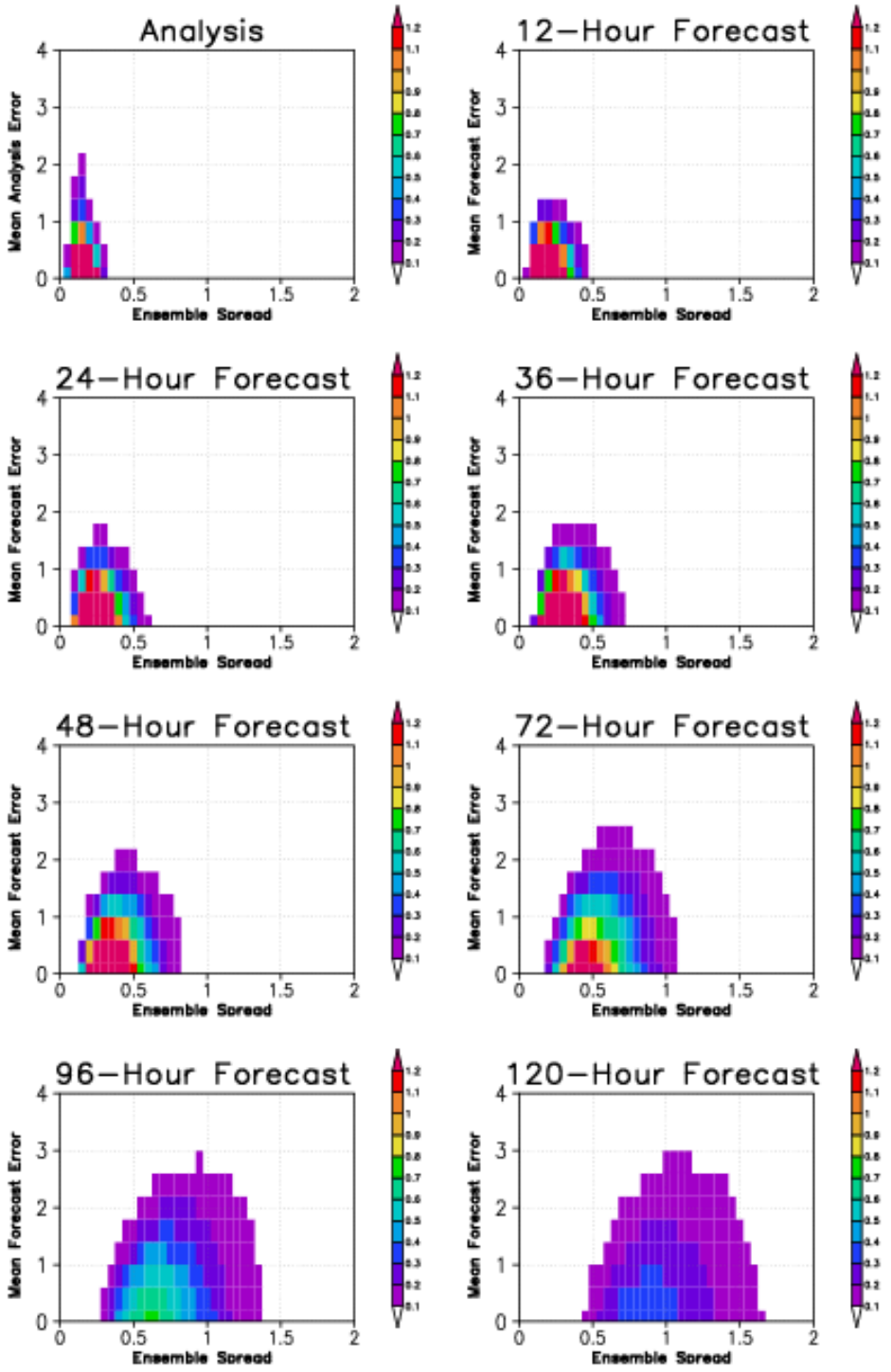

Figure B.18: Joint probability distribution of the ensemble spread and the magnitude of the error in the ensemble mean forecast of the meridional componet of the wind at the 500 hPa level in the NH extratropics. The width of the bins is 0.005 for the ensemble spread and 0.4 for the forecast error.

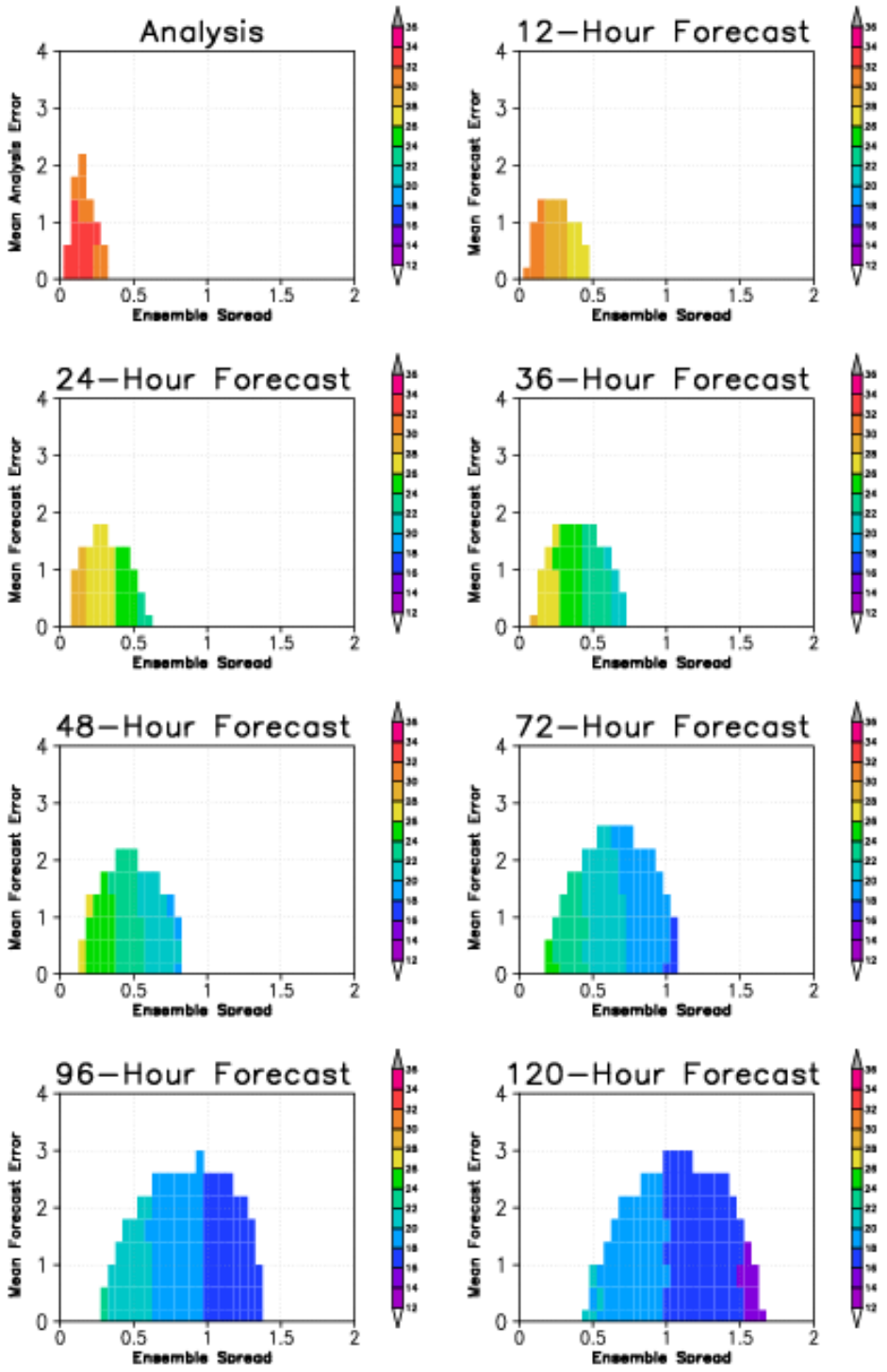

Figure B.19: Mean E-dimension for the bins shown in Figure 18

.

Table B.1: NH-extratropics root-mean-square analysis error, z_a, and error doubling time for the meridional wind component at the 500 hPa level at different observational densities. While these values are slightly different for the other model variables, they show the same tendencies.

number of soundings	rms analysis error	error doubling time
all locations	0.29 ms^{-1}	33.3 hours
2000 locations	0.39 ms^{-1}	34.7 hours
1000 locations	0.48 ms^{-1}	36.7 hours
500 locations	0.64 ms^{-1}	38.9 hours

Bibliography

Al-Saadi, J. A., R. B. Pierce, M. Natarajan, T. D. Fairlie, and W. L. Grose, 2004: Chemical climatology of the middle atmosphere simulated by the nasa langley research center interactive modeling project for atmospheric chemistry and transport (impact) model. *Journal of Geophysical Research-Atmospheres*, **109 (D17)**.

Anderson, J. L., 2001: An ensemble adjustment kalman filter for data assimilation. *Monthly Weather Review*, **129 (12)**, 2884–2903.

Anderson, J. L. and S. L. Anderson, 1999: A monte carlo implementation of the nonlinear filtering problem to produce ensemble assimilations and forecasts. *Monthly Weather Review*, **127 (12)**, 2741–2758.

Arakawa, A. and W. H. Schubert, 1974: Interaction of a cumulus cloud ensemble with large-scale environment .1. *Journal of the Atmospheric Sciences*, **31 (3)**, 674–701.

Aravequia, J. A., I. Szunyogh, E. J. Fertig, E. Kalnay, D. Kuhl, and E. J. Kostelich, Submitted: Evaluation of a strategy for the assimilation of satellite radiance observations with the local ensemble transform kalman filter. *Monthly Weather Review*.

Arellano, A. F., et al., 2007: Evaluating model performance of an ensemble-based chemical data assimilation system during intex-b field mission. *Atmospheric Chemistry and Physics*, **7 (21)**, 5695–5710.

Avery, M., cited 2009: In situ ozone and carbon dioxide measurements from the nasa dc-8 and p3-b aircraft. [Available online at http://www-gte.larc.nasa.gov/trace/TP_Avery_Vay_Instrument.htm].

Avery, M. A., D. J. Westberg, H. E. Fuelberg, R. E. Newell, B. E. Anderson, S. A. Vay, G. W. Sachse, and D. R. Blake, 2001: Chemical transport across the itcz in the central pacific during an el nino-southern oscillation cold phase event in march-april 1999. *Journal of Geophysical Research-Atmospheres*, **106 (D23)**, 32 539–32 553.

Backus, G. and F. Gilbert, 1970: Uniqueness in inversion of inaccurate gross earth data. *Philosophical Transactions of the Royal Society of London Series a-Mathematical and Physical Sciences*, **266 (1173)**, 123–192.

Baek, S. J., B. R. Hunt, E. Kalnay, E. Ott, and I. Szunyogh, 2006: Local ensemble kalman filtering in the presence of model bias. *Tellus Series a-Dynamic Meteorology and Oceanography*, **58 (3)**, 293–306.

Bengtsson, L., K. I. Hodges, and E. Roeckner, 2006: Storm tracks and climate change. *Journal of Climate*, **19 (15)**, 3518–3543.

Bhartia, P. K., R. D. McPeters, C. L. Mateer, L. E. Flynn, and C. Wellemeyer, 1996: Algorithm for the estimation of vertical ozone profiles from the backscattered ultraviolet technique. *Journal of Geophysical Research-Atmospheres*, **101 (D13)**, 18 793–18 806.

Bhartia, P. K., C. Wellemeyer, S. L. Taylor, N. Nath, and A. Gopalan, 2004: Solar backscatter ultraviolet (sbuv) version 8 profile algorithm. *Proceedings of the XX Quadrennial Ozone Symposium*, Z. C. S., Ed., International Ozone Commission, Athens, Greece, 295–296.

Bishop, C. H., B. J. Etherton, and S. J. Majumdar, 2001: Adaptive sampling with the ensemble transform kalman filter. part i: Theoretical aspects. *Monthly Weather Review*, **129 (3)**, 420–436.

CDIAC, cited 2009: Cdiac u.s. historical climatology network (hcn) daily temperature, precipitation, and snow observations for 1871-1997. [Available online at http://dss.ucar.edu/datasets/ds511.0/].

Charney, J. G., 1949: On a physical basis for numerical prediction of large-scale motions in the atmosphere. *Journal of Meteorology*, **6 (6)**, 371–385.

Coldewey-Egbers, M., M. Weber, L. N. Lamsal, R. de Beck, M. Buchwitz, and J. P. Burrows, 2005: Total ozone retrieval from gome uv spectral data using the weighting function doas approach. *Atmospheric Chemistry and Physics*, **5**, 1015–1025.

Constantinescu, E. M., A. Sandu, T. F. Chai, and G. R. Carmichael, 2007: Assessment of ensemble-based chemical data assimilation in an idealized setting. *Atmospheric Environment*, **41 (1)**, 18–36.

Deeter, M. N., et al., 2003: Operational carbon monoxide retrieval algorithm and selected results for the mopitt instrument. *Journal of Geophysical Research-Atmospheres*, **108 (D14)**.

Derber, J., et al., 1998: Changes to the 1998 ncep operational mrf model analysis/forecast system. *NOAA Technical Procedures Bulletin No. 449*.

Diab, R. D., A. Raghunandan, A. M. Thompson, and V. Thouret, 2003: Classification of tropospheric ozone profiles over johannesburg based on mozaic aircraft data. *Atmospheric Chemistry and Physics*, **3**, 713–723.

Dobson, G., 1930: Measurements of the amount of ozone in the earth's atmosphere and its relation to other geophysical conditions: Part iv. *Proceedings of the Royal Society of London*, **A129**, 411–433.

Dobson, G. and D. Harrison, 1926: Measurements of the amount of ozone in the earth's atmosphere and its relation to other geophysical conditions. *Proceedings of the Royal Society of London*, **A110**, 660–693.

Dobson, G., D. Harrison, and J. Lawrence, 1927: Measurements of the amount of ozone in the earth's atmosphere and its relation to other geophysical conditions: Part ii. *Proceedings of the Royal Society of London*, **A114**, 521–541.

Dobson, G., D. Harrison, and J. Lawrence, 1928: Measurements of the amount of ozone in the earth's atmosphere and its relation to other geophysical conditions: Part iii. *Proceedings of the Royal Society of London*, **A122**, 456–486.

Drummond, J. R. and G. S. Mand, 1996: The measurements of pollution in the troposphere (mopitt) instrument: Overall performance and calibration requirements. *Journal of Atmospheric and Oceanic Technology*, **13 (2)**, 314–320.

EDGAR, cited 2009: Emission database for global atmospheric research. [Available online at http://edgar.jrc.ec.europa.eu/].

Emanuel, K. A., 1994: *Atmospheric Convection*. Oxford University Press, New York.

Emmons, L. K., et al., 2004: Validation of measurements of pollution in the troposphere (mopitt) co retrievals with aircraft in situ profiles. *Journal of Geophysical Research-Atmospheres*, **109 (D3)**.

Emmons, L. K., et al., 2007: Measurements of pollution in the troposphere (mopitt) validation exercises during summer 2004 field campaigns over north america. *Journal of Geophysical Research-Atmospheres*, **112 (D12)**, 7.

Evensen, G., 2003: The ensemble kalman filter: theoretical formulation and practial implemntation. *Ocean dynamics*, **53**, 343–367.

Evensen, G., 2007: *Data Assimilation, the ensemble kalman filter*. Springer, New York.

Fertig, E. J., B. R. Hunt, E. Ott, and I. Szunyogh, 2007: Assimilating non-local observations with a local ensemble kalman filter. *Tellus Series a-Dynamic Meteorology and Oceanography*, **59 (5)**, 719–730.

Fleming, E. L., C. H. Jackman, J. E. Rosenfield, and D. B. Considine, 2002: Two-dimensional model simulations of the qbo in ozone and tracers in the tropical stratosphere. *Journal of Geophysical Research-Atmospheres*, **107 (D23)**, 17.

Forster, P., et al., 2007: Changes in atmospheric constituents and in radiative forcing. *Climate Change 2007: The Physical Science Basis*, S. Solomon, D. Qin, M. Manning, Z. Chen, M. Marquis, K. Averyt, T. M.M.B., and H. J. Miller, Eds., Cambridge Univ. Press, 129–234.

Fu, Q., C. M. Johanson, J. M. Wallace, and T. Reichler, 2006: Enhanced mid-latitude tropospheric warming in satellite measurements. *Science*, **312 (5777)**, 1179–1179.

Fyfe, J. C., 2003: Extratropical southern hemisphere cyclones: Harbingers of climate change? *Journal of Climate*, **16 (17)**, 2802–2805.

GEIA, cited 2009: Global emissions inventory activity homepage. [Available online at http://www.geiacenter.org/].

Geng, Q. Z. and M. Sugi, 2003: Possible change of extratropical cyclone activity due to enhanced greenhouse gases and sulfate aerosols - study with a high-resolution agcm. *Journal of Climate*, **16 (13)**, 2262–2274.

Gill, A., 1982: *Atmosphere and Ocean Dynamics*. Academic Press.

Grell, G. A., 1993: Prognostic evaluation of assumptions used by cumulus parameterizations. *Monthly Weather Review*, **121 (3)**, 764–787.

Grundstein, A., 2003: A synoptic-scale climate analysis of anomalous snow water equivalent over the northern great plains of the usa. *International Journal of Climatology*, **23 (8)**, 871–886.

Hakim, G. J., 2005: Vertical structure of midlatitude analysis and forecast errors. *Monthly Weather Review*, **133 (3)**, 567–578.

Hall, N. M. J., B. J. Hoskins, P. J. Valdes, and C. A. Senior, 1994: Storm tracks in a high-resolution gcm with doubled carbon-dioxide. *Quarterly Journal of the Royal Meteorological Society*, **120 (519)**, 1209–1230.

Hanna, S. R., J. C. Chang, and M. E. Fernau, 1998: Monte carlo estimates of uncertainties in predictions by a photochemical grid model (uam-iv) due to uncertainties in input variables. *Atmospheric Environment*, **32 (21)**, 3619–3628.

Heath, D. F., A. J. Krueger, H. A. Roeder, and B. D. Henderson, 1975: Solar backscatter ultraviolet and total ozone mapping spectrometer (sbuv-toms) for nimbus g. *Optical Engineering*, **14 (4)**, 323–331.

Hilsenrath, E., R. P. Cebula, M. T. Deland, K. Laamann, S. Taylor, C. Wellemeyer, and P. K. Bhartia, 1995: Calibration of the noaa-11 solar backscatter ultraviolet (sbuv/2) ozone data set from 1989 to 1993 using in-flight calibration data and ssbuv. *Journal of Geophysical Research-Atmospheres*, **100 (D1)**, 1351–1366.

Hipskind, R. S., G. L. Gregory, G. W. Sachse, G. F. Hill, and E. F. Danielsen, 1987: Correlations between ozone and carbon-monoxide in the lower stratosphere, folded tropopause, and maritime troposphere. *Journal of Geophysical Research-Atmospheres*, **92 (D2)**, 2121–2130.

Holton, J. R., P. H. Haynes, M. E. McIntyre, A. R. Douglass, R. B. Rood, and L. Pfister, 1995: Stratosphere-troposphere exchange. *Reviews of Geophysics*, **33 (4)**, 403–439.

Houtekamer, P. L., 1993: Global and local skill forecasts. *Monthly Weather Review*, **121 (6)**, 1834–1846.

Houtekamer, P. L. and H. L. Mitchell, 2001: A sequential ensemble kalman filter for atmospheric data assimilation. *Monthly Weather Review*, **129 (1)**, 123–137.

Hu, Q., A. Weiss, S. Feng, and P. S. Baenziger, 2005: Earlier winter wheat heading dates and warmer spring in the us great plains. *Agricultural and Forest Meteorology*, **135 (1-4)**, 284–290.

Hu, Y. and Q. Fu, 2007: Observed poleward expansion of the hadley circulation since 1979. *Atmospheric Chemistry and Physics*, **7 (19)**, 5229–5236.

Hudson, R. D., M. F. Andrade, M. B. Follette, and A. D. Frolov, 2006: The total ozone field separated into meteorological regimes - part ii: Northern hemisphere mid-latitude total ozone trends. *Atmospheric Chemistry and Physics*, **6**, 5183–5191.

Hudson, R. D., A. D. Frolov, M. F. Andrade, and M. B. Follette, 2003: The total ozone field separated into meteorological regimes. part i: defining the regimes. *Journal of the Atmospheric Sciences*, **60 (14)**, 1669–1677.

Hunt, B. R., E. J. Kostelich, and I. Szunyogh, 2007: Efficient data assimilation for spatiotemporal chaos: A local ensemble transform kalman filter. *PHYSICA D-NONLINEAR PHENOMENA*, **230 (1-2)**, 112–126.

Jiang, J. and W. Perrie, 2007: The impacts of climate change on autumn north atlantic midlatitude cyclones. *Journal of Climate*, **20 (7)**, 1174–1187.

Kalnay, E., 2003: *Atmospheric modeling, data assimilation and predictability*. Cambridge University Press, New York.

Karl, T. R., R. W. Knight, D. R. Easterling, and R. G. Quayle, 1996: Indices of climate change for the united states. *Bulletin of the American Meteorological Society*, **77 (2)**, 279–292.

Karoly, D. J. and Q. G. Wu, 2005: Detection of regional surface temperature trends. *Journal of Climate*, **18 (21)**, 4337–4343.

Keppenne, C. L. and M. M. Rienecker, 2002: Initial testing of a massively parallel ensemble kalman filter with the poseidon isopycnal ocean general circulation model. *Monthly Weather Review*, **130 (12)**, 2951–2965.

Keyser, D. and M. A. Shapiro, 1986: A review of the structure and dynamics of upper-level frontal zones. *Monthly Weather Review*, **114 (2)**, 452–499.

Kiss, P., R. Muller, and I. M. Janosi, 2007: Long-range correlations of extrapolar total ozone are determined by the global atmospheric circulation. *Nonlinear Processes in Geophysics*, **14 (4)**, 435–442.

Knippertz, P., U. Ulbrich, and P. Speth, 2000: Changing cyclones and surface wind speeds over the north atlantic and europe in a transient ghg experiment. *Climate Research*, **15 (2)**, 109–122.

Koch, S. E., et al., 2005: Turbulence and gravity waves within an upper-level front. *Journal of the Atmospheric Sciences*, **62 (11)**, 3885–3908.

Komhyr, W. D., 1969: Electrochemical concentration cells for gas analysis. *Annales De Geophysique*, **25 (1)**, 203.

Kuhl, D., et al., 2007: Assessing predictability with a local ensemble kalman filter. *Journal of the Atmospheric Sciences*, **64 (4)**, 1116–1140.

Ladstatter-Weissenmayer, A., M. Kanakidou, J. Meyer-Arnek, E. V. Dermitzaki, A. Richter, M. Vrekoussis, F. Wittrock, and J. P. Burrows, 2007: Pollution events over the east mediterranean: Synergistic use of gome, ground-based and sonde observations and models. *Atmospheric Environment*, **41 (34)**, 7262–7273.

Leroy, S. S., J. G. Anderson, and J. A. Dykema, 2006: Testing climate models using gps radio occultation: A sensitivity analysis. *Journal of Geophysical Research-Atmospheres*, **111 (D17)**, 15.

Livezey, R. E. and W. Y. Chen, 1983: Statistical field significance and its determination by monte-carlo techniques. *Monthly Weather Review*, **111 (1)**, 46–59.

Lorenc, A. C., 1981: A global 3-dimensional multivariate statistical interpolation scheme. *Monthly Weather Review*, **109 (4)**, 701–721.

Lu, J., G. A. Vecchi, and T. Reichler, 2007: Expansion of the hadley cell under global warming. *Geophysical Research Letters*, **34 (6)**, 5.

McCabe, G. J., M. P. Clark, and M. C. Serreze, 2001: Trends in northern hemisphere surface cyclone frequency and intensity. *Journal of Climate*, **14 (12)**, 2763–2768.

McPeters, R. D. and G. J. Labow, 1996: An assessment of the accuracy of 14.5 years of nimbus 7 toms version 7 ozone data by comparison with the dobson network. *Geophysical Research Letters*, **23 (25)**, 3695–3698.

McPeters, R. D., G. J. Labow, and J. A. Logan, 2007: Ozone climatological profiles for satellite retrieval algorithms. *Journal of Geophysical Research-Atmospheres*, **112 (D5)**, 9.

McPeters, R. D., C. G. Wellemeyer, and C. Ahn, 2004: The validation of version 8 ozone profiles: Is sbuv ready for prime time? *International Quadrennial Ozone Symposium, 1-8 Jun. 2004,*, Kos, Greece.

Miyazaki, K., 2009: Performance of a local ensemble transform kalman filter for the analysis of atmospheric circulation and distribution of long-lived tracers under idealized conditions. *Journal of Geophysical Research-Atmospheres*, **114**, 21.

Nazaryan, H., M. P. McCormick, and J. M. Russell, 2007: Comparative analysis of sbuv/2 and haloe ozone profiles and trends. *Journal of Geophysical Research-Atmospheres*, **112 (D10)**, 17.

Neumann, C. J., M. B. Lawrence, and E. L. Caso, 1977: Monte-carlo significance testing as applied to statistical tropical cyclone prediction models. *Journal of Applied Meteorology*, **16 (11)**, 1165–1174.

Oczkowski, M., I. Szunyogh, and D. J. Patil, 2005: Mechanisms for the development of locally low-dimensional atmospheric dynamics. *Journal of the Atmospheric Sciences*, **62 (4)**, 1135–1156.

Orlanski, I. and E. K. M. Chang, 1993: Ageostrophic geopotential fluxes in downstream and upstream development of baroclinic waves. *Journal of the Atmospheric Sciences*, **50 (2)**, 212–225.

Orlanski, I. and J. P. Sheldon, 1995: Stages in the energetics of baroclinic systems. *Tellus Series A-Dynamic Meteorology and Oceanography*, **47 (5)**, 605–628.

Ott, E., 2003: *Chaos in dynamical systems.* Cambridge, New York.

Ott, E., et al., 2004: A local ensemble kalman filter for atmospheric data assimilation. *Tellus Series a-Dynamic Meteorology and Oceanography*, **56 (5)**, 415–428.

Pan, L. L., W. J. Randel, B. L. Gary, M. J. Mahoney, and E. J. Hintsa, 2004: Definitions and sharpness of the extratropical tropopause: A trace gas perspective. *Journal of Geophysical Research-Atmospheres*, **109 (D23)**, 11.

Patil, D. J., B. R. Hunt, E. Kalnay, J. A. Yorke, and E. Ott, 2001: Local low dimensionality of atmospheric dynamics. *Physical Review Letters*, **86 (26)**, 5878–5881.

Persson, A., 2000: Synoptic-dynamic diagnosis of medium range weather forecast systems. *Proceedings of the Seminars on diagnosis of models and data assimilation systems*, ECMWF, Reading, U.K., 123–137.

Petropavlovskikh, I., C. Ahn, P. K. Bhartia, and L. E. Flynn, 2005: Comparison and covalidation of ozone anomalies and variability observed in sbuv(/2) and umkehr northern midlatitude ozone profile estimates. *Geophysical Research Letters*, **32 (6)**.

Phillips, N. A., 1990: Dispersion processes in large-scale weather prediction. Tech. rep., World Meteorological Oranization.

Pierce, R. B., et al., 2007: Chemical data assimilation estimates of continental us ozone and nitrogen budgets during the intercontinental chemical transport experiment-north america. *Journal of Geophysical Research-Atmospheres*, **112 (D12)**, 30.

Pinto, J. G., U. Ulbrich, G. C. Leckebusch, T. Spangehl, M. Reyers, and S. Zacharias, 2007: Changes in storm track and cyclone activity in three sres ensemble experiments with the echam5/mpi-om1 gcm. *Climate Dynamics*, **29 (2-3)**, 195–210.

Polsky, C. and W. E. Easterling, 2001: Adaptation to climate variability and change in the us great plains: A multi-scale analysis of ricardian climate sensitivities. *Agriculture Ecosystems and Environment*, **85 (1-3)**, 133–144.

Randel, W. J., D. J. Seidel, and L. L. Pan, 2007: Observational characteristics of double tropopauses. *Journal of Geophysical Research-Atmospheres*, **112 (D7)**, 13.

Rao, T. N. and S. Kirkwood, 2005: Characteristics of tropopause folds over arctic latitudes. *Journal of Geophysical Research-Atmospheres*, **110 (D18)**, 16.

Rault, D. F. and G. Taha, 2007: Validation of ozone profiles retrieved from stratospheric aerosol and gas experiment iii limb scatter measurements. *Journal of Geophysical Research-Atmospheres*, **112 (D13)**, 17.

Rodgers, C. D., 1990: Characterization and error analysis of profiles retrieved from remote sounding measurements. *Journal of Geophysical Research-Atmospheres*, **95 (D5)**, 5587–5595.

Rodgers, C. D., 2000: *Inverse methods for atmospheric sounding : theory and practice*. Series on atmospheric, oceanic and planetary physics ; v.2, World Scientific, Singapore ; [River Edge, N.J.].

Rood, R. B., et al., 1991: 3-dimensional simulations of wintertime ozone variability in the lower stratosphere. *Journal of Geophysical Research-Atmospheres*, **96 (D3)**, 5055–5071.

Rossby, C.-G., 1949: On the dispersion of planetary waves in a barotropic atmosphere. *Tellus*, **1 (1)**, 54–58.

Sachse, G. W., G. F. Hill, L. O. Wade, and M. G. Perry, 1987: Fast-response, high-precision carbon-monoxide sensor using a tunable diode-laser absorption technique. *Journal of Geophysical Research-Atmospheres*, **92 (D2)**, 2071–2081.

Satterfield, E. A. and I. Szunyogh, 2009: Predictability of the performance of an ensemble forecast system: Predictability of the space of uncertanties. *Monthly Weather Review*.

Seidel, D. J. and W. J. Randel, 2007: Recent widening of the tropical belt: Evidence from tropopause observations. *Journal of Geophysical Research-Atmospheres*, **112 (D20)**, 6.

Serra, C., A. Burguen, M. D. Martinez, and X. Lana, 2006: Trends in dry spells across catalonia (ne spain) during the second half of the 20th century. *Theoretical and Applied Climatology*, **85 (3-4)**, 165–183.

Shapiro, M. A., 1978: Further evidence of mesoscale and turbulent structure of upper level jet stream-frontal zone systems. *Monthly Weather Review*, **106 (8)**, 1100–1111.

Shapiro, M. A., 1980: Turbulent mixing within tropopause folds as a mechanism for the exchange of chemical-constituents between the stratosphere and troposphere. *Journal of the Atmospheric Sciences*, **37 (5)**, 994–1004.

Shapiro, M. A., 1981: Frontogenesis and geostrophically forced secondary circulations in the vicinity of jet-stream frontal zone systems. *Journal of the Atmospheric Sciences*, **38 (5)**, 954–973.

Shapiro, M. A., A. J. Kreuger, and P. J. Kennedy, 1982: Nowcasting the position and intensity of jet streams using a satellite-borne total ozone mapping spectrometer. *Nowcasting*, K. A. Browning, Ed., Academic Press, 137–145.

Singh, H. B., W. H. Brune, J. H. Crawford, D. J. Jacob, and P. B. Russell, 2006: Overview of the summer 2004 intercontinental chemical transport experiment - north america (intex-a). *Journal of Geophysical Research-Atmospheres*, **111 (D24)**.

Snyder, C., 1999: Error growth in flows with finite-amplitude waves or coherent structures. *Journal of the Atmospheric Sciences*, **56 (4)**, 500–506.

Soja, A. J., W. R. Cofer, H. H. Shugart, A. I. Sukhinin, P. W. Stackhouse, D. J. McRae, and S. G. Conard, 2004: Estimating fire emissions and disparities in boreal siberia (1998-2002). *Journal of Geophysical Research-Atmospheres*, **109 (D14)**.

Solomon, S. D., et al., 2007: Technical summary. *Climate Change 2007: The Physical Science Basis*, S. D. Solomon, D. Qin, M. Manning, Z. Chen, M. Marquis, K. B. B. Averyt, M. M. B. Tignor, and H. L. Miller, Jr., Eds., Cambridge University Press, 19–91.

Stobie, J., 2000: Algorithm theoretical basis document for statistical digital filter (sdf) analysis system (stretch-grid version). Tech. rep., Data Assimilation Office, NASA Goddard Space Flight Center, Greenbelt, Md. This was never published!! I got it from a guy at UW. Goddard had no records of this publication.

Streets, D. G., et al., 2003: An inventory of gaseous and primary aerosol emissions in asia in the year 2000. *Journal of Geophysical Research-Atmospheres*, **108 (D21)**.

Szunyogh, I., E. Kalnay, and Z. Toth, 1997: A comparison of lyapunov and optimal vectors in a low-resolution gcm. *Tellus Series a-Dynamic Meteorology and Oceanography*, **49 (2)**, 200–227.

Szunyogh, I., E. J. Kostelich, G. Gyarmati, E. Kalnay, B. R. Hunt, E. Ott, E. Satterfield, and J. A. Yorke, 2008: A local ensemble transform kalman filter data

assimilation system for the ncep global model. *Tellus Series a-Dynamic Meteorology and Oceanography*, **60 (1)**, 113–130.

Szunyogh, I., E. J. Kostelich, G. Gyarmati, D. J. Patil, B. R. Hunt, E. Kalnay, E. Ott, and J. A. Yorke, 2005: Assessing a local ensemble kalman filter: perfect model experiments with the national centers for environmental prediction global model. *Tellus Series a-Dynamic Meteorology and Oceanography*, **57 (4)**, 528–545.

Szunyogh, I., Z. Toth, R. E. Morss, S. J. Majumdar, B. J. Etherton, and C. H. Bishop, 2000: The effect of targeted dropsonde observations during the 1999 winter storm reconnaissance program. *Monthly Weather Review*, **128 (10)**, 3520–3537.

Szunyogh, I., Z. Toth, A. V. Zimin, S. J. Majumdar, and A. Persson, 2002: Propagation of the effect of targeted observations: The 2000 winter storm reconnaissance program. *Monthly Weather Review*, **130 (5)**, 1144–1165.

Takamura, H., T. Sampe, Y. Tanimoto, and A. Shimpo, 2004: Observed associations among storm tracks, jet streams, and midlatitude oceanic fronts. *Earth's Climate: The Ocean-Atmosphere Interaction*, C. Wang, X. S.-P., and J. A. Carton, Eds., American Geophysical Union, 329–343.

Thepaut, J.-N., 2003: Satellite data assimilation in numerical weather prediction: an overview. *Seminar on Recent developments in data assimilation for atmosphere and ocean*, Shinfield Park, Reading, 75–96.

Thompson, A. M., et al., 2007a: Intercontinental chemical transport experiment ozonesonde network study (ions) 2004: 1. summertime upper troposphere/lower stratosphere ozone over northeastern north america. *Journal of Geophysical Research-Atmospheres*, **112 (D12)**, 15.

Thompson, A. M., et al., 2007b: Intercontinental chemical transport experiment ozonesonde network study (ions) 2004: 2. tropospheric ozone budgets and variability over northeastern north america. *Journal of Geophysical Research-Atmospheres*, **112 (D12)**, 22.

TOMS, cited 2009: Total ozone mapping spectrometer. [Available online at http://toms.gsfc.nasa.gov/].

Toth, Z. and E. Kalnay, 1993: Ensemble forecasting at nmc - the generation of perturbations. *Bulletin of the American Meteorological Society*, **74 (12)**, 2317–2330.

Toth, Z. and E. Kalnay, 1997: Ensemble forecasting at ncep and the breeding method. *Monthly Weather Review*, **125 (12)**, 3297–3319.

Trenberth, K. E., et al., 2007: Observations: Surface and atmospheric climate change. *Climate Change 2007: The Physical Science Basis*, S. D. Solomon, D. Qin,

M. Manning, Z. Chen, M. Marquis, K. B. B. Averyt, M. M. B. Tignor, and H. L. Miller, Jr., Eds., Cambridge University Press, 235–336.

von Storch, H. and F. Zwiers, 1999: *Statistical Analysis in Climate Research*. Cambridge Univ. Press.

Wang, X. L. L., V. R. Swail, and F. W. Zwiers, 2006: Climatology and changes of extratropical cyclone activity: Comparison of era-40 with ncep-ncar reanalysis for 1958-2001. *Journal of Climate*, **19 (13)**, 3145–3166.

Whitaker, J. S. and T. M. Hamill, 2002: Ensemble data assimilation without perturbed observations. *Monthly Weather Review*, **130 (7)**, 1913–1924.

Whitaker, J. S. and A. F. Loughe, 1998: The relationship between ensemble spread and ensemble mean skill. *Monthly Weather Review*, **126 (12)**, 3292–3302.

Wilks, D. S., 2006: *Statistical Methods in the Atmospheric Sciences*. 2d ed., Elsevier Academic Press.

Yin, J. H., 2005: A consistent poleward shift of the storm tracks in simulations of 21st century climate. *Geophysical Research Letters*, **32 (18)**, 4.

Zachariasse, M., P. F. J. van Velthoven, H. G. J. Smit, J. Lelieveld, T. K. Mandal, and H. Kelder, 2000: Influence of stratosphere-troposphere exchange on tropospheric ozone over the tropical indian ocean during the winter monsoon. *Journal of Geophysical Research-Atmospheres*, **105 (D12)**, 15 403–15 416.

Zimin, A. V., I. Szunyogh, B. R. Hunt, and E. Ott, 2006: Extracting envelopes of nonzonally propagating rossby wave packets. *Monthly Weather Review*, **134 (4)**, 1329–1333.

Zimin, A. V., I. Szunyogh, D. J. Patil, B. R. Hunt, and E. Ott, 2003: Extracting envelopes of rossby wave packets. *Monthly Weather Review*, **131 (5)**, 1011–1017.